The Thesis Committee for Danny W. Anderson
Certifies that this is the approved version of the following Thesis:

Xenolith constraints on the origin of low $\delta^{18}O$ values in Mauna Kea basalts: The role of self-assimilation

APPROVED BY
SUPERVISING COMMITTEE:

John C. Lassiter, Supervisor

Jaime D. Barnes, Committee Member

James E. Gardner, Committee Member

Xenolith constraints on the origin of low δ18O values in Mauna Kea basalts: The role of self-assimilation

by

Danny W. Anderson

Thesis

Presented to the Faculty of the Graduate School of

The University of Texas at Austin

in Partial Fulfillment

of the Requirements

for the Degree of

Bachelor of Science in Geological Sciences: General Geology

The University of Texas at Austin

May 2018

Acknowledgements

I would like to thank Dr. John Lassiter for being an outstanding advisor and constantly encouraging me to put my best efforts into this project. Additionally, thank you to my graduate student mentor Ed Marshall, who was both integral to the data collection and interpretation for this project and in part the reason I became involved in this study. I also want to thank Drs. Jaime Barnes and James Gardner for being supportive and constructive committee members. Thank you to Ruohan Gao, who completed a similar study of Hualalai volcano and shared unpublished data for this project. Thank you to Drs. Staci Loewy and Aaron Satkoski for their help preparing and running samples for radiogenic isotope analyses. I also want to thank Dr. James Maner for his help analyzing my samples with the EMPA. In addition, I would like to thank Miguel Cisneros for helping collect O isotope data on numerous samples. Thank you to Leslie Bruce for her preliminary work collecting data on many of the samples of this study. I would also like to thank Daniel Villanueva for his continued work on these samples beyond the scope of this thesis. Thank you to Drs. Jaime Barnes and Mark Cloos for their dedication to the Honors Program and guidance in how to construct and present an honors thesis. Thank you to Dr. Ron Fodor for providing the xenolith samples that made this study possible. I would also like to thank the National Science Foundation for funding this project. Finally, thank you to the Jackson School of Geosciences for the financial and educational foundation that I could not complete this thesis without.

Abstract

Xenolith constraints on the origin of low $\delta^{18}O$ values in Mauna Kea basalts: The role of self-assimilation

Danny W. Anderson, B.S. Geological Sciences
University of Texas at Austin, 2018
Supervisor: John C. Lassiter

Several post-shield cones surrounding Mauna Kea volcano in Hawaii are marked by the presence of ultramafic and mafic cumulate xenoliths spanning a lithologic range from dunites to gabbros. These xenoliths offer a complimentary geochemical record to that provided by erupted lavas and may give insight into the dynamics of Hawaiian magma chambers and the effects of assimilation and fractional crystallization on the final melt compositions we observe at the surface. Trace-element concentrations measured in clinopyroxene suggest these xenoliths crystallized from similar parental magmas related to Mauna Kea volcanism; yet, isotopic variability precludes these samples from having formed from the same single parental magma. Compared with data from the HSDP-2 drillcore, the $^{87}Sr/^{86}Sr$ (0.70349 to 0.70357) and $^{208}Pb/^{207}Pb$ ratios (2.45 to 2.46) measured on these samples indicate they formed during the late shield stage to early post-shield transition in Mauna Kea's volcanic history. Furthermore, a positive correlation between $\delta^{18}O$ values measured in olivine (ranging from ~+3.3 to 4.8‰) and Mg# (ranging from ~0.73 to 0.90), in combination with Sr and Pb isotopic constraints, suggests that self-assimilation of hydrothermally altered, shallow edifice material has greatly lowered the $\delta^{18}O$ values in Mauna Kea lavas from expected mantle olivine values (~+5.2‰). No clear correlation between radiogenic isotope values and Mg# suggests the Pb and Sr isotope ratios of the assimilant in this process are similar to those of the parental magma, preventing the

assimilant from being an isotopically distinct material, such as lower oceanic crust (LOC). Additionally, Sr and Pb isotopes measured in samples of this study fall off of the expected mixing line between LOC and primitive Mauna Kea lavas. Additionally, the lack of anomalously high Sr isotope ratios, a typical signature of seawater interaction, rules out the possibility of submarine storage at intermediate depths. However, self-assimilation alone cannot account for the low- $\delta^{18}O$ values (~+4.7 to 4.8‰) of the most primitive xenoliths (Mg# ~0.90). When applying a binary mixing model between Sr and O isotopic values of primitive Hawaiian basalt and extremely low assimilant estimates ($\delta^{18}O$ ~0‰), assimilation of >10% edifice material would be required to lower the $\delta^{18}O$ values. Energetically, this cannot be achieved, as assimilating this amount of material cannot be done without drawing down the Mg# to more evolved values through fractional crystallization. As a result, we propose that the low $\delta^{18}O$ values in the high-Mg# xenoliths reflect the sampling of an isotopically light component of the Hawaiian plume.

Table of Contents

List of Figures

List of Tables

1. Introduction

As a model example of hotspot volcanism, the Hawaiian Island chain is one of the most comprehensively studied sets of ocean island volcanoes on the planet. The full extent of the chain covers a distance of nearly 6,000 km and possesses over 107 volcanoes (Bargar and Jackson, 1974; Clague and Dalrymple, 1987). The still-active volcanoes located at the southeast end of the chain, including the subaqueous Loihi Seamount, which lies about 30 km offshore of Hawaii Island, are the youngest examples of a volcanic trend dating back to over 75 million years ago (Clague and Dalrymple, 1987). These volcanoes remain some of our best means to learn about hotspot volcanism, and decades of work on the islands have improved our understanding of this volcanic system immensely. However, despite decades of work, there are still significant questions that remain unanswered regarding the nature of the material from which the volcanoes on these islands formed and how these volcanoes have changed over time.

Studying the Hawaiian Islands is an opportunity to "see" into the structure and dynamics of mantle plumes, the cause and evolution of hotspot volcanoes, and eruptive processes in general. Geochemistry is perhaps our best available tool to look into the complex magma generation and plumbing systems within these volcanoes. From shallow conduits and magma chambers to magma storage systems in the lower crust and even beyond, within the mantle itself, these rocks carry geochemical tracers of where they have been prior to being erupted. For instance, major-element studies of Hawaiian basalts have given us a good sense of the crystallization paths of these lavas. Geochemical analyses of xenoliths have given us evidence for deep magma storage during periods of volcanism. A scarcity of these xenoliths in other points in the life cycle of Hawaiian volcanoes suggests a transition in the depth of magma storage. This conclusion is substantiated by work on Kilauea and Mauna Kea. Studies have

managed to image shallow magma bodies beneath these volcanoes using seismic tomography (e.g., Okubo, Benz, and Chouet, 1997).

Yet, there is also substantial disagreement in the Hawaiian volcanic community. Geochemical signatures are not direct or clear signals from the mantle in which they were first generated. Despite these tracers being our best means to studying the structures and processes within these volcanoes, there is still a lot of debate surrounding many aspects of Hawaiian volcanism. Questions as fundamental as why Hawaiian volcanoes evolve through time have persisted since our earliest studies of these islands. Changes in magma supply through time, the number of distinct components within the plume, and relative contribution of the asthenosphere to the isotope ratios of these lavas still remain unexplained and fervently contested. Additionally, it is unknown precisely how processes such as assimilation, fractional crystallization, and metasomatism contribute to what we find when we study erupted material that has finally reached the surface. We also remain unsure of how and why magma storage and transport evolve through time, along with why there are geochemical and structural changes associated with different "stages" in the life cycles of Hawaiian volcanoes.

One way to resolve many of these uncertainties is by studying xenoliths, which serve to compliment the geochemical record preserved in the erupted lavas of these volcanoes. In particular, mantle xenoliths provide detail on the structure and composition of the underlying mantle itself, whereas xenoliths formed from entrained pieces of lower oceanic crust (LOC) beneath Hawaii offer geochemical constraints on potential assimilation of the Pacific plate. Magma chamber cumulate xenoliths are clusters of fractionally crystallized minerals that provide information on magma storage and evolution, as they form from the same primary magma as the lavas that ultimately erupt on the surface. Contrasts between the chemistries of erupted lavas and

magma chamber cumulates may be key to quantifying relative contributions of fractional crystallization and assimilation on the geochemical signatures carried in volcanic material at the surface.

By drawing on a number of geochemical techniques, a detailed study of magma chamber cumulate xenoliths from Mauna Kea volcano can help resolve disagreements regarding even the most fundamental problems surrounding Hawaiian volcanism, including where magma bodies are stored and what causes changes in isotopic ratios throughout the life cycle of these volcanoes. Studies of major and trace-elements on these rocks tell us whether all of these xenoliths are cogenetic and related to the same original melt, as well as recording cooling rates and equilibrium temperatures. The Mg#, a proxy for magma cooling based on the concentration of Mg relative to Fe in minerals, gives us a metric for the evolution of the primary melt and the extent of fractional crystallization on a magma body. Radiogenic isotopes offer a window into the melt source and hold evidence for assimilation. Oxygen isotope ratios can reveal signs of assimilated hydrothermally altered material, possible heterogeneities in the plume source, and potential information about the ancient slab that produced the Hawaiian hotspot. Comparisons with Mauna Kea lavas from numerous geochemical studies put age and isotopic limits on when and where processes such as assimilation could be affecting the primary magma, which can then be related to periods of Mauna Kea's volcanic and evolutionary life sequence.

2. Background

Since the early 20th century, geologists have had a great interest in the Hawaiian Islands, putting forth obscure explanations for the cause of the volcanism observed there, including immense fractures in Earth's crust (e.g., Eaton and Murata, 1960). We now interpret these islands to be the products of hotspot volcanism, invoking the role of a thermal plume extending

from deep within the mantle that resides beneath the Pacific Plate (Wilson, 1963; Christofferson, 1968; Morgan, 1972). It is thought that the hot spot beneath the Hawaiian Islands has remained relatively stationary over time, and as the Pacific Plate has moved above the plume, a series of volcanoes has been formed tracing the direction of the plate for the last nearly 80 million years (Clague and Dalrymple, 1987). As a result, the kink that connects the Emperor Seamounts to the north/northwest and the Hawaiian Ridge that stretches to the southeast is thought to be evidence for a significant change in the direction of motion of the Pacific Plate at approximately 55 million years ago (Christofferson, 1968; Clague and Dalrymple, 1987). As the plate has generally moved northward and westward through time, the youngest volcanoes lie on and around Hawaii Island, the most southeastern island in the Hawaiian Island chain.

Morgan (1971) proposed that many hotspot plumes, such as the one beneath the Hawaiian Islands, likely originate along the core-mantle boundary (CMB). Both past and recent studies of seismic data (e.g., Lay, Williams, and Garnero, 1998; Helmberger, Wen, and Ding, 1998; Zhao, 2004) trace many of these plumes, including Hawaii, to the deep lower mantle and even the CMB, substantiating this theory. One possible reason for the origin of plumes is related to a potential thermal contrast between the core and mantle across their interface. Numerous studies (e.g., Hofmann and White, 1982; Grand, van der Hilst, and Widiyantoro, 1997) have suggested that subducted slabs sink deep within the Earth's interior and can accumulate along the CMB, where they ultimately heat, melt, and occasionally become entrained within rising mantle plumes (Hofmann and White, 1982). One hypothesis, proposed by Lassiter and Hauri (1998), details the possibility for km-scale isotopic heterogeneities within these slabs of subducted lithosphere to be preserved for billion-year timescales within the resultant mantle plume. In

consequence, some of the original signatures of these ancient slabs may be preserved in ocean islands such as Hawaii (Hauri, 1996).

The Hawaiian mantle plume is commonly divided into three geochemically distinct components, known as the Loihi, Kea, and Koolau end members. The Kea and Loihi components may be derived from the melting of mantle peridotite, but studies of the Koolau component indicate that its formation is related to quartz eclogite and partial melting of a mafic source (Hauri, 1996). Figure 1 outlines the calculated relative contributions of each component to various Hawaiian volcanoes.

This heterogeneity within the plume itself is expressed on the surface as geochemical disparities between volcanoes in the Hawaiian chain. Differences in relative contributions of each component to the melt generated beneath each volcano have resulted in two sub-parallel, spatial trends characterized by differences in their chemistries in Hawaiian volcanism, known as the Kea and Loa trends (Frey et al., 2016). Figure 2 shows a map of these two trends. The Kea trend consists of Kilauea, Mauna Kea, Kohala, Haleakala, West Maui, East Molokai, and West Molokai (Frey et al., 2016). In contrast, the Loa trend is composed of Mauna Loa, Hualalai, Manukona, Kahoolawe, Lanai, and Penguin Bank (Frey et al., 2016). Hauri (1996) proposed that these two trends are the result of the geometry of the Hawaiian plume and the distribution of its components, with blobs of the Koolau end member distributed within the Loihi mantle component, which together reside beneath Loa trend volcanoes. That study suggests these components are surrounded by passively upwelling asthenosphere, thought to be the Kea end member, which contributes to the magmas of Kea trend volcanoes that reside on the periphery of the plume (Hauri, 1996). Other models of the plume have been put forth to explain these trends. Abouchami et al. (2005) use Pb isotope geochemistry to instead suggest a bilateral asymmetry

within the plume between these two trends. However, data from Ren et al. (2005), in combination with those of Xu et al. (2014), suggest that the distinction between trends is less exact, with Kea lavas sometimes erupting in Loa volcanoes and vice versa.

These volcanoes ultimately progress through a general life cycle that can be categorized into four primary stages based on a number of factors, including lava type, magma supply rate, and xenolith populations. The earliest stage, the pre-shield, is marked by frequent entrainment of lherzolite mantle xenoliths, low magma supply rates, and alkalic lavas (Clague, 1987; Garcia et al., 1995). Following the pre-shield stage is the shield stage, which marks a transition to high magma supply rates, tholeiitic lavas, and xenoliths sampling shallower depths (Clague, 1987; Watson and McKenzie, 1991). Shield stage xenoliths brought to the surface are typically smaller and rarer. In addition, the shield stage is estimated to generate approximately 95% of the total volume of Hawaiian volcanoes (Clague and Dalrymple, 1987; Watson and McKenzie, 1991). The post-shield stage that follows marks a change back to alkalic lavas and lower magma supply rates. Studies of xenoliths collected from this period of Hawaiian volcanism have suggested the xenoliths are entrained deeper beneath the volcano, during magma storage within the lower Pacific crust (e.g., Bohrson and Clague, 1988). The post-shield stage is often followed by an erosional period void of volcanic activity for approximately 0.4-2.5 million years (Clague and Dalrymple, 1987).

These stages may also be marked by differences in the structure of the plumbing and storage systems within the volcano, but precisely how and why Hawaiian magma storage systems change through stages is debated. It is thought that the pre-shield and rejuvenated stages do not maintain any magma storage systems because of low magma supply rates (Wolfe, Wise, and Dalrymple, 1997). Most generally agree that shield stage volcanoes have shallow magma

chambers beneath their calderas. We are able to image Kilauea's current magma storage reservoir, at ~5 km depth, through seismic tomography, which is strong evidence for shallow magma storage in the shield stage (Okubo, Benz, and Chouet, 1997). Whether deeper storage during the shield stage occurs as well is far less agreed upon. While xenoliths likely sampling deep portions of the Pacific oceanic crust have been found in post-shield lavas, such as Hualalai's Kaupulehu flow, providing compelling evidence for deep magma storage within post-shield volcanoes, shield stage volcanoes lack such xenoliths (Bohrson and Clague, 1988). However, additional shallow storage in the same system would filter out these xenoliths and make it difficult for them to reach the surface. This is what makes it particularly difficult to assess whether shield stage magmas have an additional magma storage zone deeper within the plate or an exclusively shallow reservoir near the caldera.

To study how these volcanoes change through their life cycles and what processes affect the chemistries of their products, we need to look at the volcanoes that are currently active within these stages of Hawaiian volcanism. The island of Hawaii contains the youngest subaerial volcanoes in the entire chain, and thus possesses the most recent accessible traces of the underlying mantle plume and magma plumbing systems within each volcano. The island's five volcanoes, Kilauea, Mauna Loa, Mauna Kea, Hualalai, and Kohala currently range from the shield to post-shield stage. Comparisons between their erupted products through time are useful indicators of how Hawaiian volcanism evolves over otherwise impossible to sample timescales. Changes in the geochemistry of these lavas between stages may also help us identify changes in magmatic source, magma storage and transport systems, and thermal gradients within the underlying mantle. They may also help explain why these volcanoes undergo life cycles at all.

Mauna Kea is an ideal study site to gain insight into Hawaiian volcanism for several reasons. The volcano is currently in its post-shield stage, meaning that it offers the opportunity to compare erupted material between the shield and post-shield stages within the same volcano. Furthermore, at approximately 1 million years old, Mauna Kea is young enough that we can access relatively fresh, unaltered rock, and its shield stage material is not buried by as much post-shield lava as some of its older counterparts (Wolfe, Wise, and Dalrymple, 1997). In addition, lavas erupted from Mauna Kea have been extensively studied through the Hawaii Scientific Drilling Project (HSDP), a two-part mission initiated in 1991 to retrieve approximately 4.6 km of rock core from Mauna Loa and Mauna Kea volcanoes. Aside from the top ~200 m, the entirety of the core records Mauna Kea's volcanic history back to ~700 ky. Data from the extensively studied HSDP-2 cores can be used complimentary to analyses of magma chamber cumulates to approximate ages of crystallization and tie geochemical signatures observed in these cumulates to stages in Mauna Kea's life cycle. As the namesake of the Kea end member within the Hawaiian plume, Mauna Kea also carries the clearest geochemical signal of that component. Additionally, because Kea trend volcanism is dominated by melts generated from the Kea end member, information on Mauna Kea is integral to understanding the trend.

3. Samples and Methods

This study analyzed 22 large (>5cm diameter) xenoliths spanning a range of lithologies, including dunites, clinopyroxenites, websterites, wehrlites, and a variety of gabbros, sampled from four different cones surrounding Mauna Kea volcano (Fig. 3 and 4). Of these rocks, two possessed pairs of composite xenoliths, single samples containing two lithologies. These samples were collected by Ron Fodor for a study that was published in 1988 (Fodor, 1988). Grains were

chiseled off of cut and exposed portions of the xenoliths, rinsed in deionized water, and sonicated repeatedly until clean.

Major-element data for opx and cpx mineral separates loaded into an epoxy grain mounts were collected using the JEOL JXA-8200 EMPA at the University of Texas at Austin. In most cases, 5-6 mineral grains per sample were analyzed, with at least 1 core and rim analysis for each sample. The average measured major-element composition of augite (Cr) standard NMNH 164905 agrees to within 1.6% of its published major-element composition for FeO, CaO, MgO, and SiO_2, and within 2.3% for Al_2O_3. Measurements of Na_2O, Cr_2O_3, and TiO_2 are accurate to within 8%, and MnO is accurate to within 11% of published values. The measurements collected for NMNH 164905 are reproducible to within 2% (2 s.d.) for FeO, CaO, MgO, and SiO_2. Values for Na_2O, Cr_2O_3, and Al_2O_3 are reproducible to within 6% (2 s.d.). The reproducibility of data collected for MnO and TiO_2 is within 15% (2 s.d.), and that of NiO is >40% (concentration is <0.1 wt. %).

Mineral separates of olivine, plagioclase, and spinel were analyzed similarly using the same EMPA used to collect major-elements for opx and cpx. In most cases, 4-6 grains for each sample were analyzed for olivine and plagioclase, with at least 1 olivine core and rim analysis per sample. For spinel, a minimum of 4 mineral grains were analyzed for most samples. Analyses were performed at 15kV accelerating voltage using a 20nA beam current with a 1µm spot for olivine and spinel and a 10µm spot for plagioclase. The average measured major-element composition of olivine standard USNM 2566 agrees to within 1% of its published major-element composition for all elements >1 weight percent and less than 10% for all elements <1 weight percent for olivine and spinel. Reproducibility of the reported major-element data for olivine and spinel is within 2% (2 s.d.) for SiO_2, FeO, and MgO and within 6% (2 s.d.) for MnO.

The average major-element concentrations measured for anorthoclase standard NMNH 133868 are accurate to within 1% for SiO_2 and K_2O, 4% for Na_2O and Al_2O_3, 15% for FeO, and 30% for CaO (concentration is <1 wt. %) for plagioclase. The values collected for NMNH 133868 are reproducible to within 2% for SiO_2, Al_2O_3, Na_2O, and K_2O, 5% for CaO, and 10% for FeO. Average concentrations measured for plagioclase standard NMNH 115900 are accurate to within 2% for SiO_2, Al_2O_3, and CaO, 4% for MgO, 10% for FeO, 12% for Na_2O, and 31% for K_2O (concentration is <0.2 weight percent). The NMNH 115900 measurements are reproducible to within 3% for SiO_2, Al_2O_3, and CaO, 4% for Na_2O, 6% for FeO, 11% for K_2O, and 18% for MgO (2 s.d.). As is shown in Figure 5, major-element data collected for these samples is orders of magnitude more precise for oxides with >5-10 wt. % concentrations.

Trace-element data were collected for opx and cpx grains by LA-ICP-MS at the University of Texas at Austin using an Agilent 7500ce quadrupole with a New Wave UP-193FX laser system. The same epoxy mounts that were analyzed for major-elements on the EMPA were reused for these analyses, and the 100µm spots were approximated to be centered on where major-elements were collected. Spots were pre-abladed with dwell times of 45 seconds. Trace-element analyses were collected using BCR-2g as a calibration standard. Reproducibility of standard NIST 612 was within 6% (2 s.d.) for all trace-elements, with the exception of Er and U, which were reproducible to within 8% (2 s.d.).

Olivine, clinopyroxene, and plagioclase $\delta^{18}O$ ($\delta^{18}O_{olv}$, $\delta^{18}O_{cpx}$, and $\delta^{18}O_{plag}$) values were measured via laser fluorination (Sharp, 1990). Approximately 2.0 mg of hand-picked, optically clear grains of each phase were used for each analysis. Each sample was analyzed one to two times per available phase, and most phases were analysed more than once. Garnet standard UWG-2 ($\delta^{18}O$ = +5.8‰) (Valley et al., 1995) and in house olivine standard San Carlos ($\delta^{18}O$ =

+5.2‰), and quartz standard Lausanne-1 ($\delta^{18}O$ = +18.1‰) were also analyzed. All $\delta^{18}O$ analyses are reported relative to standard mean ocean water (SMOW), where NBS-28 $\delta^{18}O$ = +9.7‰. The error on each analysis is ±0.1‰ (1σ) based on the long-term error of standards. During the analytical sessions for which the samples in this study were analyzed, error on UWG-2 standard was ±0.1‰ (1σ) and for San Carlos standard was better than ±0.1‰ (1σ). All olivine and clinopyroxene samples duplicated within error (Table 1).

Strontium and Pb radiogenic isotopes were measured on mineral separates digested in an HF:HNO_3 solution. Clinopyroxene grains were exclusively analyzed for 4 of these samples, and plagioclase grains were exclusively analyzed for 2 of these samples, and both phases were analyzed for 2 samples, for a total of 8 samples. Strontium and Pb were collected and purified using similar methods to those outlined in (Lassiter et al., 2003) and (Carlson and Irving, 1994). Sr and Pb were each separated using Sr-Spec and AG1-X8 resins, respectively.

Strontium was analyzed as a metal on single Re filaments using the University of Texas at Austin's Triton TIMS. All sample analyses had absolute errors less than 3*10^-6, except for the analysis of HK-1 plagioclase, which had an absolute error of 3.3*10^-6.

Lead isotopes were analyzed with a Nu Instruments *Nu Plasma III* MC-ICP-MS using a DSN 100 desolvating nebulizer. Solutions were aspirated at 100 μL/min. Samples were diluted to approximately match the total ion intensity of the standards and run at 5ppb. Instrumental mass bias was corrected for using thalium ($^{205}Tl/^{203}Tl$ = 2.389650) added to the samples with a Pb/Tl ratio of ~10 and then normalized to NBS 981. Based on the precision of standard analyses of NBS-981, the uncertainty in $^{206}Pb^{204}Pb$, $^{207}Pb/^{204}Pb$, and $^{208}Pb/^{204}Pb$ ratios is estimated to be 0.004% per amu (2SD, n = 5). The uncertainty of these ratios based on the precision of standard

analyses of NBS-982 is 0.005% per amu (2SD, n = 5). The uncertainty of these ratios based on the precision of standard analyses of BHVO-2 is 0.006% per amu (2SD, n = 2).

4. Results

Petrography

Thin sections for all samples were used to make detailed petrographic and mineralogical observations. A few samples, namely D-4, HC-18 CG, HC-18 FG, HC-25 D, HC-26, and HC-76, have kink bands in olivine and pyroxene grains, which is evidence for small-scale deformation within the magma chamber (Fig. 6). One sample, H-17, shows possible preferred crystal orientations or perhaps a recrystallization structure (Fig. 7). Trace amounts of biotite in two samples, D-4 and H-17, show evidence for the presence of small amounts of water during crystallization (Fig. 7). The lack of biotite in the remaining samples may be the result of low oxygen fugacity within the magma chamber. Additionally, HC-10 possesses compositional pyroxene-rich and pyroxene-poor banding, as seen in Figure 8. By studying these thin sections in detail, we separated the samples by mineralogy as follows: 3 wehrlites, 1 websterite, 5 olivine gabbros, 3 gabbronorites, 4 gabbros, 5 dunites, and 1 clinopyroxenite. The gabbros and gabbronorites could further be separated according to their pyroxenes. Those that contained clinopyroxene (cpx) and orthopyroxene (opx) were considered 2-pyroxene, and those with cpx alone were 1-pyroxene. These lithologies were grouped into four categories: 1) dunites and wehrlites, 2) 2-pyroxene gabbros, olivine gabbros, and gabbronorites, 3) 1-pyroxene gabbros, olivine gabbros, and gabbronorites, and 4) clinopyroxenites and websterites. Table 2 lists the mineralogy and classification of each sample.

Major-Elements

Major-element compositions for cpx, opx, olivine, plagioclase, and spinel are reported in Tables 3-7. Measurements of major-element compositions in cpx reveal that Mg# ($Mg\#_{cpx}$, calculated as molar $Mg/(Mg+Fe_{total})$) ranges from ~0.75 to 0.90. Olivine Mg# ($Mg\#_{olv}$) ranges from ~0.73 to 0.87, with a constant $Mg\#_{cpx}$-$Mg\#_{olv}$ offset of ~0.01 to 0.05. There is the exception of three samples (HC-25 Light, H-17, and HC-52), which each possess $Mg\#_{olv}$ values that are consistently ~0.01 to 0.04 higher than their $Mg\#_{cpx}$ counterparts (Fig. 9). Core and rim data collected on most pyroxene and olivine grains show little major-element variation (typically ±<0.5 wt. % intra-grain variation). Furthermore, the variability of major-element compositions between grains of the same sample is low. Across a single sample, the $Mg\#_{cpx}$ in different grains varies by ±<0.01. Only one sample, HC-10, has an inter-grain $Mg\#_{cpx}$ variation that is higher, at ±0.03. Likewise, across single samples, the $Mg\#_{olv}$ in different grains varies by ±<0.01. There is much less variation (±<0.01 variation between grains of the sample) in the $Mg\#_{olv}$ data for HC-10.

Trace-Elements

Trace-element concentrations were collected on all cpx and opx grains analyzed for major-elements, and these data were normalized to estimated pyrolite values reported in McDonough and Sun (1995). The non-normalized trace-element values (in ppm) are reported in Tables 8 and 9. Spider diagrams and REE plots show enrichment in MREEs, relative to HREE and LREE values (Fig. 10 and 11). Values of Eu/Eu* were calculated for cpx in each sample as $[Eu]_{norm}/sqrt([Sm]_{norm}*[Gd]_{norm})$ and range from 0.68-1.03. Similarly, Sr/Sr* was calculated for cpx in each sample as $[Sr]_{norm}/sqrt([Pr]_{norm}*[Nd]_{norm})$, with values ranging from 0.04 to 0.98.

Furthermore, Ti/Ti* values in cpx grains for all samples were calculated as $[Ti]_{norm}/sqrt([Eu]_{norm}*[Gd]_{norm})$, with values ranging from 0.11 to 1.26.

Stable and Radiogenic Isotopes

Oxygen isotope data are reported in Table 1. Oxygen isotope values measured in cpx grains ($\delta^{18}O_{cpx}$) range from +3.47 to 4.54‰. Oxygen isotope values measured in olivine grains ($\delta^{18}O_{olv}$) range from +3.35 to 4.77‰. Oxygen isotope values measured on plagioclase grains ($\delta^{18}O_{plag}$) range from +4.4 to 5.1‰. For samples where both phases were measured, no average offset was observed between $\delta^{18}O_{cpx}$ and $\delta^{18}O_{olv}$, though values varied by ±0.2‰ (Fig. 12)

Strontium and Pb isotopic data are reported in Tables 10 and 11. The Sr isotopic ratios show little variability, ranging from 0.70349 to 0.70357. Pb isotopes also fall within a narrow range, with $^{206}Pb/^{204}Pb$ lying between 18.37 and 18.52 and $^{208}Pb/^{204}Pb$ spanning from 37.98 to 38.10. In comparison to other Hawaiian volcanoes, these samples appear relatively unradiogenic with regard to Sr, though they fall in a normal region for Mauna Kea lavas (Fig. 13). By contrast, Pb isotopes appear relatively radiogenic compared to other Hawaiian volcanoes (Fig. 13).

5. Discussion

Origin of Mauna Kea Xenoliths

In order to make interpretations about the evolution of Mauna Kea's magma storage system and the processes that affect it, we must understand how the xenolith samples of this study formed and relate to Mauna Kea as a whole. Petrographic observations provide insight into the physical effects of crystallization of different phases. There is evidence for solid-state deformation from kink bands and preferred crystal orientations or potential recrystallization patterns in some samples (Fig. 6 and 7). There are also signs of trace amounts of water in some xenoliths in the form of biotite (Fig. 7).

Geochemically, trace-element data show that these samples follow similar crystallization sequences consistent with the progression of fractional crystallization we observe in typical Hawaiian lavas. Strontium and Eu in many cpx grains measured in samples of this study show decreases in concentrations consistent with the formation of plagioclase at typical Mg# values observed in other Hawaiian studies (e.g., Yang and Frey, 1996). Figure 14 shows a correlation between Sr/Sr^*_{cpx} and Eu/Eu^*_{cpx} related to the lithology of each sample. In particular, samples that crystallized from a more primitive magma (the dunites marked with dark gray circles) tend to have Sr and Eu anomaly values close to 1. This can also be seen in Figure 10, where the dunites have no apparent relative enrichment or depletion of Sr or Eu. Figures 15a and 15b show the relationships between Sr/Sr^*_{cpx} and Eu/Eu^*_{cpx} and $Mg\#_{cpx}$, respectively. Again, these plots indicate that more primitive magmas produce cpx crystals with Sr and Eu anomaly values near 1. Conversely, samples formed from more evolved melts, such as the gabbros (light gray squares and diamonds), appear to have lost Sr and Eu, relative to their neighboring trace-elements, as indicated by Figure 10. Just as the more primitive dunites plot at higher Sr and Eu anomaly values in Figure 14, the more evolved gabbros fall in a region with much lower Sr and Eu anomaly values. The low Sr/Sr^*_{cpx} and Eu/Eu^*_{cpx} values in samples with higher $Mg\#_{olv}$ can also be observed in Figures 15a and 15b. These trends are all indications that the changes in Sr and Eu anomalies are linked to the evolution of the primary magma and likely the crystallization of plagioclase. As plagioclase forms within the magma chamber, its crystal lattice allows the substitution of Sr and Eu for Ca, leaving the melt relatively depleted in these-elements, as recorded in the samples of this study. Studies of the HSDP-2 drill core have shown the timing of crystallization for different phases to occur along a similar path to the samples of this study (Yang and Frey, 1996). The CaO and Al_2O_3 major-element contents of Mauna Kea basalts

indicate that the formation of clinopyroxene and plagioclase are expected to begin formation at Mg#s around 0.86, which is the approximate composition of the samples of this study (Yang and Frey, 1996; Wolfe, Wise, and Dalrymple, 1997).

Trace-element concentrations in these samples appear to be related to the crystallization of different phases, including olivine, plagioclase, and pyroxene, suggesting they formed along a similar crystallization path. However, this relationship in trace-elements cannot explain the isotopic variations in the same samples, an indication that while they follow similar sequences in crystallization, they are not derived from the same, parental magma. If these samples crystallized from a common original melt, we would expect to see little isotopic variability, as crystallization cannot fractionate Sr or Pb isotopes. Yet, when we look at the measured isotopes in these xenoliths, their values range substantially, which cannot be explained without additional processes at work, which will be discussed more thoroughly later.

Relative Timing of Crystallization

Past studies of the HSDP-2 drill core (e.g., Blichert-Toft, 2003; Bryce, DePaolo, and Lassiter, 2005) have noted distinct isotopic changes between different stages of Hawaiian volcanism, which we can use to constrain the timing of crystallization for these xenoliths relative to the life cycle of Mauna Kea. Figure 13 shows the different regions in which Mauna Kea shield and post-shield stage lavas fall on a plot of $^{87}Sr/^{86}Sr$ versus $^{206}Pb/^{204}Pb$. The transition between the shield and post-shield stages of Mauna Kea volcanism is marked by a shift towards less radiogenic Sr and Pb isotope ratios. Plotting the data of this study against these shield and post-shield regions, we find a correlation between $^{87}Sr/^{86}Sr$ and $^{206}Pb/^{204}Pb$ that falls along this transition between stages. This suggests that these xenoliths crystallized during the late shield to early post-shield period in Mauna Kea's volcanic history. Simple estimated age versus depth

curves developed by Bryce, DePaolo, and Lassiter (2005) using parameters from Sharp and Renne (2005) and DePaolo and Stolper (1996) can be used to relate the age of the HSDP-2 drill core to depth. Isotope ratio versus depth curves made using the data from the HSDP-2 drill core (Fig. 16a and 16b) again show a clear shift in radiogenic isotopes associated with the change between shield and post-shield stages.

The cause of the transition in isotopic values between stages of Hawaiian volcanism is not well understood. Previous studies (e.g., Eiler et al., 1996) have hypothesized that the change in Sr and Pb isotopes between Hawaiian shield and post-shield stages is linked to a shift to deeper magma storage and the assimilation of lower oceanic crust (LOC) near the Moho. The correlation between Sr and Pb isotope values in the Mauna Kea xenoliths of this study shows a positive, linear trend, as shown in Figures 13 and 17. This correlation could reflect a combination between a Mauna Kea shield stage end member and incorporated, relatively unradiogenic material, possibly the assimilated LOC that has been argued for (Eiler et al., 1996). Our best estimates for the geochemical composition of Hawaiian LOC comes from analyses of gabbroic xenoliths entrained in the Kaupulehu flow (Gao et al., 2016). However, by comparing the LOC isotopic values collected on the xenoliths from the Kaupulehu flow (from Gao et al., 2016 and Gao et al., personal comm.) to the data of this study, together with HSDP-2 drill core lavas (Fig. 13), we find that the region that defines LOC isotope ratios does not fall on the extension of the line (Fig. 13) produced by the trend in the xenoliths of this study. Strontium isotope values are extremely low in LOC by comparison to Hawaiian lavas. Even low amounts of assimilation of this material would shift the values of the post-shield lavas to $^{87}Sr/^{86}Sr$ levels that are far too isotopically depleted, failing to produce the linear correlation observed in these samples. Furthermore, as Figure 13 shows, LOC is isotopically distinct, and the associated effects that

assimilation would have on the isotopes should be reflected in Sr and Pb versus Mg# plots (Fig. 18a-d). However, as will later be discussed in more detail, there is no correlation between these values. Thus, the cause of the isotopic differences between stages of volcanism are likely from the mantle source, though whether these are intrinsic heterogeneities within the plume or the product of mixing between the plume and asthenosphere is unclear.

Xenolith Thermal Histories

A two-pyroxene major-element thermometer developed by Brey and Köhler (1990) was used to estimate crystallization temperatures for samples with the available phases. Approximating pressures of 2.5kbars, the calculated T_{BKN} values range from 886 to 964°C. Using the major-element data collected with the EMPA on olivine and spinel grains, we also calculated equilibrium temperatures ranging from 976 to 1015°C as outlined in Ballhaus et al. (1991). In combination with the major-element thermometers, a two-pyroxene REE thermometer developed by Liang et al. (2013) was used to estimate equilibrium temperatures for five samples. The calculated T_{REE} values range from 1242 to 1486°C, with errors between ±14 to 100°C. All thermometry values are listed in Table 12.

Using these thermometers, we can determine the thermal structure of Mauna Kea's magma storage system. The calculated equilibrium temperatures for cpx and opx grains, recorded in trace-element concentrations (T_{REE}), are near-magmatic temperatures, and thus, they are likely good approximations of magma chamber temperatures stored at shallow depths within the subaerial portion of Mauna Kea volcano. In contrast to these T_{REE} values, calculated equilibrium temperatures for the same phases recorded in major-element concentrations (T_{BKN}) are substantially lower by ~400 to 600°C (Fig. 19a-e, 20). Furthermore, temperatures calculated from major-elements in olivine and spinel grains show similarly cool temperatures. We interpret

the differences between these three thermometers to be related to sub-solidus cooling, with T_{REE} preserving near-solidus temperatures within the magma chamber, which would be ~1300 to 1400°C. Dygert and Liang (2015) have proposed that the T_{REE} is effectively a REE diffusion closure temperature, beyond which REEs are unable to continue to exchange between mineral grains. Figure 19a-e shows that some of the REEs were out of equilibrium, and they were thus excluded from the calculation. Similarly, T_{BKN} is related to the thermal limit at which major-element cations can exchange between opx and cpx grains for given pressures. Diffusion rate is inversely proportional to closure temperature, and because major-elements (particularly Mg, Fe, and Ca) diffuse at faster rates, the temperatures they record in pyroxenes are lower than what is preserved in REEs (Dygert and Liang, 2015). In comparison to the findings in Dygert and Liang (2015), we find that the samples of this study cooled at relatively fast rates (~1,000-10,000°C per Mya) (Fig. 20). However, it is important to note that this calculation depends on grain size. The xenoliths with calculated temperatures have very similar grain sizes, but it is difficult to extrapolate how they compare to the samples of the Dygert and Liang (2015) study. Modeled cooling rates assume 5mm diameter, spherical grains, but the samples of this study are typically smaller and less uniform. These estimated cooling rates serve as first order approximations of the thermal histories of these xenoliths.

Model for Self-Assimilation of Edifice Material

In previous studies, assimilation is one proposed explanation for the unusually low $\delta^{18}O$ values found in the erupted products of Kea trend volcanoes (e.g., Eiler et al., 1996, Garcia et al., 1998, Wang and Eiler, 2008). It has been shown that O isotope values can be significantly changed by assimilation of rocks that have been hydrothermally altered (e.g., Taylor, 1974). Thus, O isotopes may be useful to determine the degree to which assimilation processes have

affected the chemistry of Hawaiian volcanoes. In contrast to the standard mantle olivine values, which are consistently ~+5.2‰, Mauna Kea lavas are characterized by $\delta^{18}O_{olv}$ values typically ranging from ~+4.6 to at maximum ~+5.2‰ (Eiler et al., 1996; Fodor and Galar, 1997; Garcia et al., 1998; Wang and Eiler, 2008). Numerous theories have been proposed to explain the dominant control on these ^{18}O depleted values. One hypothesis is assimilation of low $\delta^{18}O$, hydrothermally altered gabbros from the lower oceanic crust at the base of the Pacific oceanic crust (Eiler et al., 1996; Wang and Eiler, 2008). Such gabbros are predicted to possess $\delta^{18}O$ values of approximately +2.0 to +2.5‰, and it has been supposed that sufficient assimilation could bring Kea trend lava values down to the range we see (Eiler et al., 1996). These estimates of the LOC isotopic values come from studies of ophiolite suites, which contain lower sheeted dikes and gabbros possessing whole rock $\delta^{18}O$ values ranging from ~+1.5 to +11.5‰ (Gregory and Taylor, 1981). An alternative hypothesis is that the magma body assimilated volcanic edifice material formed from hydrothermally altered previously erupted lava (Garcia et al., 1998; Wang and Eiler, 2008). This explanation would suggest that there is no correlation between radiogenic isotopes and tracers of these AFC processes, such as O isotopes (as a proxy for assimilation) and Mg# (as a proxy for magma cooling), since the magma and assimilant would be derived from the same source. A third hypothesis is there are isotopic heterogeneities within the mantle plume source beneath Hawaii from which the melts were originally derived (Lassiter and Hauri, 1998). As has been previously discussed, it is possible that the proposed heterogeneities originate from geochemically distinct regions of the subducted slab (i.e., the low $\delta^{18}O$ values come from the lower crust or lithospheric mantle from an ancient slab source) (Lassiter and Hauri, 1998). Using geochemical trends in the data collected from this study, we will evaluate and test these hypotheses.

A relationship between measured $\delta^{18}O$ values and Mg# (Fig. 21) in the samples of this study supports the hypothesis that assimilation has occurred and resulted in the low $\delta^{18}O$ values measured at Mauna Kea. DePaolo (1981) proposed that the energy lost from cooling a magma body and initiating fractional crystallization would be coupled with the heating and potential melting of wallrock within a magma chamber. Quantitative modeling explored by Spera and Bohrson (2001) and Bohrson and Spera (2001) but energetic constraints on this coupling. As an indicator of the extent of fractional crystallization and cooling that occurs within a magma chamber, the Mg# is potentially related to the heating and incorporation of additional solid material through these assimilation-fractional crystallization (AFC) processes. The positive correlation between $\delta^{18}O$ values and Mg# in Mauna Kea xenoliths shown in Figure 21 suggests that low $\delta^{18}O$ values are related to the evolution of the primary magma and the amount of assimilation increases with increasing fractional crystallization. More fractional crystallization within the magma body drives the Mg# to lower values, which is energetically paired with the assimilation of low-$\delta^{18}O$ material and a subsequent decrease in O isotope values.

Although the relationship between $\delta^{18}O$ and Mg# in the xenoliths of this study suggests that AFC processes are occurring within Mauna Kea, it is unclear what the assimilant is. As has been discussed, it is possible that assimilation of LOC is the source of the low $\delta^{18}O$ values. Plotting data from these xenoliths against a simple binary mixing model between expected O and Sr isotopic values for LOC and those of primitive Hawaiian basalt (Fig. 22), we find that these samples fall off of the anticipated curve. As shown in Figure 22, the Sr isotope values measured in these xenoliths do not span the necessary range to fit the mixing model. This precludes assimilation of LOC from explaining the correlation between $\delta^{18}O$ and Mg#. Furthermore, comparisons of Sr and Pb isotopes versus Mg# (Fig. 18a-d) show that there is no relationship

between radiogenic isotopes and assimilation, which we would not expect from mixing the isotopically distinct Pacific crust with magma originating from the Hawaiian plume.

The lack of correlation between Sr and Pb isotopes and Mg# can instead be explained by assimilation of hydrothermally altered, volcanic edifice within Mauna Kea (e.g., Garcia et al., 1998; Wang and Eiler, 2008). If this were the case, any AFC process modifying the O isotope values would have no clear effect on Sr and Pb isotopes, since the assimilant would be related to the same source: the Kea end member of the mantle plume. Thus, while assimilation of edifice material would change O isotopes significantly as a function of magma evolution (i.e., Mg#), there would be no observed difference in the radiogenic isotopic values.

The data collected on the samples of this study substantiate what was proposed by Wang and Eiler (2008), who suggested that low O isotope values in Mauna Kea olivines are the products of self-assimilation of volcanic edifice material. Figure 23 shows how the data of this study relate to the measurements collected in the Wang and Eiler (2008) study. The data from this study show much lower Mg#s and $\delta^{18}O$ values that follow the same trend observed in Wang and Eiler (2008). Our data support that self-assimilation is likely occurring within a shallow magma chamber reservoir beneath Mauna Kea, which bolsters the hypothesis outlined by Wang and Eiler (2008).

On account of the lack of high-Sr isotope anomalies in the low- $\delta^{18}O$ value xenoliths, these samples appear to be missing a "seawater signature" from the edifice assimilant. Material hydrothermally altered by seawater will have $^{87}Sr/^{86}Sr$ ratios significantly higher than primitive Mauna Kea magmas. We interpret the absence of this signature to mean that this assimilation process occurred in shallow magma storage reservoirs of the subaerial portion of the volcano via interaction with meteoric water. Unlike the interpretations of O isotopes in other studies (e.g.,

Eiler et al., 1996), our hypothesis that these $\delta^{18}O$ values reflect shallow AFC processes and assimilation of volcanic edifice suggests that these low $\delta^{18}O$ values are not tied to deeper processes at the base of the oceanic crust beneath Hawaii or even within submarine portions of the volcano at intermediate depths.

The isotopic evidence that assimilation and fractional crystallization are largely occurring at shallow depths (<4km) holds important implications for what we know and understand about magma storage during shield stage Hawaiian volcanism. Supposing that assimilation of LOC is responsible for low O isotope values (e.g., Eiler et al., 1996), requires magma storage at depths near the Moho, where the base of the Pacific oceanic crust can be melted and incorporated into the magma body. However, in order to preserve the primitive sample Mg#s of ~0.90 by the time they reach magma storage in the subaerial portion of Mauna Kea, the primary magma cannot have lost much or any heat assimilating material at lower depths near the base of the crust. If these xenoliths crystallized at very shallow depths beneath Mauna Kea, it is unlikely that there is a deeper magma storage reservoir in which these magmas first ponded before continuing towards the surface. Assimilation of shallow edifice that has not been altered by seawater will have no substantial effect on radiogenic isotope values, and no other significant interaction between the magma and the crust suggests that studies of Hawaiian shield stage lava radiogenic isotopes are near-direct reflections of the underlying mantle plume.

Interpretations from the Mantle Source

While the role of self-assimilation is critical in producing low- $\delta^{18}O$ values in Mauna Kea lavas, this process alone is insufficient to explain these measurements. Again looking at the mixing model in Figure 22, the minimum amount of assimilation required to produce the $\delta^{18}O$ values measured in the more primitive samples makes no energetic sense. Even using extreme

assimilant O isotope values of ~0‰, >10% assimilation would need to occur for a sample with Mg# of ~0.90 to produce $\delta^{18}O$ values of ~+4.7 to 4.8‰ (Fig. 22). With the introduction of this volume of material, assimilation would drive cooling and fractional crystallization of the primary magma, resulting in more evolved Mg#s. This cannot account for the preservation of the primitive Mg#s measured on several xenoliths and thus cannot be the only source contributing to the low O isotope values. Some of the data presented in Wang and Eiler (2008) supports this hypothesis as well. Several of the samples have $\delta^{18}O$ values of ~4.7 to 4.8‰ and Mg#s of ~0.90, which again suggests some of these more primitive xenoliths are sampling a depleted plume component (Fig. 23). Wang and Eiler (2008) interpret these data to be related to olivine "xenocrysts" out of thermodynamic equilibrium with the evolving primary magma, which is experiencing open-system differentiation; however, this alone cannot explain the extreme amount of assimilation that would be necessary to bring these O isotope values down to those we observe in the samples of this study. Thus, we invoke the role of an isotopically light component of the mantle, sampled by the more primitive xenoliths of this study.

As has already been discussed, Lassiter and Hauri (1998) have theorized that km-scale heterogeneities within a subducted slab may be preserved for long timespans within mantle plumes such as the one beneath Hawaii. An isotopically light component of the Hawaiian plume originating from the lower crust of the ancient slab could account for the intrinsically low $\delta^{18}O$ values of the primary magmas within Mauna Kea. In conjunction with self-assimilation of the edifice, a magma that samples this O isotope-depleted plume component could produce both the correlation between $\delta^{18}O$ and Mg# and the deviation from typical mantle O isotope values we find in the high Mg# samples.

6. Future Work

We are currently in the process of analyzing several additional samples, for which we already have O isotope data, to collect more radiogenic isotopic values. Many of these samples were purposely selected for their high Mg# values. These additional data can be used to see how the most primitive samples relate to Hawaii Island as a whole and Mauna Kea lavas through time. This may give us our most clear view into the original primary melt within the magma chamber prior to assimilation, which may be the key to understanding whether magma is stored at deep levels near the base of the Pacific plate prior to ponding much closer to the surface.

In addition, there are hundreds of other unanalyzed xenoliths in our possession to strengthen this dataset with. These could be used to fill in gaps in our O isotope dataset, and provide a greater range of Mg#s with which to see the effects of assimilation processes on the primary magma. Further analyses of extremely primitive samples could offer clarity on the intrinsically light component of the Hawaiian plume we propose in this study.

Future studies of other related volcanoes may help us understand why Mauna Kea self-assimilates while other volcanoes, such as Mauna Loa and Hualalai, which have more mantle-like O isotope values apparently do not. It is also important to substantiate our observations at Mauna Kea with data from other Kea trend lavas to confirm the interpretations drawn in this study.

7. Conclusions

We conclude that the mafic and ultramafic xenoliths of this study are the volcanic products of a transition period from the shield to the post-shield stages, as marked by a distinct change in radiogenic isotope ratios. They record a series of temporal and evolutionary snapshots of the effects of assimilation and fractional crystallization within different magma bodies all following similar crystallization sequences within the subaerial portion of Mauna Kea. We find

that low $\delta^{18}O$ values in Mauna Kea lavas are evidence of 1) self-assimilation of hydrothermally altered, shallow edifice within the volcano, and 2) an isotopically light component of the Hawaiian plume related to heterogeneities originating in the slab source material. An observed positive correlation between $\delta^{18}O$ and Mg# supports assimilation, but comparisons of $^{87}Sr/^{86}Sr$ ratios between primitive Hawaiian basalt and LOC reveal a lack of radiogenic isotopic variability between the primary magma and the assimilant. Furthermore, assimilation of even extreme low-$\delta^{18}O$ value material alone violates energetic constraints and cannot account for the O isotope values of xenoliths associated with a primitive primary magma. Discrepancies between major-element and trace-element thermometers reflect sub-solidus cooling of the phases within these samples, suggesting relatively moderate cooling rates.

References

Abouchami, W., Hofmann, A.W., Galer, S.J.G., Frey, F.A., Eisele, J., Feingenson, M., 2005. Lead isotopes reveal bilateral asymmetry and vertical continuity in the Hawaiian mantle plume. Nature 434, 851-856.

Ballhaus, C., Berry, R.F., Green, D.H., 1991. High pressure experimental calibration of the olivine-orthopyroxene-spinel oxygen geobarometer: implications for the oxidation state of the upper mantle. Contrib. Mineral Petrol. 107, 27-40.

Bargar, K.E., Jackson, E.D., 1974. Calculated volumes of individual shield volcanoes along the Hawaiian-Emperor chain. Jour. Research U.S. Geol. Survey 2 (5), 545-550.

Bilchert-Toft, J., Weis, D., Maerschalk, C., Agranier, A., Albarede, F., 2003. Hawaiian hot spot dynamics as inferred from the Hf and Pb isotope evolution of Mauna Kea volcano. Geochem. Geophys. Geosyst. 4 (2).

Bohrson, W.A., Spera, F.J., 2001. Energy-Constrained Open-System Magmatic Processes II: Application of Energy-Constrained Assimilation–Fractional Crystallization (EC-AFC) Model to Magmatic Systems. Jour. of Petrol. 42 (5), 1019-1041.

Brey, G.P., Kohler, T., 1990. Geothermobarometry in four-phase lherzolites II. New thermobarometers, and practical assessment of existing thermobarometers. Jour. of Petrol. 31 (6), 1353-1378.

Bryce, J.G., DePaolo, D.J., Lassiter, J.C., 2005. Geochemical structure of the Hawaiian plume: Sr, Nd, and Os isotopes in the 2.8 km HSDP-2 section of Mauna Kea volcano. Geochem. Geophys. Geosyst. 6 (9).

Christofferson, E., 1968. The relationship of sea-floor spreading in the Pacific to the origin of the Emperor Seamounts and the Hawaiian Island Chain (abstract). Eos Trans. AGU, 49, 214.

Clague, D.A., 1987. Hawaiian xenolith populations, magma supply rates, and development of magma chambers. Bull. Volcanol. 49, 577-587.

Clague, D.A., Dalrymple, G.B., 1987. The Hawaiian-Emperor volcanic chain geologic evolution. U.S. Geol. Survey Prof. Paper, 1 (1350) 5-54.

DePaolo, D.J., 1981. Trace element and isotopic effects of combined wallrock assimilation and fractional crystallization. Earth Planet. Sci. Lett. 53 (2), 189-202.

DePaolo, D.J., Stolper, E.M., 1996. Models of Hawaiian volcano growth and plume structure: Implications of results from the Hawaii Scientific Drilling Project. Jour. of Geophys. Research 101 (B5), 11,643-11,654.

Dygert, N., Liang, Y., 2015. Temperatures and cooling rates recorded in REE in coexisting pyroxenes in ophiolitic and abyssal peridotites. Earth Planet. Sci. Lett. 420, 151-161.

Eaton, J.P., Murata, K.J., 1960. How Volcanoes Grow: Geology, geochemistry, and geophysics disclose the constitution and eruption mechanism of Hawaiian volcanoes. Science 132 (3432), 925-938.

Eiler, J.M., Farley, K.A., Valley, J.W., Hofmann, A.W., Stolper, E.M., 1996. Oxygen isotope constraints on the sources of Hawaiian volcanism. Earth Planet. Sci. Lett. 144, 453-468.

Fodor, R.V., Galar, P., 1997. A view into the subsurface of Mauna Kea volcano, Hawaii: Crystallization processes interpreted through the petrology and petrography of gabbroic and ultramafic xenoliths. Jour. of Petrol. 38 (5) 581-624.

Fodor, R.V., Vandermeyden, H.J., 1988. Petrology of gabbroic xenoliths from Mauna Kea volcano, Hawaii. Jour. of Geophys. Research 93 (B5), 4,435-4,452.

Frey, F.A., Huang, S., Xu, G., Jochum, K.P., 2016. The geochemical components that distinguish Loa- and Kea-trend Hawaiian shield lavas. Geochim. et Cosmochim. 185, 160-181.

Gao, R., Lassiter, J.C., Barnes, J.D., Clague, D.A., Bohrson, W.A., 2016. Geochemical investigation of gabbroic xenoliths from Hualalai volcano: implications for lower oceanic crust accretion and Hualalai volcano magma storage system. Earth Planet. Sci. Lett. 442, 162-172.

Gao et al., personal communications.

Garcia, M.O., Foss, D.J., West, H.B., Mahoney, J.J., 1995. Geochemical and Isotopic Evolution of Loihi Volcano, Hawaii. Jour. of Petrol. 36 (6), 1647-1674.

Garcia, M.O., Ito, E., Eiler, J.M., Pietruszka, A.J., 1998. Crustal contamination of Kilauea volcano magmas revealed by oxygen isotope analyses of glass and olivine from Puu Oo eruption lavas. Jour. of Petrol. 39 (5), 803-817.

Grand, S.P., van der Hilst, R.D., Widiyantoro, S., 1997. Global seismic tomography: A snapshot of convection in the Earth. GSA Today 7 (4), 1-7.

Gregory, R.T., Taylor, H.P., 1981. An oxygen isotope profile in a section of Cretaceous oceanic crust, Samail Ophiolite, Oman: Evidence for $\delta^{18}O$ buffering of the oceans by deep (>5 km) seawater-hydrothermal circulation at mid-ocean ridges. Jour. of Geophys. Research 86 (B4), 2737-2755.

Hauri, E.H., 1996. Major-element variability in the Hawaiian mantle plume. Nature 382, 415-419.

Hofmann, A.W., White, W.M., 1982. Mantle plumes from ancient oceanic crust. Earth Planet. Sci. Lett. 57 (2), 421-436.

Helmberger, D.V., Wen, L., Ding, X., 1998. Seismic evidence that the source of the Iceland hotspot lies at the core-mantle boundary. Nature 396, 251-255.

Lay, T., Williams, Q., Garnero, E.J., 1998. The core-mantle boundary layer and deep Earth dynamics. Nature 392 461-468.

Lassiter, J.C., Hauri, E.H., 1998. Osmium-isotope variations in Hawaiian lavas: evidence for recycled oceanic lithosphere in the Hawaiian plume. Earth Planet. Sci. Lett. 164, 483-496.

Liang, Y., Sun, C., Yao, L., 2013. A REE-in-two-pyroxene thermometer for mafic and ultramafic rocks. Geochim. et Cosmochim. 102, 246-260.

McDonough, W.F., Sun, S.S., 1995. The composition of the Earth. Chem. Geol. 120 (3) , 223-253.

Morgan, W.J., 1971. Convection plumes in the lower mantle. Nature 230, 42-43.

Morgan, W.J., 1972. Deep mantle convection plumes and plate motions. Amer. Assoc. Petrol. Geol. Bull. 56 (2), 203-213.

Okubo, P.G., Benz, H.M., Chouet, B.A., 1997. Imaging the crustal magma sources beneath Mauna Loa and Kilauea volcanoes, Hawaii. Geology 25 (10), 867-870.

Ren, Z., Ingle, S., Takahashi, E., Hirano, N., Hirata, T., 2005. The chemical structure of the Hawaiian mantle plume. Nature 436, 837-840.

Sharp, Z.D., 1990. A laser-based microanalytical method for the *in situ* determination of oxygen isotope ratios of silicates and oxides. Geochim. et Cosmochim. 54 (5), 1353-1357.

Sharp, W.D., Renne, P.R., 2005. The $^{40}Ar/^{39}Ar$ dating of core recovered by the Hawaii Scientific Drilling Project (phase 2), Hilo, Hawaii. Geochem. Geophys. Geosyst. 6 (4).

Spera, F.J., Bohrson, W.A., 2001. Energy-Constrained Open-System Magmatic Processes I: General Model and Energy-Constrained Assimilation and Fractional Crystallization (EC-AFC) Formulation. Jour. of Petrol. 42 (5), 999-1018.

Swanson, D.A., Duffield, W.A., Fiske, R.S., 1976. Displacement of the south flank of Kilauea volcano: The result of forceful intrusion of magma into the rift zones. U.S. Geol. Survey Prof. Paper 963, 1-39.

Taylor, H.P., 1974. The application of oxygen and hydrogen isotopes studies to problems of hydrothermal alteration and ore deposition. Econ. Geol. 69 (6), 843-883.

Valley, J.W., Kitchen, N., Kohn, M.J., Neindorf, C.R., Spicuzza, M.J., 1995. UWG-2, a garnet standard for oxygen isotope ratios: Strategies for high precision and accuracy with laser heating. Geochim. et Cosmochim. 59 (24), 5223-5231.

Wang, Z., Eiler, J.M., 2008. Insights into the origin of low-$\delta^{18}O$ basaltic magmas in Hawaii revealed from in situ measurements of oxygen isotope compositions of olivines. Earth Planet. Sci. Lett. 269, 377-387.

Watson, S., McKenzie, D., 1991. Melt Generation by Plumes: A Study of Hawaiian Volcanism. Jour. of Petrol. 32 (3), 501-537.

Wilson, J.T., 1963. A possible origin of the Hawaiian islands. Can. Jour. Phys. 41, 863-870.

Wolfe, E.W., Wise, W.S., Dalrymple, G.B., 1997. The geology and petrology of Mauna Kea volcano, Hawaii –A study of postshield volcanism. U.S. Geol. Survey Prof. Paper 1557, 1-129.

Xu, G., Huang, S., Frey, F.A., Blichert-Toft, J., Abouchami, W., Clague, D.A., Cousens, B., Moore, J.G., Beeson, M.H., 2014. The distribution of geochemical heterogeneities in the source of Hawaiian shield lavas as revealed by a transect across the strike of the Loa and Kea spatial trends: East Molokai to West Molokai to Penguin Bank. Geochem. et Cosmochim. 132, 214-237.

Yang, H.-J., Frey, F.A., Rhodes, J.M., Garcia, M.O., 1996. Evolution of Mauna Kea volcano: Inferences from lava compositions recovered in the Hawaii Scientific Drilling Project. Jour. of Geophys. Research 101 (B5), 11,747-11,767.

Zhao, D., 2004. Global tomographic images of mantle plumes and subducting slabs: insight into deep Earth dynamics. Phys. of the Earth and Planet. Int. 146 (1-2), 3-34.

Figures

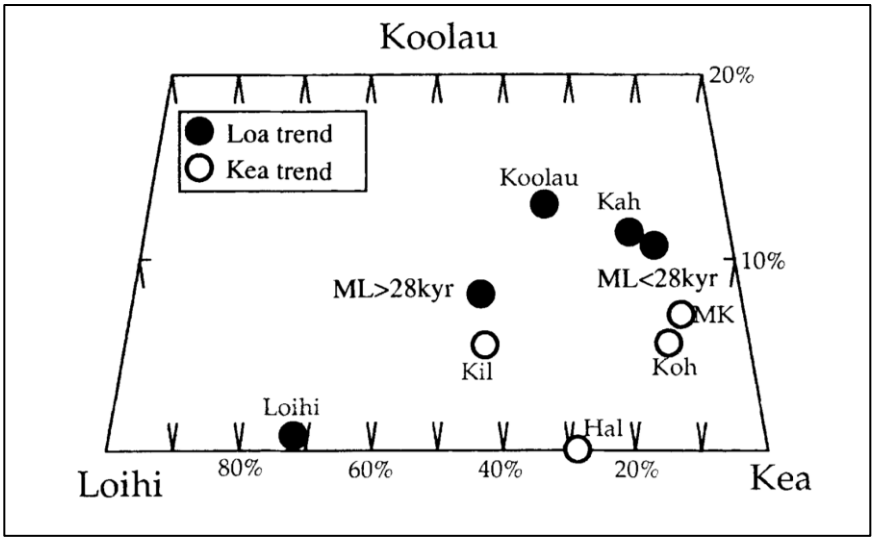

Fig. 1. Plot of where we expect several of the Hawaiian volcanoes fall in terms of the relative contribution of the predicted Koolau, Kea, and Loihi end member components of the Hawaiian plume. Volcanoes that fall on the Kea and Loa trend are plotted with different shades to show that the Kea component contributes heavily to the composition of Kea trend volcanoes. The black circles mark some Loa trend volcanoes (Loihi, Mauna Loa, Koolau, and Kahoolawe). The white circles mark some Kea trend volcanoes (Kilauea, Haleakala, Kohala, and Mauna Kea). From Hauri (1996).

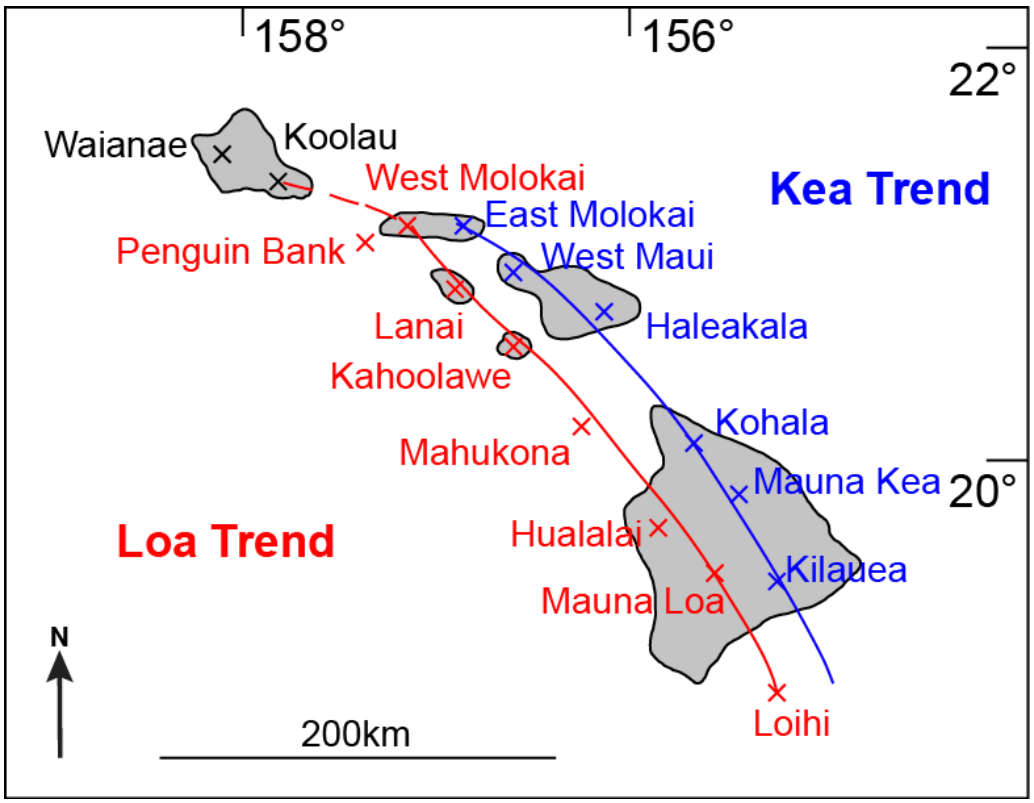

Fig. 2. Map of the Hawaiian Islands showing the volcanoes of the Kea trend, running along the eastern sides of the islands and the volcanoes of the Loa trend along the western sides of the islands. Modified from Frey et al. (2016).

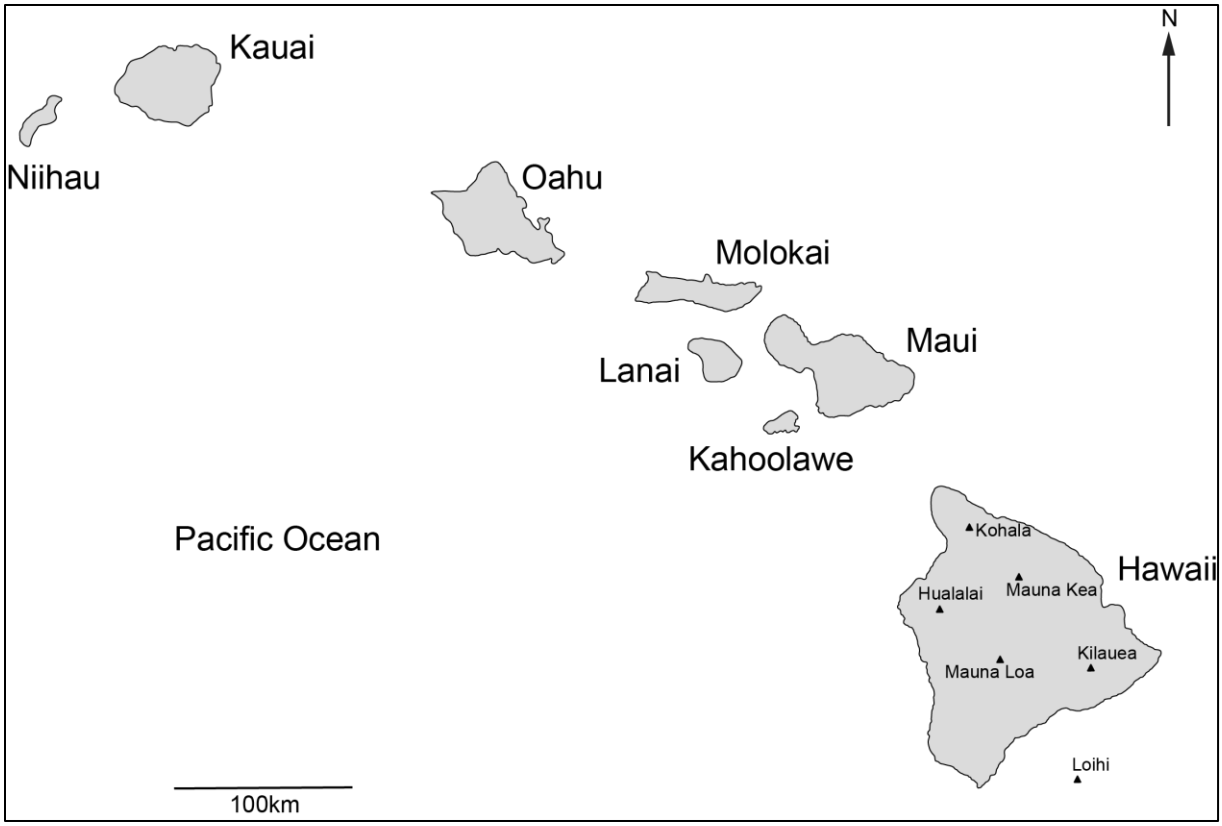

Fig. 3. Map of the Hawaiian Islands. In the southeast corner, Hawaii Island, containing Kohala, Hualalai, Mauna Kea, Mauna Loa, and Kilauea volcanoes, can be seen.

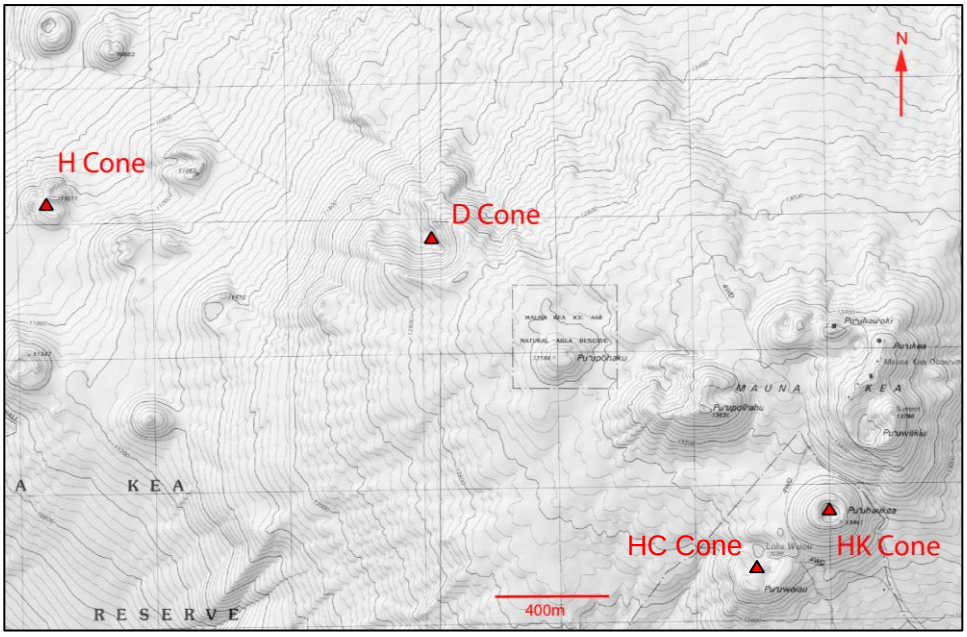

Fig. 4. Map of Mauna Kea volcano, with labeled cones surrounding the central vent from which the samples of this study were collected.

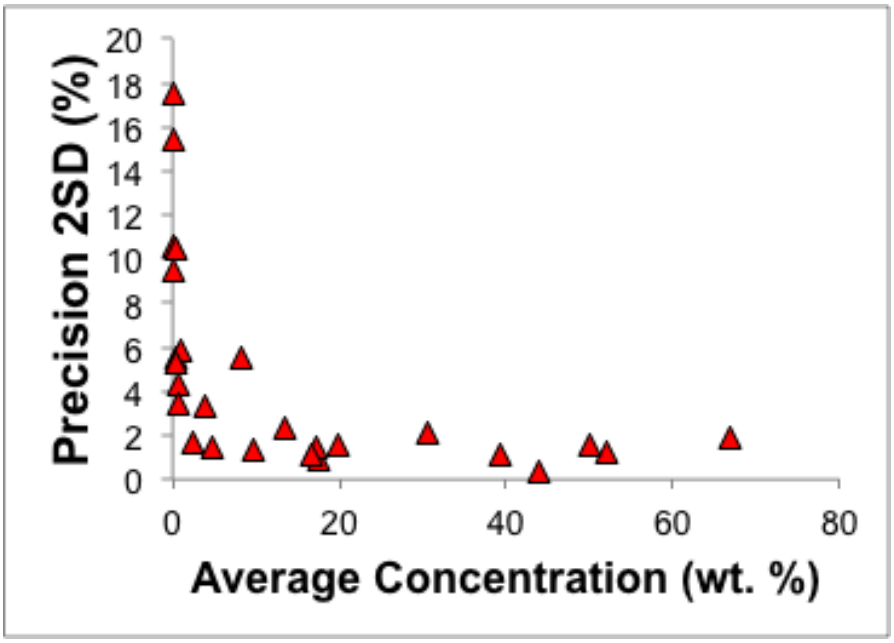

Fig. 5. Plot of precision measured on all major-element secondary standards of this study versus the average concentration of each oxide analyzed. From this graph we can see that the precision becomes increasingly poor as the proportion of oxide relative to the total sample decreases.

a)

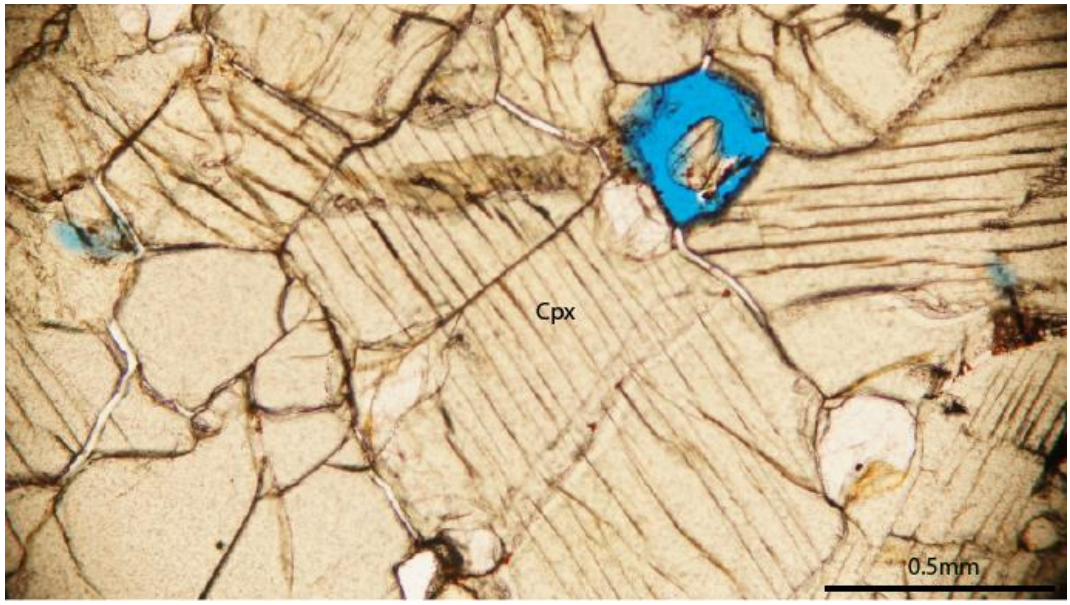

b)

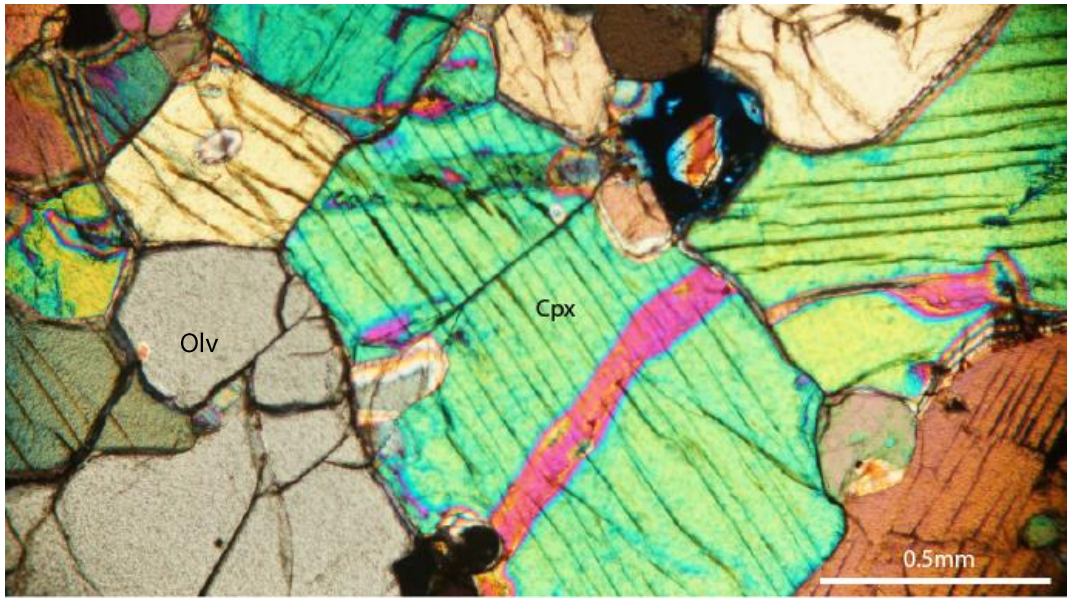

Fig. 6. a) Thin section of HC-25 D in plane polarized light. The phases in this photo are mainly olivines (gray-tan textureless with many fractures) and pyroxenes (gray-tan with lined texture). The center cpx grain has a kink band showing evidence for small-scale differential stress on these samples, perhaps due to the overlying weight of other grains and magma within the magma chamber. b) The same thin section of HC-25 D in cross polarized light. The kink band is much more apparent, standing out as a stark pink against the green color of the rest of the cpx grain.

a)

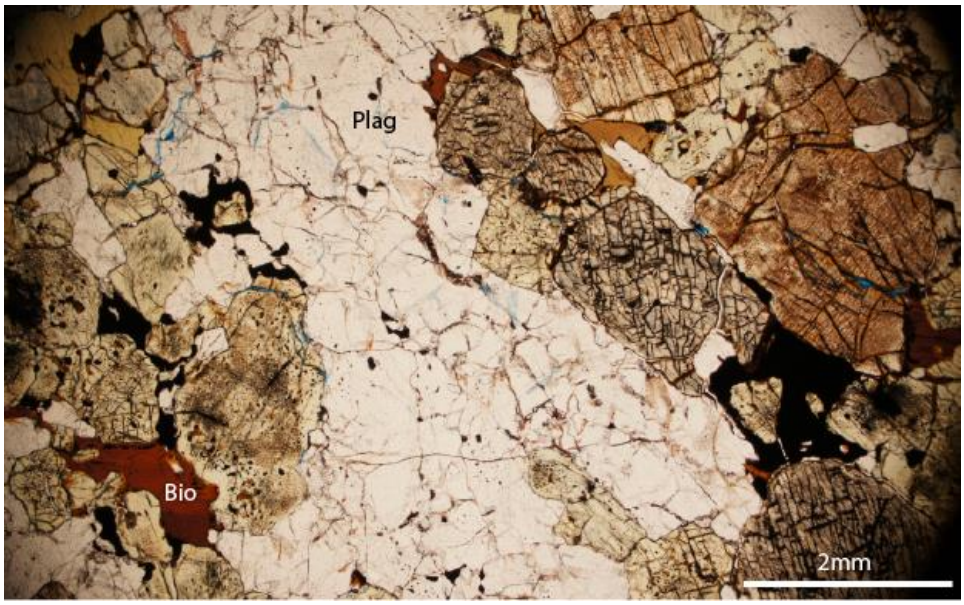

b)

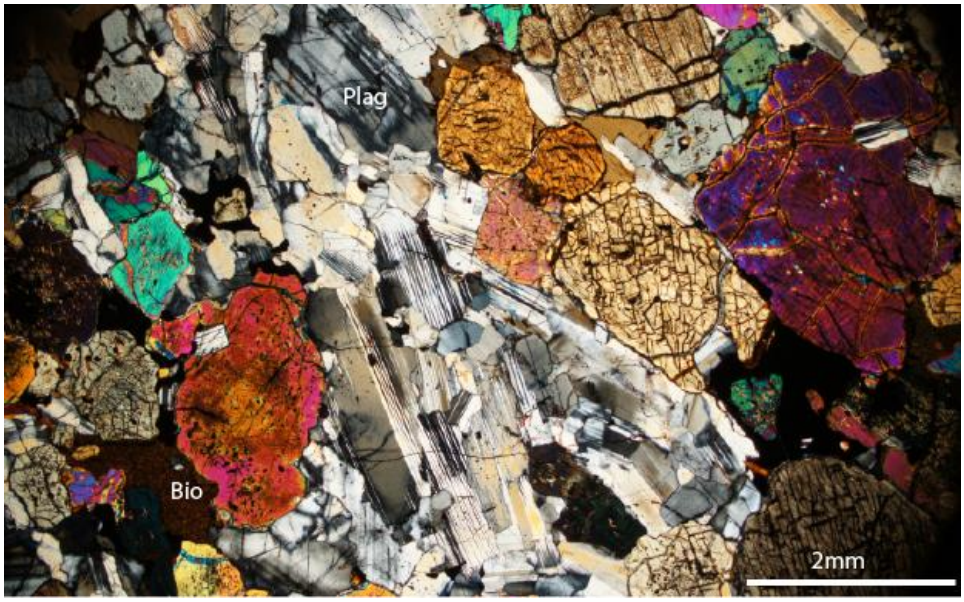

Fig. 7. a) Thin section of sample H-17 in plane polarized light showing an example of possible preferred grain orientation or a recrystallization pattern within the plagioclase grains, which are the colorless minerals through the center of the image. The darker brown minerals filling in the gaps between other grains are biotite, which suggests water was present during crystallization. b) The same thin section of H-17 in cross polarized light. Here, it is clearer that the plagioclase grains, which are black and white, are aligned in a sub-parallel orientation that trends from the top left to the bottom right of the image.

a)

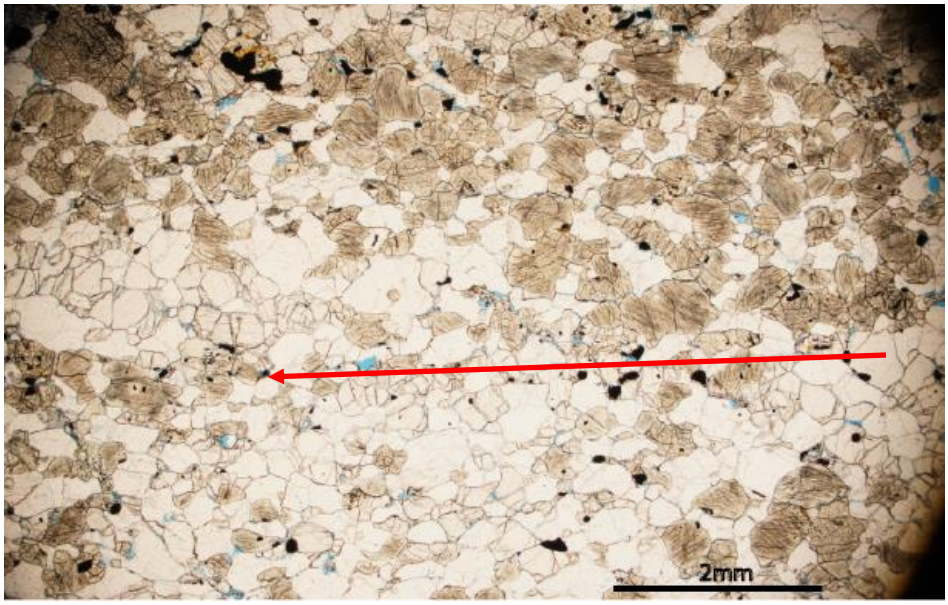

b)

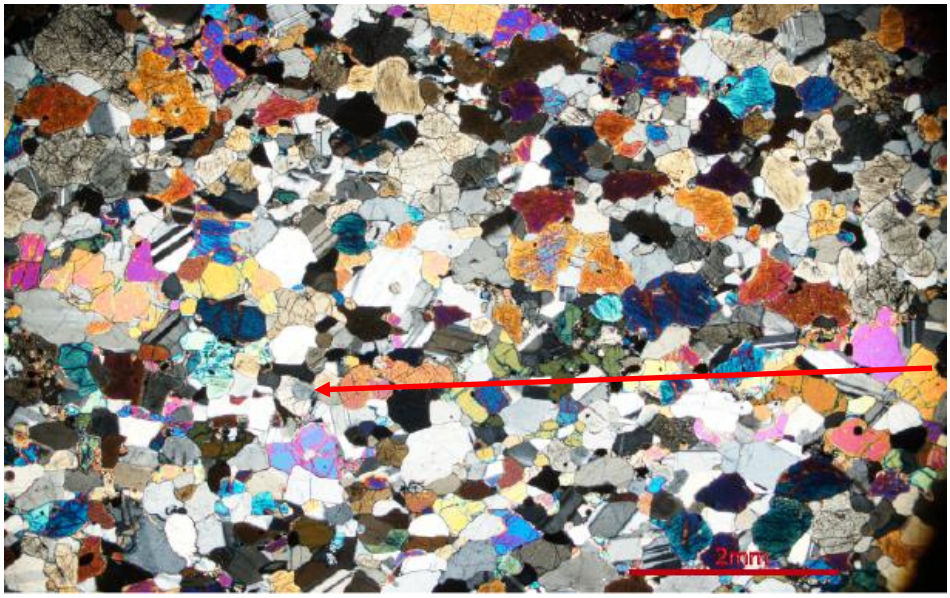

Fig. 8. a) Thin section of HC-10 in plane polarized light. The sample is compositionally banded, with stacked pyroxene-rich and pyroxene-poor horizontal layers. One of these layers is marked by the red arrow. Above the arrow, there is a fairly continuous band of dark gray pyroxene grains. Surrounding this band on the top and bottom is a layer of colorless plagioclase grains. b) The same thin section of HC-10 in cross polarized light. The banding can still be seen, most notably along the red arrow, where a line of dark, colorful grains cuts across the image.

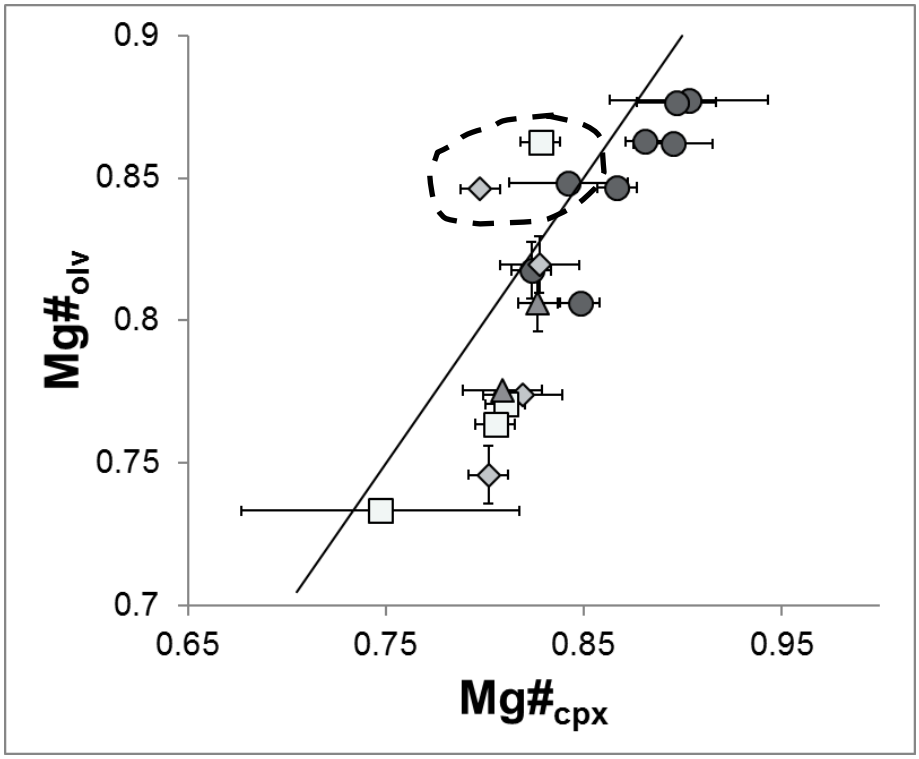

Fig. 9. Plot of $Mg\#_{olv}$ versus $Mg\#_{cpx}$ reflecting good agreement in most samples between olivine and cpx Mg#. We find that the $Mg\#_{olv}$ in each sample is systematically lower than $Mg\#_{cpx}$ by ~0.01-0.05, as is shown by the 1:1 line. The three samples circled by the dashed line show deviations from this trend, which we interpret to be related to the introduction of new melt into the magma chamber. Symbol shape and shade are explained in Table 2.

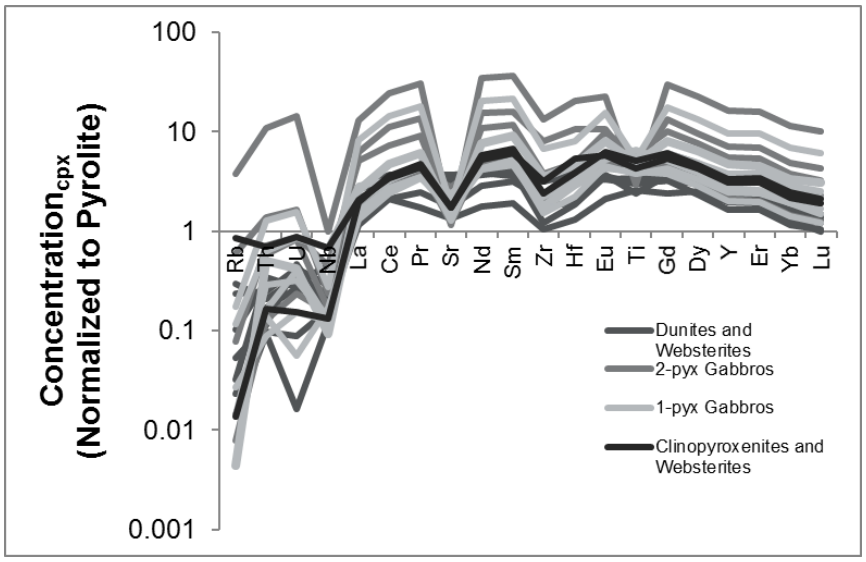

Fig. 10. Spider diagram of normalized trace-element concentrations in cpx mineral separates. The more evolved samples have negative Sr and Eu anomalies associated with the crystallization of plagioclase from the melt. Data are normalized to estimated pyrolite values provided by McDonough and Sun (1995).

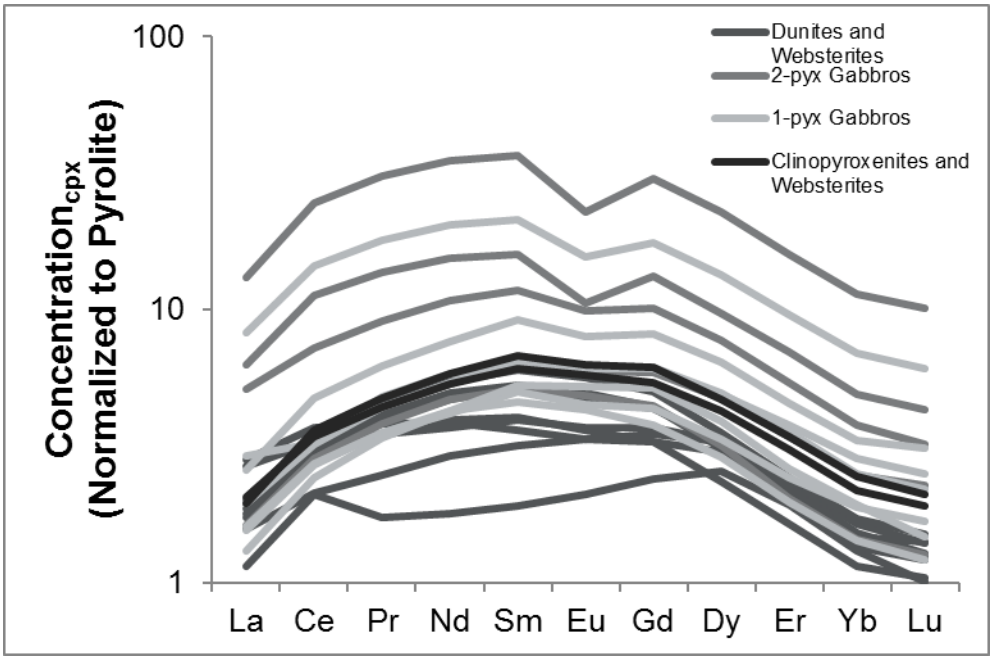

Fig. 11. REE plot showing normalized Rare Earth Element concentrations in cpx mineral separates for each sample. The negative Eu anomalies in the samples crystallizing out from more evolved melts may be a sign of plagioclase formation. Data are normalized to estimated pyrolite values provided by McDonough and Sun (1995).

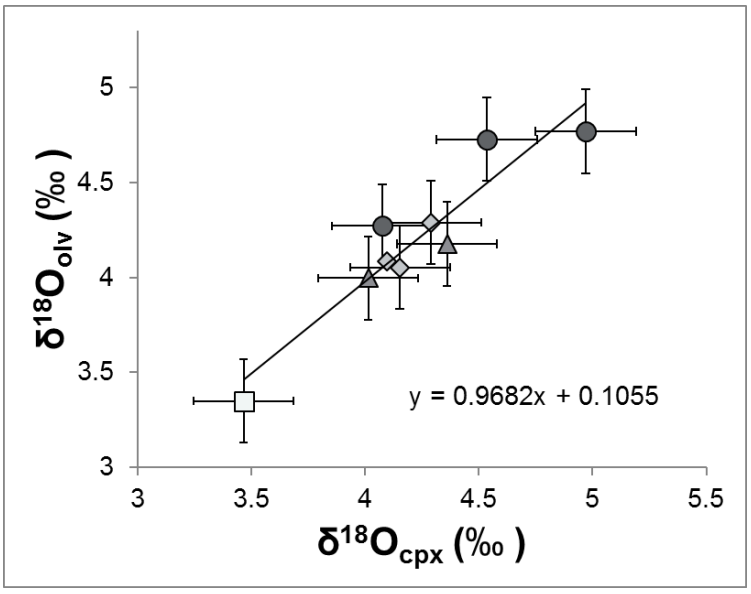

Fig. 12. Plot of $\delta^{18}O$ measured in olivine ($\delta^{18}O_{olv}$) versus $\delta^{18}O$ measured in cpx ($\delta^{18}O_{cpx}$). Using the correlation between $\delta^{18}O_{cpx}$ and $\delta^{18}O_{olv}$, $\delta^{18}O_{olv}$ for HC-26 was extrapolated from the $\delta^{18}O_{cpx}$ value. Measurements of plagioclase O isotopes ($\delta^{18}O_{plag}$) were conducted on three samples, and the values range from +4.4 to 5.1‰ with $\Delta_{plag\text{-}olv}$ = +1.05‰ ± 0.002‰. Using this average standard offset, the expected $\delta^{18}O_{olv}$ for HC-18 CG was calculated.

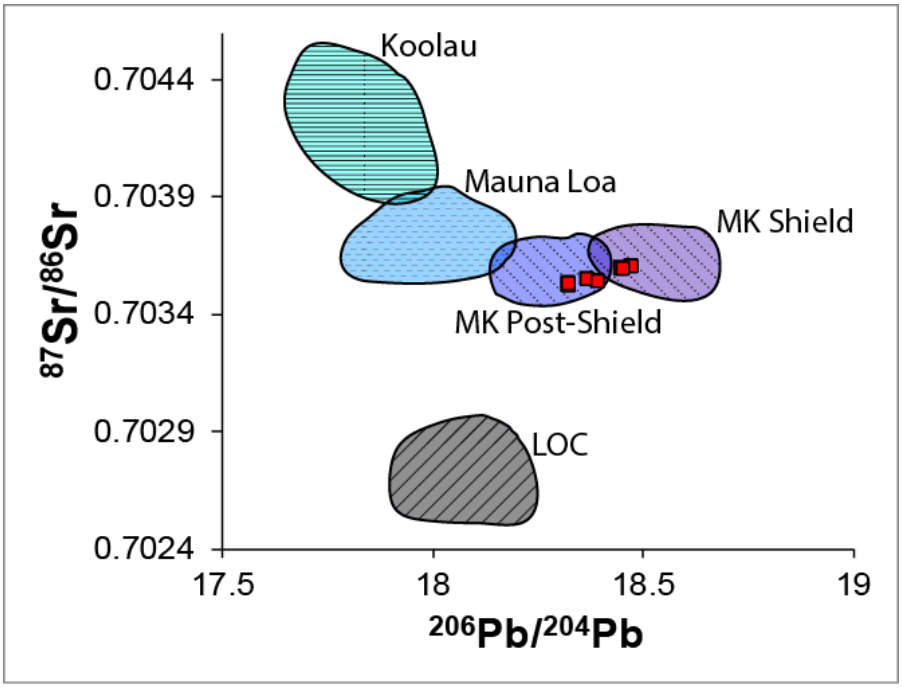

Fig. 13. Plot of Sr versus Pb isotopes for various Hawaiian volcanoes, including Mauna Kea shield and post-shield stage lavas (From Bryce, DePaolo, and Lassiter, 2005), Mauna Loa lavas, and Koolau lavas (from GeoRoc). Measured isotopic compositions of lower oceanic crust (LOC) xenoliths collected from the Kaupulehu flow (from Gao et al., 2016) are plotted in gray as well. Samples from this study are plotted as red squares. The samples fall within the transition zone between Mauna Kea's shield and post-shield stages.

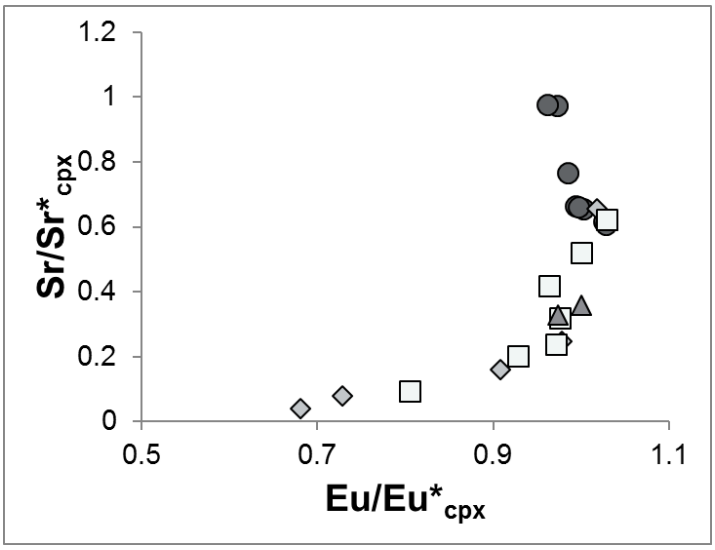

Fig. 14. Plot of Strontium anomaly versus Europium anomaly measured in cpx. Here, we see a sharp drop in Sr/Sr^*_{cpx} relative to Eu/Eu^*_{cpx} associated with an increase in the evolution of the primary magma (as indicated by the lithology). As the melt evolves and changes from crystallizing the dunites in the top right of the diagram to the gabbros in the bottom left, the cpx's forming within the magma chamber are increasingly depleted in both Sr and Eu. This shift marks the crystallization of plagioclase grains in the magma chamber. The curvature of the trend indicates that Sr is more readily accepted by plagioclase early on, while Eu only begins to really enter the phase once the melt has lost a great deal of its Sr. This may be related to oxygen fugacity within the magma chamber, which affects whether the uptake of Eu in plagioclase occurs. This relationship may be evidence that all of these samples crystallized along the same liquid line of descent, deriving from a similar original primary magma. However, the isotopic variability in Figure 18a-d preclude these samples from sharing the same individual source.

a) b)

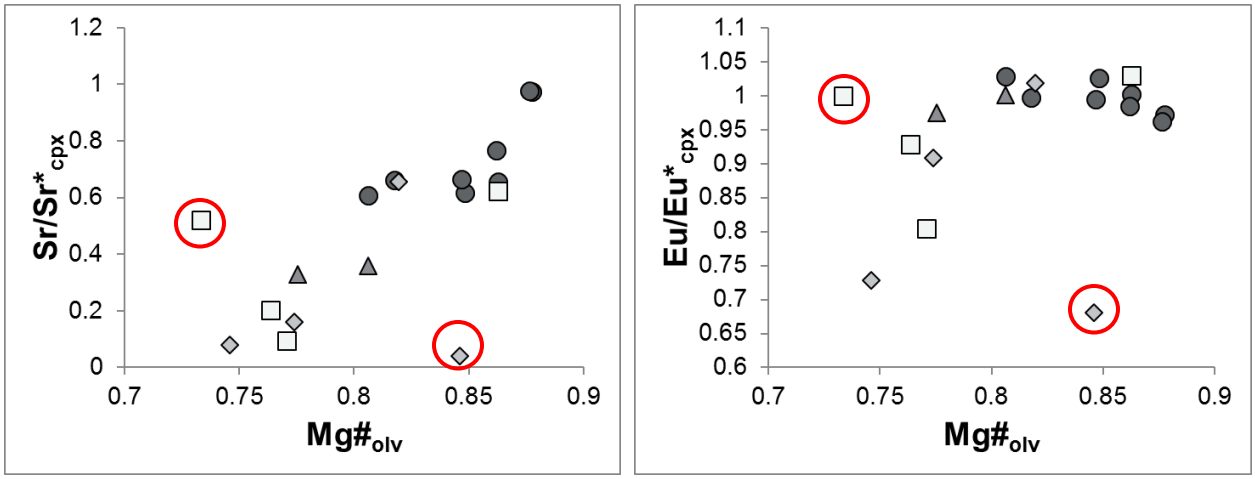

Fig. 15. a) Plot of Sr/Sr^*_{cpx} versus $Mg\#_{olv}$ showing a fair correlation between these values. The evolution of the primary magma is marked by a decrease in Sr/Sr^*_{cpx}, reflecting an overall depletion of Sr within the magma, likely related to the formation of plagioclase. b) Plot of Eu/Eu^*_{cpx} versus $Mg\#_{olv}$ showing a possible nonlinear correlation between these values. Figure _ (Sr/Sr* versus Eu/Eu* above) shows that there is practically no loss of Eu in the melt, relative to Sr until the melt has evolved more substantially, after the dunites (dark gray circles) have crystallized out. It is possible that there is a latency in Eu uptake in plagioclase grains. This plot further confirms this interpretation, as there is hardly a change in Eu/Eu* until after $Mg\#_{olv}$ falls below ~0.80. Two samples, each marked with a red circle in both plots, appear to deviate from the general trend in the data. Each of these two samples was discussed in the *Major-Elements* section for having $Mg\#_{olv}$ unusually higher than $Mg\#_{cpx}$, which may account for why they do not match the trends.

a)

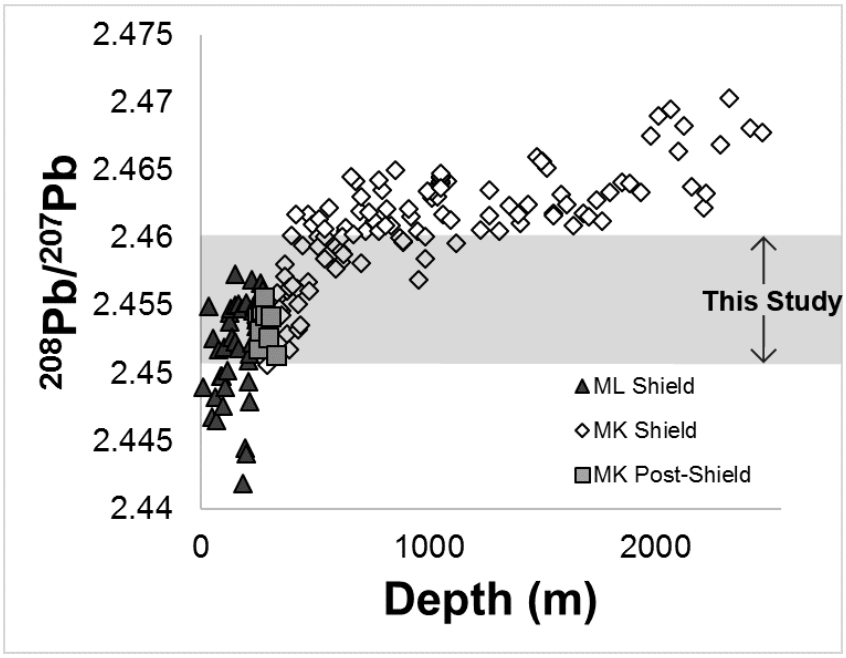

b)

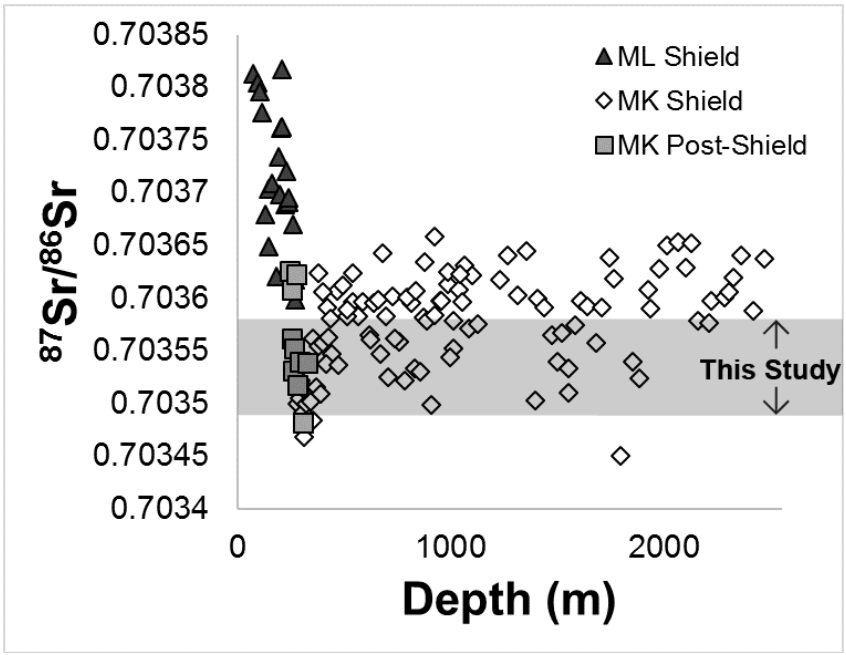

Fig. 16. a)-b) Pb and Sr isotope ratios measured on the HSDP-2 drill core plotted against the depth at which they were collected. The gray shaded region in each plot reflects the Pb and Sr isotope range of the samples collected from this study. Combined, these two charts suggest that the samples of this study crystallized during the late shield to early post-shield stages of Mauna Kea's volcanic history.

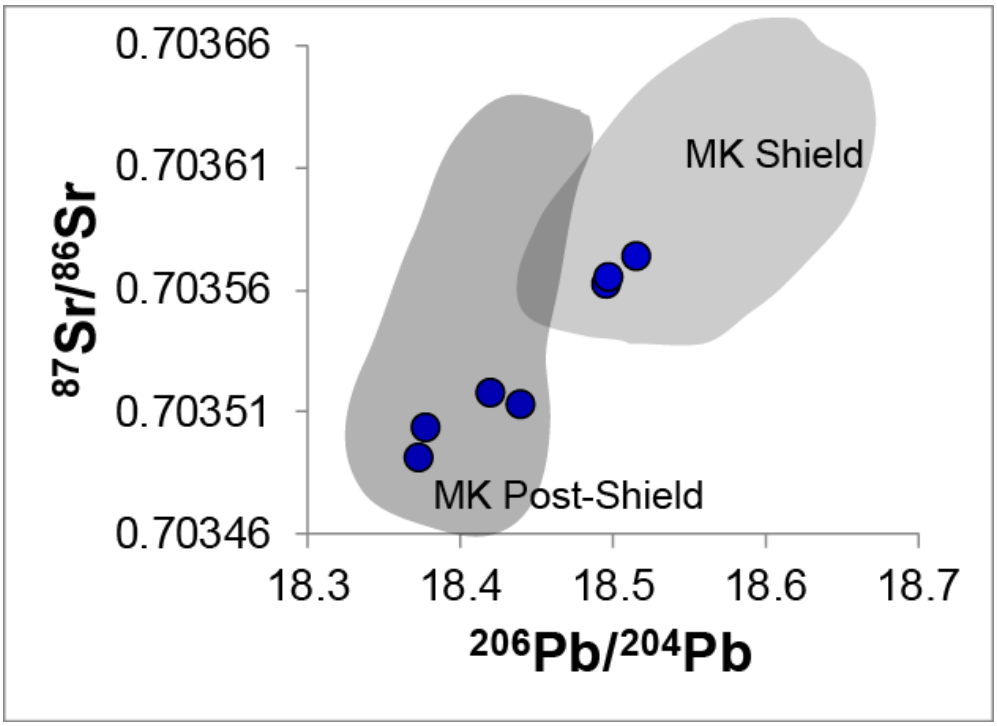

Fig. 17. Plot of $^{87}Sr/^{86}Sr$ versus $^{206}Pb/^{204}Pb$ with regions for Mauna Kea shield and post-shield stages. Data from this study is plotted on top of these regions in blue, showing that most samples likely formed while Mauna Kea was shifting between shield and post-shield stages. Shield and post-shield regions are made from data taken from Bryce, DePaolo, and Lassiter (2005).

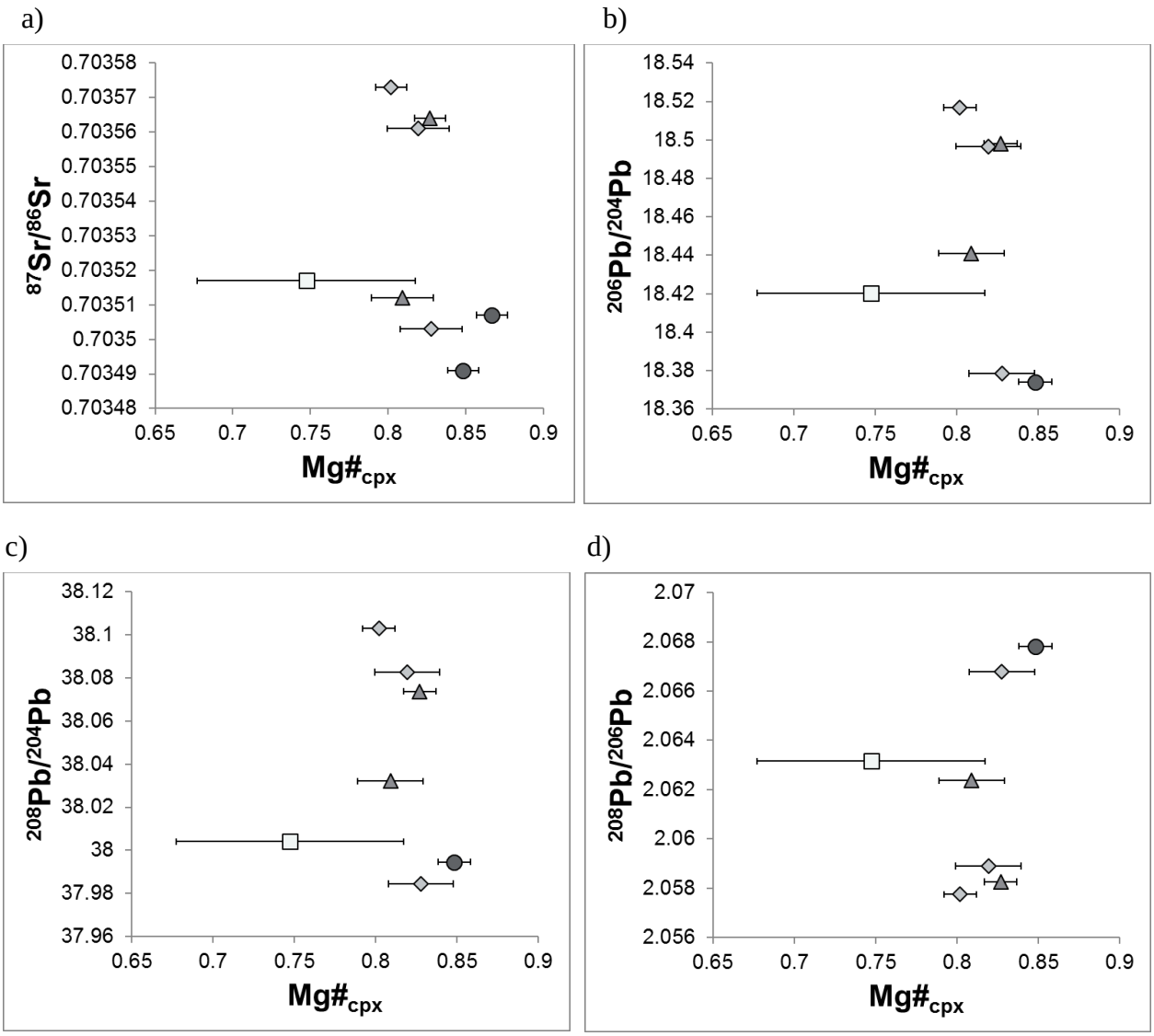

Fig. 18. Plot of Sr and Pb isotopes versus $Mg\#_{cpx}$. There is no clear correlation between Sr or Pb isotopes and $Mg\#_{cpx}$, which suggests that the proposed assimilation process, related to increasing magma evolution, is not associated with Sr and Pb isotope variability. This supports that the assimilant is edifice material, which would possess similar Sr and Pb isotopic ratios to the magma and thus not correlate with any mixing signature.

a)

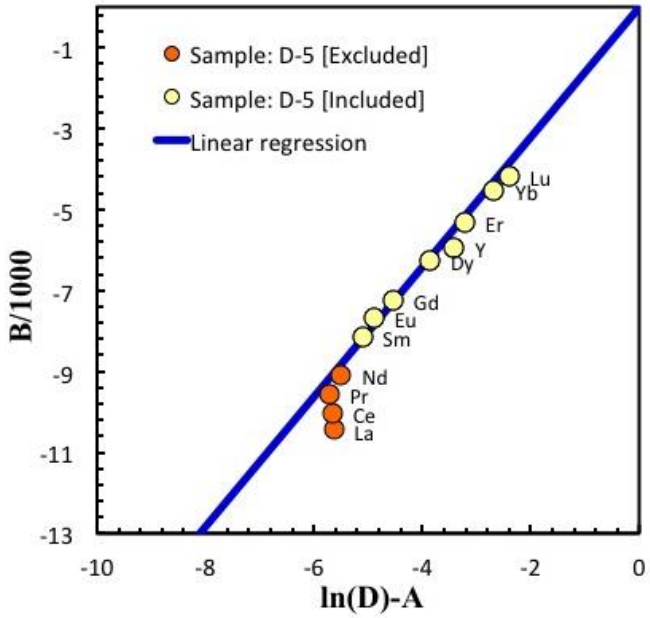
Sample: D-5 [Excluded]
Sample: D-5 [Included]
Linear regression
Lu
Yb
Er
Y
Dy
Gd
Eu
Sm
Nd
Pr
Ce
La
B/1000
ln(D)-A
-1
-3
-5
-7
-9
-11
-13
-10
-8
-6
-4
-2
0

b)

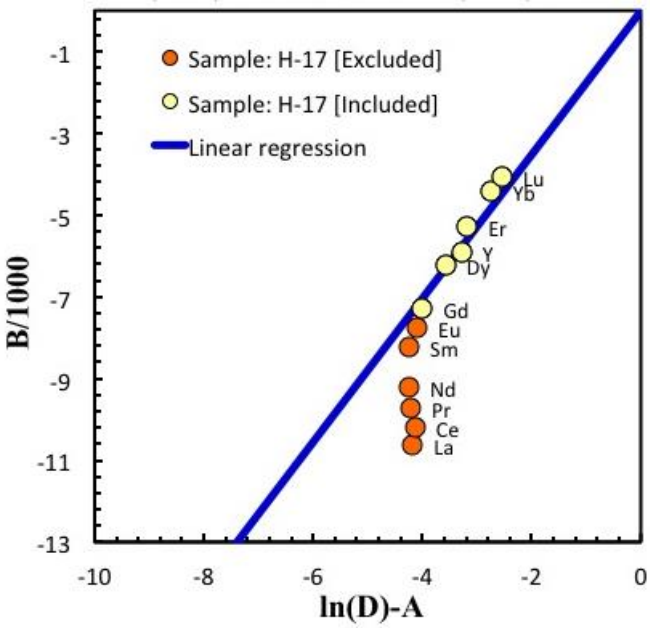
Sample: H-17 [Excluded]
Sample: H-17 [Included]
Linear regression
Lu
Yb
Er
Y
Dy
Gd
Eu
Sm
Nd
Pr
Ce
La
B/1000
ln(D)-A
-1
-3
-5
-7
-9
-11
-13
-10
-8
-6
-4
-2
0

c)

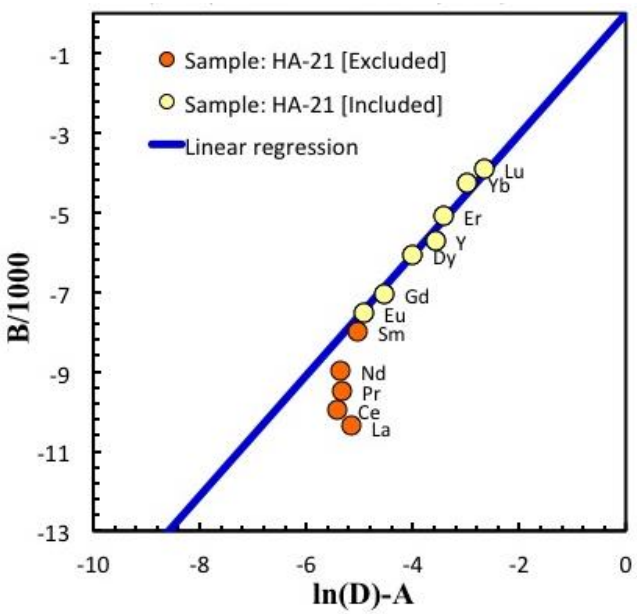
Sample: HA-21 [Excluded]
Sample: HA-21 [Included]
Linear regression
Lu
Yb
Er
Y
Dy
Gd
Eu
Sm
Nd
Pr
Ce
La
B/1000
ln(D)-A
-1
-3
-5
-7
-9
-11
-13
-10
-8
-6
-4
-2
0

d)

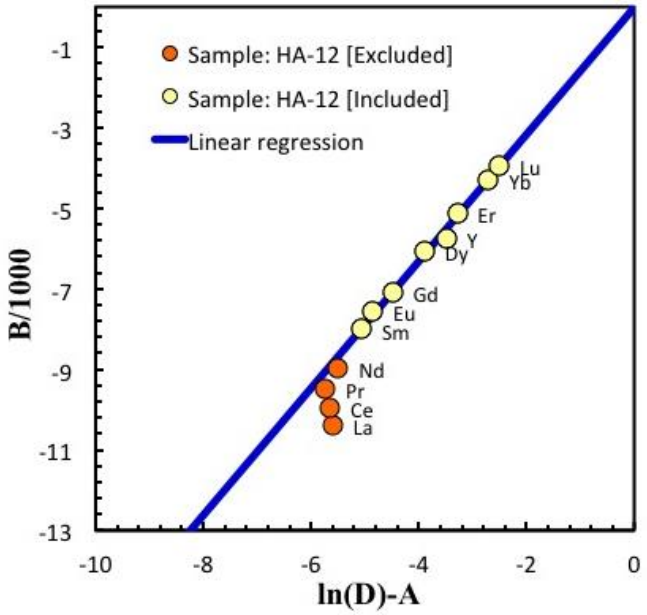
Sample: HA-12 [Excluded]
Sample: HA-12 [Included]
Linear regression
Lu
Yb
Er
Y
Dy
Gd
Eu
Sm
Nd
Pr
Ce
La
B/1000
ln(D)-A
-1
-3
-5
-7
-9
-11
-13
-10
-8
-6
-4
-2
0

e)

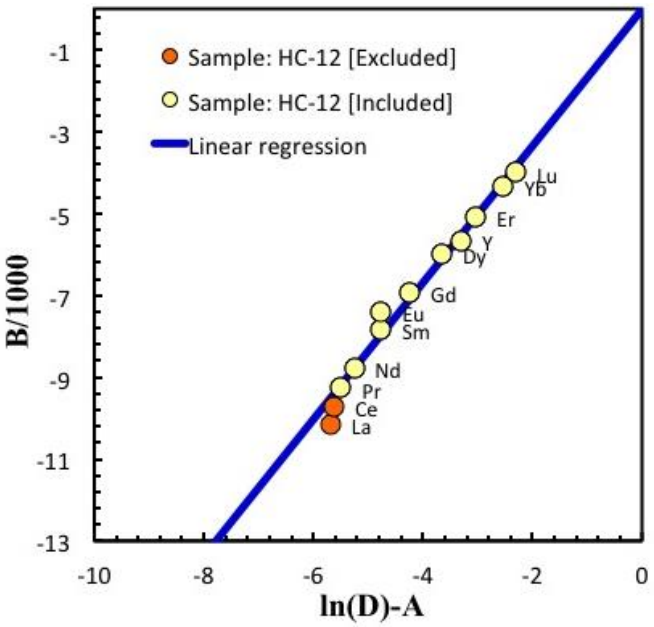

Fig. 19. a)-e) Inversion diagrams showing potential perturbation by secondary processes. We can see that for some samples (e.g., H-17), not all of the REEs in the sample are in equilibrium between opx and cpx. Thus, T_{REE} has been calculated for each sample excluding the elements marked in orange for each plot.

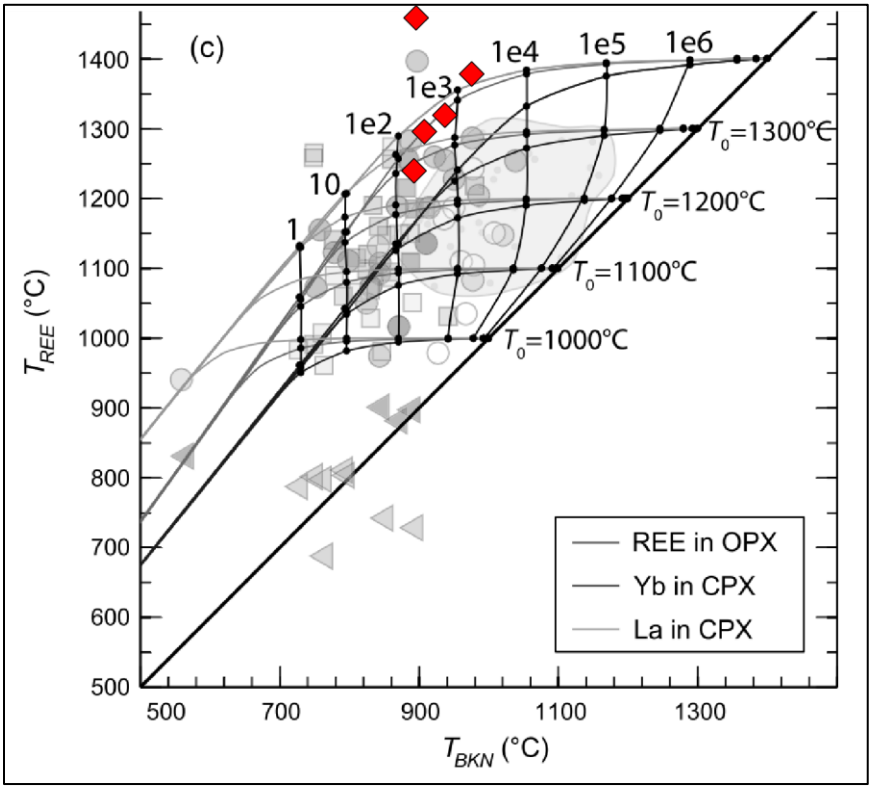

Fig. 20. Plot of T_{REE} versus T_{BKN} modified from Dygert and Liang (2015). The temperatures calculated from rare earth and major-element data measured in cpx and opx are plotted in red. Cooling rates (given in °C per Mya), are shown in black above the curves. The values plotted from this study suggest that these samples cooled at rates between ~10^3 and 10^4°C per Mya.

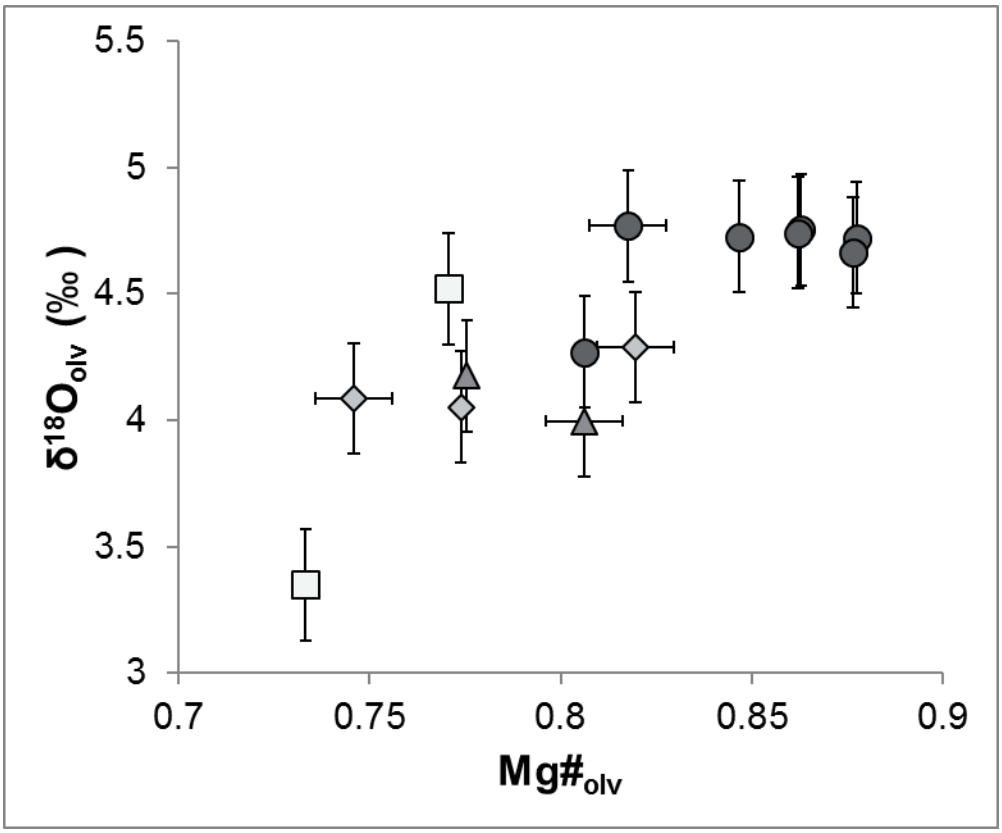

Fig. 21. Oxygen isotopic values measured in olivine versus clinopyroxene Mg#. The strong correlation between $\delta^{18}O_{olv}$ and $Mg\#_{cpx}$ suggests a relationship between oxygen isotopic values and time spent in the magma chamber, which supports the theory of assimilation of hydrothermally altered material. Note that $\delta^{18}O_{olv}$ values for even samples with very high $Mg\#_{cpx}$ are fairly low relative to the expected 5.2‰ mantle value. This suggests that assimilation is not solely responsible for these O-depleted samples.

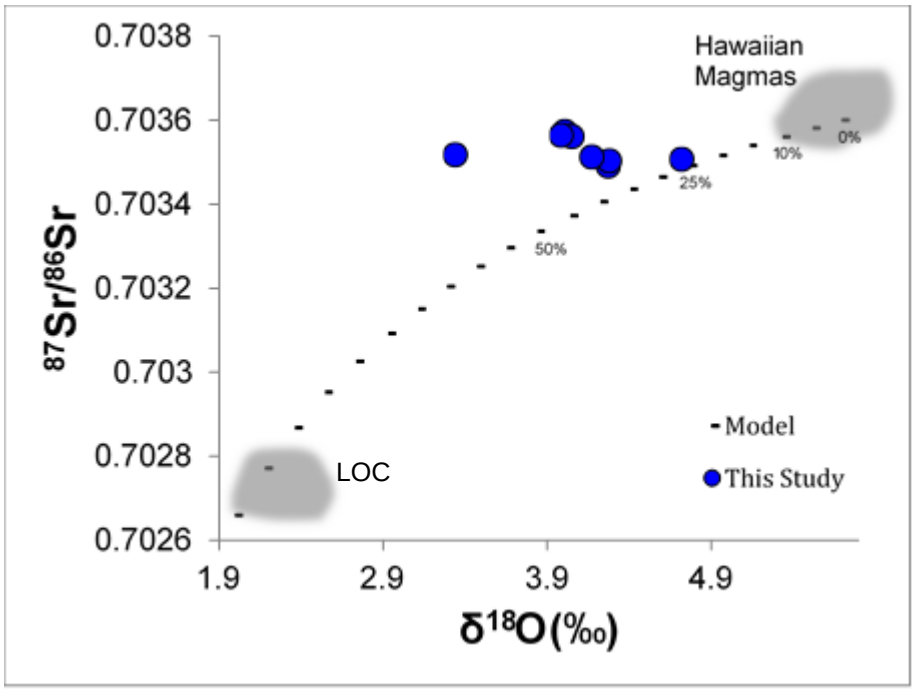

Fig. 22. Binary mixing model between primitive Hawaiian magmas and hydrothermally altered LOC gabbros. Input values are $\delta^{18}O_{magma}$ = +5.7‰ (Lassiter and Hauri, 1998), $\delta^{18}O_{LOC}$ = +2.0‰ (Wang and Eiler, 2008), $^{87}Sr/^{86}Sr_{magma}$ = 0.7036 (Gao et al., 2016), $^{87}Sr/^{86}Sr_{magma}$ = 0.70266 (Lassiter and Hauri, 1998), $[Sr]_{magma}$ = 120ppm (from literature data on Pacific MORB compiled from GeoRoc), and $[Sr]_{LOC}$ = 47ppm (Gao et al., 2016). The data from this study fall off of the mixing curve, indicating that assimilation of LOC cannot explain the observed O variations.

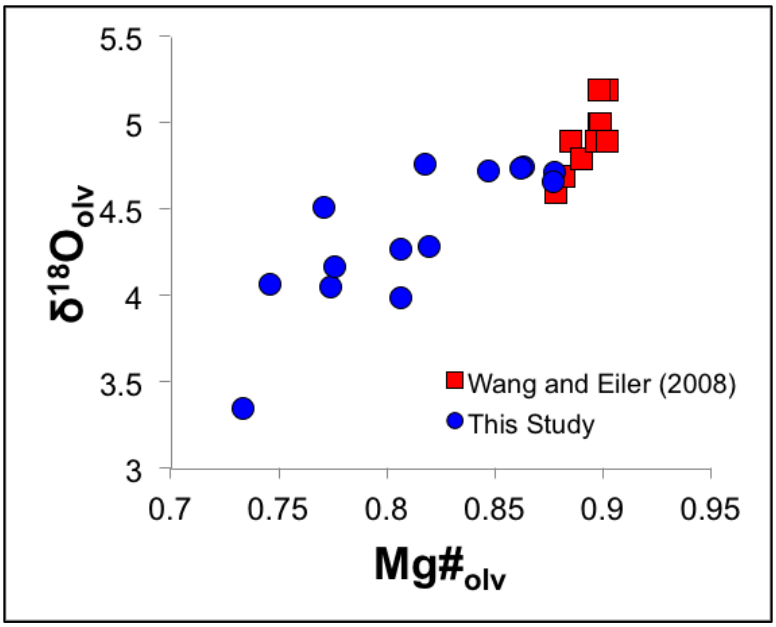

Fig. 23. Plot of $\delta^{18}O_{olv}$ versus $Mg\#_{olv}$. Data from both this study and Wang and Eiler (2008) show that there is a positive correlation between these two values, with the data from this study extending to far lower values for Mg# and $\delta^{18}O$, again supporting the hypothesis that self-assimilation has affected the O isotope values of Mauna Kea lavas.

Tables

Table 1
O isotope compositions of Mauna Kea xenoliths

Sample	n_{olv}	$\delta^{18}O_{olv}$ (‰)	n_{cpx}	$\delta^{18}O_{cpx}$ (‰)	n_{plag}	$\delta^{18}O_{plag}$ (‰)
D Cone	2	4.73 (0.05)	2	4.54 (0.01)	–	–
D-4	2	4.27 (0.15)	2	4.08 (0.24)	–	–
D-5	–	4.09*	2	4.10 (0.09)	–	–
HA-21	2	4.05 (0.05)	2	4.15 (0.01)	1	5.10
HA-6	1	4.75	–	–	–	–
HC-10	2	3.35 (0.01)	2	3.47 (0.03)	1	4.40
HC-12	2	4.00 (0.03)	2	4.01 (0.02)	–	–
HC-18 CG	–	**4.05**	–	–	1	5.10
HC-21	2	4.18 (0.03)	2	4.36 (0.17)	–	–
HC-25D	1	4.77	1	4.97	–	–
HC-26	2	4.52 (0.28)	–	–	–	–
HC-28	1	4.74	–	–	–	–
HC-47	1	4.72	–	–	–	–
HC-61	1	4.66	–	–	–	–
HK-1	2	4.29 (0.02)	2	4.29 (<0.01)	–	–

Values marked with a * have been calculated using the trend between $\delta^{18}O_{olv}$ $\delta^{18}O_{cpx}$. Bolded values were calculated using the average systematic offset (1.05‰) between $\delta^{18}O_{olv}$ and $\delta^{18}O_{plag}$.

Table 2
Xenolith samples listed by lithology

Sample	Lithology	Symbol
D Cone	Wehrlite	Circle
D-4	Wehrlite	Circle
D-5	Olivine gabbronorite (2pyx)	Diamond
H-17	Gabbronorite (2pyx)	Diamond
HA-12	Gabbronorite (2pyx)	Diamond
HA-21	Gabbronorite (2pyx)	Diamond
HA-6	Dunite	Circle
HC-10	Olivine gabbro (1pyx)	Square
HC-12	Websterite	Triangle
HC-18 CG	Gabbro (1pyx)	Square
HC-18 FG	Gabbro (1pyx)	Square
HC-21	Clinopyroxenite	Triangle
HC-25 D	Wehrlite	Circle
HC-25 L	Dunite	Circle
HC-26	Olivine gabbro (1pyx)	Square
HC-28	Dunite	Circle
HC-47	Dunite	Circle
HC-52	Gabbro (1pyx)	Square
HC-61	Dunite	Circle
HC-76	Olivine gabbro (1pyx)	Square
HC-77	Gabbro (1pyx)	Square
HK-1	Olivine gabbronorite (2pyx)	Diamond

Symbol shades are marked by Mg#, with high-Mg# samples (e.g., dunites) being very dark gray and low-Mg# samples (e.g., gabbros) being white.

Table 3
Clinopyroxene major-element compositions (wt. %)

Sample	n	SiO_2	TiO_2	Al_2O_3	Cr_2O_3	FeO	MnO	MgO	CaO	Na_2O	NiO	Total	$Mg\#_{cpx}$
D Cone	8	52.23 (0.71)	0.69 (0.07)	2.60 (0.25)	1.03 (0.07)	4.56 (0.18)	0.12 (0.02)	16.66 (0.30)	21.99 (0.43)	0.36 (0.05)	0.05 (0.01)	100.27 (0.71)	0.87 (0.01)
D-4	16	51.92 (0.93)	0.74 (0.16)	2.81 (0.61)	1.05 (0.08)	4.63 (0.27)	0.11 (0.01)	16.54 (0.46)	22.07 (0.49)	0.36 (0.05)	0.04 (0.01)	100.27 (0.71)	0.85 (0.01)
D-5	4	51.71 (1.12)	0.80 (0.22)	3.04 (0.85)	1.07 (0.08)	4.70 (0.32)	0.11 (0.01)	16.42 (0.56)	22.11 (0.52)	0.34 (0.06)	0.04 (0.01)	100.33 (0.73)	0.80 (0.01)
H-17	11	51.34 (1.26)	0.96 (0.43)	3.27 (0.90)	1.02 (0.14)	4.86 (0.51)	0.11 (0.02)	16.16 (0.71)	22.15 (0.52)	0.37 (0.10)	0.04 (0.02)	100.29 (0.72)	0.80 (0.01)
HA-12	20	51.27 (1.26)	0.98 (0.42)	3.41 (0.92)	1.04 (0.14)	4.95 (0.47)	0.11 (0.02)	16.09 (0.73)	22.16 (0.52)	0.36 (0.10)	0.04 (0.01)	100.41 (0.65)	0.82 (0.01)
HA-21	7	51.07 (1.31)	1.05 (0.43)	3.57 (0.95)	1.05 (0.14)	5.11 (0.41)	0.10 (0.02)	16.08 (0.73)	21.98 (0.57)	0.34 (0.10)	0.04 (0.01)	100.38 (0.66)	0.82 (0.03)
HA-6	4	50.91 (1.30)	1.11 (0.40)	3.83 (0.85)	1.06 (0.14)	5.13 (0.39)	0.11 (0.02)	15.97 (0.68)	22.10 (0.55)	0.34 (0.10)	0.04 (0.01)	100.58 (0.37)	0.88 (0.01)
HC-10	12	50.49 (0.71)	1.21 (0.36)	4.09 (0.60)	1.04 (0.15)	5.23 (0.40)	0.11 (0.02)	15.72 (0.60)	22.25 (0.50)	0.34 (0.10)	0.04 (0.01)	100.50 (0.24)	0.75 (0.07)
HC-12	3	50.35 (0.44)	1.31 (0.29)	4.11 (0.53)	0.97 (0.21)	5.35 (0.36)	0.11 (0.02)	15.56 (0.40)	22.28 (0.48)	0.36 (0.11)	0.04 (0.01)	100.44 (0.32)	0.83 (0.03)
HC-18 CG	11	50.36 (0.44)	1.35 (0.28)	3.98 (0.63)	0.91 (0.23)	5.40 (0.35)	0.12 (0.02)	15.52 (0.41)	22.23 (0.46)	0.39 (0.13)	0.04 (0.01)	100.28 (0.46)	0.79 (0.03)
HC-18 FG	9	50.42 (0.44)	1.41 (0.29)	3.89 (0.60)	0.85 (0.22)	5.47 (0.35)	0.12 (0.02)	15.48 (0.41)	22.20 (0.43)	0.42 (0.14)	0.04 (0.01)	100.3 (0.49)	0.82 (0.03)
HC-21	13	50.39 (0.50)	1.40 (0.28)	3.86 (0.58)	0.85 (0.22)	5.49 (0.36)	0.12 (0.01)	15.53 (0.35)	22.18 (0.43)	0.42 (0.13)	0.04 (0.01)	100.27 (0.49)	0.81 (0.02)
HC-25 D	11	50.26 (0.46)	1.44 (0.23)	3.91 (0.62)	0.84 (0.21)	5.55 (0.32)	0.11 (0.01)	15.47 (0.36)	22.20 (0.44)	0.42 (0.12)	0.05 (0.01)	100.25 (0.49)	0.82 (0.01)
HC-25L	8	50.26 (0.46)	1.48 (0.24)	3.90 (0.61)	0.81 (0.20)	5.59 (0.34)	0.12 (0.01)	15.31 (0.30)	22.35 (0.16)	0.46 (0.12)	0.05 (0.01)	100.31 (0.49)	0.84 (0.03)
HC-26	10	50.11 (0.57)	1.57 (0.21)	3.86 (0.58)	0.76 (0.15)	5.75 (0.19)	0.12 (0.01)	15.25 (0.22)	22.26 (0.25)	0.47 (0.09)	0.04 (0.01)	100.19 (0.52)	0.81 (0.01)
HC-28	2	50.15 (0.58)	1.57 (0.21)	3.84 (0.57)	0.76 (0.16)	5.81 (0.22)	0.12 (0.01)	15.34 (0.28)	22.11 (0.36)	0.47 (0.10)	0.05 (0.01)	100.23 (0.57)	0.90 (0.02)
HC-47	2	53.60 (2.43)	0.58 (0.01)	2.24 (0.11)	1.12 (<0.01)	3.18 (0.09)	0.05 (0.01)	16.62 (0.71)	23.42 (0.94)	0.43 (0.02)	0.04 (0.01)	101.28 (2.03)	0.90 (0.04)
HC-52	5	50.92 (0.67)	0.88 (0.05)	3.94 (0.25)	0.88 (0.10)	5.80 (0.19)	0.12 (0.02)	15.80 (0.13)	21.67 (0.27)	0.29 (0.06)	0.04 (0.01)	100.35 (0.85)	0.83 (0.01)
HC-61	5	53.20 (0.55)	0.55 (0.03)	2.41 (0.14)	1.17 (0.04)	3.47 (0.15)	0.07 (0.02)	16.76 (0.22)	23.06 (0.48)	0.57 (0.03)	0.06 (0.02)	101.32 (0.65)	0.90 (0.01)
HC-76	6	51.08 (1.47)	1.12 (0.33)	3.00 (0.42)	0.44 (0.20)	8.16 (2.06)	0.19 (0.03)	16.57 (1.99)	19.81 (3.66)	0.36 (0.07)	0.05 (0.01)	100.78 (0.86)	0.81 (0.01)
HC-77	8	51.89 (0.77)	0.92 (0.19)	2.68 (0.36)	0.53 (0.13)	6.72 (1.07)	0.16 (0.02)	16.41 (1.11)	21.05 (1.93)	0.36 (0.04)	0.03 (0.01)	100.74 (0.64)	0.82 (0.02)
HK-1	8	50.24 (0.70)	1.09 (0.15)	4.24 (0.38)	0.80 (0.22)	5.76 (0.33)	0.12 (0.01)	15.49 (0.23)	22.11 (0.15)	0.31 (0.03)	0.05 (0.01)	100.20 (0.66)	0.83 (0.02)

Table 4
Orthopyroxene major-element compositions (wt. %)

Sample	n	SiO_2	TiO_2	Al_2O_3	Cr_2O_3	FeO	MnO	MgO	CaO	Na_2O	NiO	Total
D-5	9	54.72	0.39	1.30	0.11	15.12	0.31	28.29	1.10	0.01	0.07	101.43
		(0.48)	(0.04)	(0.12)	(0.02)	(0.16)	(0.02)	(0.17)	(0.28)	(0.01)	(0.03)	(0.51)
H-17	4	54.91	0.50	1.44	0.19	13.70	0.28	28.57	1.47	0.02	0.06	101.16
		(0.53)	(0.02)	(0.21)	(0.03)	(0.05)	(0.02)	(0.41)	(0.24)	(<0.01)	(0.01)	(0.78)
HA-12	10	55.13	0.24	1.21	0.07	15.10	0.34	28.33	1.02	0.02	0.08	101.52
		(0.95)	(0.04)	(0.14)	(0.05)	(0.27)	(0.01)	(0.31)	(0.50)	(0.02)	(0.03)	(0.85)
HA-21	7	55.31	0.62	1.68	0.15	12.23	0.25	29.56	1.61	0.03	0.08	101.50
		(0.52)	(0.11)	(0.22)	(0.03)	(0.28)	(0.01)	(0.27)	(0.5)	(0.01)	(0.01)	(0.63)
HC-12	4	55.10	0.43	1.39	0.17	13.87	0.29	28.83	1.42	0.02	0.08	101.60
		(0.13)	(0.15)	(0.16)	(0.04)	(0.28)	(0.02)	(0.45)	(0.82)	(0.02)	(0.02)	(0.15)

Table 5
Plagioclase major-element compositions (wt. %)

Sample	n	SiO_2	Al_2O_3	FeO	MgO	CaO	Na_2O	K_2O	Total
D-4	5	50.27	31.20	0.33	0.06	14.28	3.35	0.18	99.68
		(1.65)	(1.11)	(0.15)	(0.08)	(1.20)	(0.67)	(0.11)	(0.62)
D-5	5	53.08	29.54	0.28	0.03	12.35	4.47	0.26	100.02
		(1.07)	(1.03)	(0.01)	(0.01)	(1.13)	(0.53)	(0.05)	(0.61)
H-17	4	55.63	27.82	0.34	0.02	10.27	5.53	0.42	100.02
		(1.47)	(1.27)	(0.02)	(0.01)	(1.36)	(0.63)	(0.18)	(0.45)
HA-12	5	50.89	31.05	0.27	0.03	14.07	3.59	0.13	100.04
		(0.41)	(0.29)	(0.01)	(0.01)	(0.25)	(0.14)	(0.01)	(0.42)
HA-21	6	49.62	31.35	0.29	0.04	14.68	3.09	0.12	99.19
		(0.52)	(0.64)	(0.02)	(0.01)	(0.52)	(0.24)	(0.02)	(0.71)
HC-10	5	50.59	30.59	0.29	0.02	13.87	3.62	0.10	99.08
		(0.27)	(0.34)	(0.04)	(0.01)	(0.24)	(0.16)	(0.02)	(0.46)
HC-12	4	49.88	31.20	0.25	0.04	14.53	3.13	0.14	99.16
		(2.42)	(1.62)	(0.01)	(0.01)	(1.85)	(1.05)	(0.06)	(0.76)
HC-18	5	51.00	30.84	0.35	0.03	13.87	3.61	0.13	99.83
CG		(0.63)	(0.26)	(0.02)	(0.01)	(0.35)	(0.16)	(0.01)	(0.24)
HC-18	4	51.00	30.84	0.35	0.03	13.87	3.61	0.13	99.83
FG		(0.63)	(0.26)	(0.02)	(0.01)	(0.35)	(0.16)	(0.01)	(0.24)
HC-21	5	51.73	29.90	0.28	0.04	12.95	4.11	0.20	99.22
		(0.55)	(0.19)	(0.02)	(0.01)	(0.24)	(0.18)	(0.02)	(0.42)
HC-26	5	52.74	29.48	0.25	0.04	12.23	4.44	0.15	99.33
		(0.33)	(0.14)	(0.01)	(0.01)	(0.21)	(0.12)	(0.02)	(0.31)
HC-52	5	50.85	30.52	0.31	0.05	13.67	3.59	0.26	99.25
		(0.60)	(0.46)	(0.02)	(0.01)	(0.56)	(0.30)	(0.08)	(0.61)
HC-76	4	52.39	29.97	0.30	0.03	12.85	4.2	0.19	99.93
		(0.14)	(0.08)	(0.02)	(0.01)	(0.03)	(0.05)	(0.01)	(0.25)
HC-77	7	52.32	30.03	0.29	0.05	12.86	4.12	0.21	99.87
		(0.32)	(0.36)	(0.03)	(0.01)	(0.29)	(0.13)	(0.02)	(0.61)
HK-1	4	46.75	33.51	0.27	0.02	16.97	1.84	0.07	99.44
		(0.12)	(0.24)	(0.03)	(0.01)	(0.08)	(0.03)	(0.01)	(0.21)

Table 6
Olivine major-element compositions (wt. %)

Sample	n	SiO_2	Al_2O_3	FeO	MnO	MgO	CaO	NiO	Total	$Mg\#_{olv}$
D Cone	4	39.35 (0.21)	0.02 (0.01)	14.58 (0.08)	0.17 (0.02)	45.16 (0.11)	0.09 (0.01)	0.29 (0.03)	99.65 (0.17)	0.85 (<0.01)
D-4	5	38.60 (0.27)	0.02 (0.01)	18.11 (0.13)	0.22 (0.02)	42.28 (0.10)	0.06 (0.02)	0.23 (0.02)	99.53 (0.30)	0.81 (<0.01)
D-5	5	37.59 (0.81)	0.01 (0.02)	23.02 (0.75)	0.26 (0.03)	37.92 (0.71)	0.04 (<0.01)	0.31 (0.02)	99.15 (2.19)	0.75 (0.01)
H-17	5	39.66 (0.44)	0.01 (0.01)	14.66 (0.15)	0.17 (0.02)	45.20 (0.22)	0.09 (<0.01)	0.30 (0.02)	100.08 (0.64)	0.85 (<0.01)
HA-21	6	38.39 (0.25)	0.01 (0.01)	20.98 (0.22)	0.25 (0.02)	40.31 (0.21)	0.04 (0.01)	0.26 (0.02)	100.24 (0.38)	0.77 (<0.01)
HA-6	5	39.85 (0.32)	0.02 (0.01)	13.17 (0.11)	0.14 (0.02)	46.47 (0.14)	0.18 (0.01)	0.34 (0.03)	100.17 (0.42)	0.86 (<0.01)
HC-10	6	39.35 (0.21)	0.02 (0.01)	14.58 (0.08)	0.17 (0.02)	45.16 (0.11)	0.09 (0.01)	0.29 (0.03)	99.65 (0.17)	0.73 (<0.01)
HC-12	4	39.19 (0.07)	0.02 (0.02)	18.14 (0.58)	0.19 (0.01)	42.30 (0.41)	0.05 (0.01)	0.28 (0.02)	100.15 (0.16)	0.81 (0.01)
HC-21	4	38.38 (0.12)	0.01 (0.01)	20.94 (0.08)	0.23 (0.02)	40.58 (0.07)	0.06 (0.01)	0.24 (0.01)	100.42 (0.20)	0.78 (<0.01)
HC-25D	8	38.94 (0.30)	0.02 (0.01)	17.20 (0.68)	0.17 (0.02)	43.26 (0.19)	0.09 (0.01)	0.22 (0.02)	99.9 (0.87)	0.82 (<0.01)
HC-25L	6	39.4 (0.37)	0.02 (0.01)	14.57 (0.27)	0.15 (0.02)	45.75 (0.12)	0.09 (0.01)	0.27 (0.03)	100.25 (0.25)	0.85 (<0.01)
HC-26	5	38.28 (0.26)	0.02 (0.01)	21.27 (0.18)	0.25 (0.02)	40.10 (0.13)	0.06 (0.01)	0.28 (0.02)	100.26 (0.30)	0.77 (<0.01)
HC-28	6	39.79 (0.32)	0.03 (0.01)	13.25 (0.12)	0.15 (0.02)	46.45 (0.37)	0.20 (0.01)	0.31 (0.01)	100.17 (0.77)	0.86 (<0.01)
HC-47	5	40.21 (0.19)	0.02 (0.01)	11.90 (0.12)	0.12 (0.02)	47.78 (0.11)	0.19 (0.01)	0.38 (0.02)	100.59 (0.40)	0.88 (<0.01)
HC-52	2	39.96 (0.13)	0.01 (0.01)	13.27 (0.19)	0.14 (0.01)	46.75 (0.06)	0.20 (<0.01)	0.32 (0.03)	100.64 (0.12)	0.86 (<0.01)
HC-61	6	40.31 (0.14)	0.02 (0.01)	11.97 (0.18)	0.13 (0.02)	47.67 (0.12)	0.19 (0.01)	0.4 (0.01)	100.67 (0.34)	0.88 (<0.01)
HC-76	4	38.31 (0.07)	0.01 (0.01)	21.87 (0.03)	0.23 (0.03)	39.65 (0.27)	0.06 (0.01)	0.24 (0.02)	100.36 (0.33)	0.76 (<0.01)
HK-1	6	39.27 (0.27)	0.01 (0.01)	17.18 (0.65)	0.19 (0.01)	43.77 (0.61)	0.06 (<0.01)	0.27 (0.02)	100.73 (0.40)	0.82 (0.01)

Table 7
Spinel major-element compositions (wt. %)

Sample	n	SiO_2	TiO_2	Al_2O_3	Cr_2O_3	FeO	MnO	MgO	Total
HA-6	4	0.03 (0.03)	2.37 (0.26)	14.79 (0.43)	38.41 (0.73)	32.38 (0.7)	0.19 (0.02)	10.45 (0.18)	98.62 (0.78)
HC-25L	6	0.04 (0.02)	2.2 (0.08)	18.38 (0.54)	33.64 (0.5)	34.06 (0.2)	0.18 (0.02)	10.15 (0.2)	98.65 (0.29)
HC-28	4	0.03 (0.03)	2.12 (0.09)	13.17 (0.11)	41.83 (0.41)	30.77 (0.23)	0.19 (0.02)	9.86 (0.05)	97.98 (0.29)
HC-47	7	0.03 (0.03)	1.98 (0.09)	14.59 (0.55)	42.04 (1.17)	28.32 (0.25)	0.18 (0.01)	11 (0.17)	98.13 (0.78)
HC-61	7	0.04 (0.02)	1.88 (0.22)	13.88 (0.07)	43.81 (0.43)	27.96 (0.43)	0.17 (0.02)	10.91 (0.11)	98.65 (0.69)

Table 8
Clinopyroxene trace-element compositions (ppm)

Sample	Rb	Th	U	Nb	La	Ce	Pr	Sr	Nd	Sm
D Cone	0.142	0.020	0.009	0.19	1.21	4.94	0.88	48.93	4.91	1.64
D-4	0.009	0.007	−	0.08	1.16	5.15	1.04	54.47	6.19	2.13
D-5	0.356	0.111	0.033	0.16	4.05	18.96	3.50	22.85	19.22	6.45
H-17	2.296	0.861	0.289	0.66	8.52	40.94	7.84	25.70	43.94	14.95
HA-12	−	0.047	0.017	0.11	1.26	5.61	1.12	24.05	6.70	2.59
HA-21	0.047	0.057	0.018	0.30	3.31	12.14	2.31	31.50	13.54	4.77
HA-6	0.178	0.017	0.007	0.14	1.02	3.57	0.63	34.93	3.62	1.29
HC-10	0.008	0.023	0.007	0.09	0.85	4.04	0.86	39.20	5.31	2.15
HC-12	0.510	0.055	0.018	0.45	1.33	5.74	1.11	34.30	6.64	2.47
HC-18 CG	−	0.013	0.008	0.08	1.27	5.39	1.11	30.90	6.74	2.69
HC-18 FG	0.070	0.050	0.017	0.45	1.88	5.46	1.22	25.30	7.30	2.60
HC-21	0.008	0.013	0.003	0.09	1.26	6.03	1.20	34.50	7.32	2.76
HC-25D	0.014	0.008	0.002	0.11	1.12	4.97	0.99	56.35	5.85	2.11
HC-25L	−	0.014	0.005	0.14	1.31	5.78	1.14	60.90	6.85	2.45
HC-26	0.104	0.102	0.032	0.18	5.34	24.31	4.57	35.98	25.47	8.66
HC-28	0.032	0.009	0.009	0.11	0.74	3.51	0.44	26.86	2.23	0.78
HC-47	0.062	0.026	0.006	0.30	1.82	6.16	0.96	74.25	4.83	1.46
HC-52	−	0.011	0.001	0.11	1.04	4.55	0.90	48.08	5.29	1.86
HC-61	0.020	0.027	0.006	0.16	1.73	5.51	0.89	70.10	4.64	1.60
HC-76	0.003	0.040	0.009	0.06	1.67	7.95	1.57	27.56	9.51	3.71
HC-77	0.016	0.007	0.003	0.08	1.00	4.52	0.90	31.85	5.20	2.03
HK-1	0.005	0.010	0.005	0.10	1.05	4.80	0.97	55.17	5.84	2.08

Table 8 Continued

Clinopyroxene trace-element compositions (ppm)

Sample	Zr	Hf	Eu	Ti	Gd	Dy	Y	Er	Yb	Lu
D Cone	12.73	0.53	0.56	3633.00	1.78	1.59	7.17	0.72	0.51	0.071
D-4	20.96	1.01	0.76	5853.33	2.38	2.10	9.19	0.92	0.66	0.084
D-5	84.77	2.99	1.63	5276.67	7.20	6.55	30.60	3.07	2.15	0.291
H-17	141.6	5.85	3.50	3524.40	16.47	15.37	70.76	6.96	5.02	0.682
HA-12	23.73	0.93	0.92	5010.00	3.19	3.21	15.05	1.50	1.10	0.153
HA-21	39.47	1.38	1.53	7165.00	5.52	5.19	24.02	2.35	1.67	0.217
HA-6	21.98	0.93	0.52	4160.00	1.90	2.21	10.57	1.02	0.72	0.094
HC-10	19.29	0.88	0.80	7890.00	2.80	2.62	11.71	1.14	0.85	0.099
HC-12	33.40	1.52	0.89	5170.00	2.95	2.86	13.32	1.34	0.96	0.129
HC-18 CG	23.40	0.91	0.96	6020.00	3.33	3.32	15.01	1.57	1.10	0.148
HC-18 FG	24.4	0.92	0.93	6250.00	3.31	3.30	16.22	1.65	1.25	0.169
HC-21	25.06	1.11	0.97	6215.00	3.34	3.15	14.34	1.50	1.08	0.143
HC-25D	19.70	0.92	0.73	5365.00	2.37	2.21	9.44	0.96	0.65	0.096
HC-25L	24.44	1.18	0.87	6053.33	2.73	2.40	10.84	1.06	0.76	0.102
HC-26	71.42	2.25	2.40	6280.00	9.59	9.04	40.93	4.21	3.06	0.410
HC-28	10.87	0.37	0.32	3140.00	1.30	1.72	8.49	0.85	0.58	0.068
HC-47	32.90	1.06	0.52	3635.00	1.79	2.04	9.53	0.94	0.59	0.082
HC-52	17.59	0.81	0.66	4797.50	2.06	1.95	8.66	0.87	0.63	0.082
HC-61	19.25	0.54	0.57	2875.00	2.02	2.21	10.39	0.98	0.67	0.086
HC-76	36.40	1.31	1.23	5876.67	4.43	4.31	20.40	1.99	1.47	0.210
HC-77	16.20	0.63	0.69	4526.67	2.36	2.26	10.56	1.06	0.83	0.113
HK-1	19.89	0.97	0.75	6028.33	2.41	2.14	9.02	0.89	0.63	0.085

Table 9
Orthopyroxene trace-element compositions (ppm)

Sample	Rb	Th	U	Nb	La	Ce	Pr	Sr	Nd	Sm	Zr	Hf	Eu	Ti	Gd	Dy	Y	Er	Yb	Lu
D-5	0.702	0.222	0.178	0.072	0.10	0.18	0.21	0.020	0.30	0.45	0.71	0.98	0.37	1.98	0.66	0.85	1.10	1.59	1.47	1.84
H-17	0.139	2.409	2.443	0.377	1.01	1.96	2.29	0.076	2.53	2.65	1.76	1.92	1.89	2.22	2.78	2.15	3.08	3.70	4.85	4.00
HA-12	<0.001	0.071	0.058	0.010	0.03	0.06	0.07	0.015	0.10	0.19	0.23	0.35	0.22	1.99	0.31	0.40	0.51	0.79	0.70	0.88
HA-21	0.004	0.223	0.209	0.062	0.14	0.15	0.21	0.038	0.24	0.36	0.30	0.46	0.34	2.52	0.51	0.54	0.74	0.92	1.02	1.06
HC-12	0.621	0.024	0.041	0.029	0.03	0.06	0.09	0.042	0.13	0.25	0.28	0.60	0.23	2.78	0.37	0.45	0.54	0.81	0.79	0.91

Table 10
Sr isotope compositions of Mauna Kea xenoliths

Sample	$^{87}Sr/^{86}Sr_{cpx}$	$^{87}Sr/^{86}Sr_{plag}$
D Cone	0.703507	–
D-4	0.703507	–
D-5	–	0.703573
HA-21	0.703560	0.703566
HC-10	–	0.703517
HC-12	0.703564	–
HC-21	0.703512	–
HK-1	0.703503	0.70351

Table 11
Pb isotope compositions of Mauna Kea xenoliths

	Clinopyroxene			Plagioclase		
Sample	$^{206}Pb/^{204}Pb_{cpx}$	$^{207}Pb/^{204}Pb_{cpx}$	$^{208}Pb/^{204}Pb_{cpx}$	$^{206}Pb/^{204}Pb_{plag}$	$^{207}Pb/^{204}Pb_{plag}$	$^{208}Pb/^{204}Pb_{plag}$
D-4	18.37	15.49	38.00	–	–	–
D-5	–	–	–	18.52	15.49	38.10
HA-21	18.50	15.49	38.08	18.50	15.47	38.04
HC-10	–	–	–	18.42	15.48	38.00
HC-12	18.50	15.49	38.07	–	–	–
HC-21	18.44	15.49	38.03	–	–	–
HK-1	18.38	15.49	37.98	18.38	15.48	37.97

Table 12
Calculated T_{REE} and T_{BKN} for each sample

Sample	T_{REE} (°C)	T_{BKN} (°C)
D-5	1331 (58)	927
H-17	1486 (100)	889
HA-12	1304 (14)	899
HA-21	1242 (38)	886
HC-12	1398 (29)	964

Supplementary Material

Table S1

EMPA analyses of (Cr) augite, hornblende, olivine, anorthoclase, and labradorite standards NMNH 164905, NMNH 143965, USNM 2566, NMNH 133868, and NMNH 115900 (wt. %)

Standard	n	Na_2O	Al_2O_3	Cr_2O_3	FeO	CaO	MgO	SiO_2	MnO	NiO	TiO_2	K_2O	Total
(Cr) Augite													
	9	0.79 (0.01)	8.21 (0.23)	0.91 (0.03)	4.88 (0.03)	17.42 (0.08)	17.10 (0.13)	49.93 (0.4)	0.13 (0.01)	0.06 (0.01)	0.47 (0.03)	–	99.9 (0.40)
Hornblende (Kakanui)													
	9	2.58 (0.06)	15.25 (0.18)	0.00 (0.02)	11.09 (0.26)	10.11 (0.07)	12.57 (0.12)	40.43 (0.29)	0.09 (0.01)	0.01 (0.01)	4.81 (0.07)	–	96.96 (0.52)
Olivine (Springwater)													
	5	–	–	–	16.68 (0.11)	0.00 (0.01)	43.84 (0.1)	39.26 (0.25)	0.27 (0.01)	0.01 (0.01)	–	100.09 (0.38)	16.68 (0.11)
Anorthoclase (Kakanui)													
	3	9.70 (0.07)	19.58 (0.16)	0.16 (0.01)	0.53 (0.01)	0.01 (0.01)	67.05 (0.64)	–	–	2.32 (0.02)	99.35 (0.85)	9.70 (0.07)	19.58 (0.16)
Labradorite													
	10	3.87 (0.06)	30.49 (0.32)	0.44 (0.01)	13.45 (0.16)	0.13 (0.01)	52.00 (0.31)	–	–	–	0.12 (0.01)	100.50 (0.72)	3.87 (0.06)

Table S2

Individual clinopyroxene major-element analyses by sample grain (wt. %)

Analysis	SiO_2	TiO_2	Al_2O_3	Cr_2O_3	FeO	MnO	MgO	CaO	Na_2O	NiO	Total
D Cone-CPX-1-CORE	52.80	0.64	2.51	1.01	4.58	0.15	16.65	22.00	0.36	0.05	100.74
D Cone-CPX-1-RIM	51.89	0.72	2.67	0.98	4.56	0.12	16.53	22.40	0.37	0.04	100.27
D Cone-CPX-2-CORE	52.57	0.63	2.38	1.07	4.58	0.11	17.02	21.93	0.32	0.03	100.65
D Cone-CPX-3-CORE	51.56	0.78	2.90	0.99	4.35	0.12	16.22	22.15	0.42	0.05	99.55
D Cone-CPX-3-RIM	51.72	0.79	2.99	0.96	4.24	0.13	16.26	22.67	0.44	0.06	100.26
D Cone-CPX-4-CORE	51.70	0.61	2.35	1.02	4.66	0.11	16.75	21.46	0.29	0.06	99.02
D Cone-CPX-4-RIM	53.62	0.63	2.33	1.04	4.79	0.09	17.00	21.42	0.33	0.05	101.31
D Cone-CPX-5	51.99	0.67	2.65	1.19	4.68	0.10	16.82	21.90	0.34	0.02	100.36
D-4-CPX-1-CORE	50.93	1.47	2.87	0.57	5.69	0.13	15.55	22.13	0.50	0.05	99.89
D-4-CPX-1-CORE-1	50.35	1.10	4.20	1.12	5.14	0.09	15.68	22.66	0.32	0.03	100.70
D-4-CPX-1-CORE-2	50.16	1.16	4.49	1.13	5.13	0.10	15.64	22.66	0.28	0.03	100.77
D-4-CPX-1-RIM	49.67	1.89	4.26	0.73	5.84	0.14	14.92	22.28	0.57	0.02	100.32
D-4-CPX-1-RIM	50.36	1.44	3.11	0.67	5.52	0.13	15.33	22.28	0.54	0.05	99.43
D-4-CPX-2-CORE	50.98	0.98	3.99	1.13	5.09	0.11	15.67	22.26	0.29	0.03	100.53
D-4-CPX-2-CORE	50.68	1.63	3.77	0.66	5.71	0.12	15.36	22.39	0.58	0.03	100.93
D-4-CPX-2-RIM	50.11	1.34	4.31	1.00	5.52	0.09	16.16	21.19	0.29	0.05	100.06
D-4-CPX-2-RIM	49.43	1.84	4.00	0.71	5.94	0.13	15.28	22.14	0.51	0.05	100.03
D-4-CPX-3	49.92	1.27	4.45	1.05	5.57	0.10	15.21	22.43	0.33	0.03	100.38
D-4-CPX-3-CORE	50.44	1.09	4.42	1.13	4.82	0.11	15.83	22.46	0.27	0.05	100.62

D-4-CPX-3-RIM	50.20	1.41	4.38	0.91	5.59	0.11	15.05	22.58	0.36	0.05	100.64
D-4-CPX-4	50.09	1.69	4.23	0.80	5.88	0.10	14.83	22.37	0.55	0.05	100.59
D-4-CPX-5	49.29	1.83	4.03	0.71	6.06	0.13	15.38	21.78	0.41	0.03	99.65
D-4-CPX-6-CORE	50.48	1.42	4.29	0.91	6.11	0.13	15.80	21.39	0.32	0.07	100.93
D-4-CPX-6-RIM	50.58	1.37	4.27	0.94	5.47	0.12	15.25	22.59	0.32	0.01	100.94
D-5-CPX-1-CORE	51.84	0.96	3.07	0.27	7.04	0.17	15.47	22.00	0.39	0.04	101.25
D-5-CPX-1-RIM	51.22	0.99	2.85	0.27	6.83	0.19	15.55	22.10	0.42	0.05	100.46
D-5-CPX-3-RIM	51.91	0.86	2.95	0.40	6.54	0.18	15.47	22.44	0.40	0.06	101.20
H-17-CPX-1-CORE	52.73	0.64	2.50	0.13	6.87	0.19	15.52	22.52	0.46	0.07	101.64
H-17-CPX-1-RIM	52.96	0.65	2.35	0.11	6.92	0.19	15.70	22.46	0.45	0.04	101.83
H-17-CPX-2-CORE	51.88	0.69	2.22	0.09	7.26	0.19	15.68	22.20	0.42	0.05	100.69
H-17-CPX-2-RIM	53.95	0.46	1.34	0.05	6.64	0.18	16.14	22.40	0.43	0.01	101.62
H-17-CPX-3-CORE	52.36	0.56	2.07	0.11	7.07	0.21	15.50	22.25	0.44	0.04	100.61
H-17-CPX-3-RIM	52.70	0.56	1.66	0.08	6.89	0.20	15.94	22.10	0.40	0.04	100.58
H-17-CPX-4-CORE	52.12	0.58	1.83	0.07	7.05	0.20	15.58	22.27	0.45	0.04	100.20
H-17-CPX-4-RIM	53.71	0.45	1.23	0.08	7.10	0.19	16.09	22.10	0.38	0.05	101.37
H-17-CPX-5-CORE	52.93	0.50	1.66	0.09	7.13	0.20	15.96	22.12	0.41	0.03	101.03
HA-12-CPX-1-A	51.80	0.93	3.17	0.49	6.37	0.17	15.57	22.52	0.41	0.04	101.48
HA-12-CPX-1-RIM	51.08	0.92	2.74	0.47	6.21	0.14	15.70	22.50	0.38	0.07	100.21
HA-12-CPX-2-CORE	51.22	0.98	2.80	0.44	6.31	0.19	15.72	22.72	0.40	0.05	100.84
HA-12-CPX-2-RIM	52.03	0.95	2.61	0.42	6.96	0.16	16.59	20.87	0.38	0.03	101.00
HA-12-CPX-3-CORE	51.68	0.93	2.79	0.36	6.40	0.16	15.87	22.22	0.37	0.04	100.83
HA-12-CPX-3-RIM	52.65	0.92	2.86	0.40	6.63	0.16	16.17	21.98	0.38	0.01	102.17
HA-12-CPX-4-CORE	52.63	0.87	2.65	0.32	6.56	0.15	16.14	21.89	0.40	0.03	101.63
HA-12-CPX-4-RIM	51.44	0.87	2.65	0.34	6.88	0.17	16.27	21.47	0.37	0.05	100.51
HA-12-CPX-5-CORE	51.89	0.92	2.76	0.35	6.04	0.19	15.89	22.71	0.36	0.04	101.13
HA-12-CPX-5-RIM	52.31	0.96	2.52	0.38	6.11	0.15	15.77	22.81	0.41	0.04	101.45
HA-12-CPX-6-CORE	52.18	0.86	2.72	0.41	5.96	0.14	15.86	22.97	0.39	0.01	101.50
HA-12-CPX-6-RIM	51.74	0.87	2.91	0.42	6.63	0.17	16.26	21.62	0.37	0.01	101.01
HA-21-CPX-1-RIM	51.56	1.07	3.06	0.37	6.85	0.19	16.04	21.70	0.39	0.03	101.26
HA-21-CPX-2-CORE	51.84	0.99	2.81	0.32	6.15	0.18	15.80	22.46	0.38	0.05	100.97
HA-21-CPX-2-RIM	52.26	1.03	3.00	0.46	6.22	0.18	15.79	22.47	0.41	0.01	101.82
HA-21-CPX-3-CORE	51.42	1.00	3.03	0.39	6.22	0.18	15.67	22.67	0.40	0.07	101.05
HA-21-CPX-3-RIM	53.12	0.82	2.52	0.33	8.78	0.22	19.02	16.67	0.31	0.03	101.83
HA-21-CPX-4-CORE	51.54	0.92	2.59	0.44	7.82	0.18	18.14	18.69	0.31	0.03	100.66
HA-21-CPX-4-RIM	52.33	0.98	2.91	0.43	6.13	0.17	15.80	22.55	0.40	0.03	101.73
HA-6-CPX-1-CORE	51.46	0.86	3.48	1.00	3.82	0.06	15.93	23.53	0.48	0.03	100.66
HA-6-CPX-1-RIM	51.46	1.02	3.82	1.08	4.01	0.09	15.66	22.97	0.47	0.05	100.63
HA-6-CPX-3-CORE	51.58	0.84	3.37	1.03	3.79	0.07	15.69	23.58	0.45	0.04	100.43
HA-6-CPX-3-RIM	52.84	0.82	3.40	1.17	3.75	0.09	15.65	23.70	0.42	0.02	101.86
HC-10-CPX-1-RIM	50.91	1.06	3.64	0.21	6.89	0.15	15.02	22.29	0.43	0.01	100.61
HC-10-CPX-2-CORE	48.01	1.89	3.48	0.27	10.88	0.17	14.45	21.08	0.33	0.04	100.60
HC-10-CPX-2-CORE	51.61	1.01	3.79	0.24	7.62	0.16	15.14	21.76	0.36	0.02	101.71

HC-10-CPX-2-RIM	51.22	0.98	3.05	0.14	8.70	0.20	16.53	19.49	0.31	0.05	100.67
HC-10-CPX-2-RIM	51.05	1.05	3.92	0.29	7.90	0.17	15.41	20.79	0.41	0.03	101.02
HC-10-CPX-3	51.14	0.96	3.27	0.23	6.91	0.16	15.19	22.51	0.37	0.02	100.76
HC-10-CPX-3-CORE	51.42	0.90	2.97	0.15	10.09	0.23	17.70	16.86	0.28	0.06	100.65
HC-10-CPX-3-RIM	51.17	1.27	3.86	0.21	7.31	0.18	14.81	22.25	0.42	0.03	101.53
HC-10-CPX-4	50.56	1.35	4.10	0.12	7.43	0.17	15.13	22.03	0.48	0.05	101.41
HC-10-CPX-4-CORE	50.14	1.55	3.52	0.33	8.33	0.21	14.81	21.78	0.40	0.05	101.11
HC-10-CPX-5-CORE	50.87	1.21	3.88	0.13	7.53	0.16	14.83	22.22	0.38	0.03	101.23
HC-12-CPX-1	52.20	0.76	3.12	0.73	5.95	0.14	17.42	20.34	0.34	0.01	101.02
HC-12-CPX-2	52.30	0.73	2.92	0.66	6.63	0.18	17.56	19.42	0.34	0.05	100.79
HC-12-CPX-3	51.78	0.91	3.12	0.79	5.90	0.14	15.81	22.01	0.39	0.05	100.89
HC-17-CPX-3	52.29	0.74	3.00	0.42	6.79	0.17	15.99	21.35	0.42	0.00	101.17
HC-17-CPX-4	53.12	0.71	2.55	0.13	7.26	0.19	15.77	21.34	0.41	0.02	101.50
HC-18 CG-CPX-1-CORE	52.93	0.89	3.08	0.58	5.50	0.14	16.13	22.86	0.36	0.03	102.51
HC-18 CG-CPX-1-CORE	51.92	0.98	3.08	0.14	7.50	0.17	15.44	21.76	0.39	0.05	101.43
HC-18 CG-CPX-1-RIM	52.08	0.93	3.13	0.67	5.24	0.16	15.92	22.93	0.37	0.06	101.50
HC-18 CG-CPX-1-RIM	51.35	1.19	3.72	0.18	7.50	0.18	14.80	22.09	0.40	0.06	101.47
HC-18 CG-CPX-2-RIM	52.18	0.93	2.97	0.13	7.25	0.18	15.28	22.38	0.37	0.02	101.70
HC-18 CG-CPX-4	52.01	0.86	2.63	0.13	7.23	0.20	15.10	22.45	0.36	0.01	100.99
HC-18 CG-CPX-5	50.99	0.99	2.78	0.15	8.08	0.18	15.88	20.62	0.36	0.03	100.07
HC-18 CG-CPX-6	51.99	1.09	3.26	0.15	7.42	0.19	14.88	22.09	0.41	0.03	101.51
HC-18 FG-CPX-1-CORE	50.62	1.22	3.98	0.30	8.22	0.20	15.24	20.62	0.43	0.05	100.88
HC-18 FG-CPX-1-RIM	52.14	0.88	2.58	0.14	7.26	0.16	15.26	22.24	0.37	0.01	101.04
HC-18 FG-CPX-2	51.67	1.06	3.36	0.03	7.81	0.22	15.10	21.78	0.39	0.00	101.42
HC-18 FG-CPX-2-CORE	51.18	1.02	3.08	0.54	6.22	0.17	15.62	22.58	0.40	0.05	100.85
HC-18 FG-CPX-2-RIM	51.48	0.99	2.99	0.43	6.29	0.14	15.80	22.30	0.41	0.04	100.88
HC-18 FG-CPX-3	51.41	1.18	3.25	-0.02	8.15	0.21	14.97	21.84	0.36	0.00	101.37
HC-18 FG-CPX-4-CORE	50.18	1.59	3.69	0.21	9.33	0.18	14.64	21.28	0.40	0.04	101.55
HC-18 FG-CPX-4-RIM	50.69	1.53	3.92	0.18	8.43	0.17	15.07	21.05	0.38	0.00	101.42
HC-18 FG-CPX-5	49.48	1.30	4.17	0.04	7.92	0.21	14.65	22.15	0.39	-0.01	100.30
HC-21-CPX-1-CORE	51.32	1.14	3.09	0.50	6.64	0.19	15.81	21.46	0.38	0.02	100.55
HC-21-CPX-1-CORE	52.16	1.21	3.14	0.41	6.65	0.17	15.75	21.89	0.38	0.04	101.79
HC-21-CPX-1-RIM	51.92	1.07	3.38	0.48	6.28	0.14	15.45	22.20	0.39	0.02	101.33
HC-21-CPX-2-CORE	50.76	1.17	2.82	0.42	6.64	0.14	15.56	21.71	0.37	0.03	99.62
HC-21-CPX-2-CORE	51.24	1.14	3.16	0.45	6.79	0.15	16.16	21.27	0.38	0.03	100.76
HC-21-CPX-2-RIM	51.69	1.15	3.01	0.40	6.97	0.19	15.94	20.68	0.38	0.05	100.44
HC-21-CPX-2-RIM	51.42	1.12	3.04	0.44	6.69	0.17	16.07	21.36	0.39	0.04	100.72
HC-21-CPX-3-CORE	51.48	1.09	2.91	0.44	6.93	0.14	16.42	20.42	0.36	0.05	100.23
HC-21-CPX-3-CORE	51.33	1.22	3.22	0.43	6.39	0.17	15.38	22.15	0.40	0.05	100.73
HC-21-CPX-3-RIM	52.49	0.84	2.86	0.45	7.03	0.17	16.42	20.22	0.35	0.02	100.87
HC-21-CPX-4-CORE	51.25	1.21	3.25	0.45	6.73	0.16	16.23	21.16	0.38	0.05	100.88
HC-21-CPX-4-CORE	51.32	0.74	2.50	0.51	6.37	0.15	15.90	22.01	0.34	0.05	99.89
HC-21-CPX-4-RIM	51.87	0.95	2.57	0.38	7.88	0.18	18.06	18.39	0.32	0.02	100.64

HC-25 D-CPX-1	51.89	0.75	3.19	0.97	6.21	0.17	16.32	21.19	0.34	0.02	101.04
HC-25 D-CPX-1-CORE	51.08	1.09	4.45	0.32	6.02	0.15	16.00	21.28	0.34	0.01	100.74
HC-25 D-CPX-1-CORE-1	50.65	1.11	4.75	0.52	6.05	0.14	15.88	21.33	0.37	0.04	100.84
HC-25 D-CPX-2	51.10	1.02	4.25	0.43	6.20	0.11	15.92	21.76	0.35	0.01	101.16
HC-25 D-CPX-2-CORE	51.91	0.86	3.59	0.56	6.30	0.14	16.27	21.08	0.32	0.05	101.08
HC-25 D-CPX-2-RIM	50.31	1.02	4.34	0.43	6.47	0.15	16.04	21.02	0.33	0.05	100.14
HC-25 D-CPX-3-CORE	50.40	1.07	4.91	0.22	6.33	0.16	15.87	20.98	0.32	0.04	100.30
HC-25 D-CPX-3-RIM	50.17	1.08	4.47	0.29	6.02	0.12	16.05	21.42	0.33	0.02	99.97
HC-25 D-CPX-4-CORE	53.32	0.87	3.63	0.37	6.43	0.13	16.39	21.16	0.35	0.04	102.68
HC-25 D-CPX-5-CORE	50.35	0.98	4.04	0.55	6.40	0.11	15.92	21.18	0.33	0.02	99.90
HC-25 D-CPX-5-RIM	51.46	1.01	4.10	0.36	6.06	0.15	16.07	21.01	0.32	0.04	100.58
HC-25 L-CPX-1a	51.77	1.00	4.32	0.57	5.35	0.13	16.22	21.60	0.34	0.05	101.34
HC-25 L-CPX-1B	50.48	1.05	4.35	0.65	5.13	0.14	16.14	21.56	0.38	0.04	99.93
HC-25 L-CPX-1C	51.08	1.06	4.35	0.55	5.34	0.13	15.88	21.42	0.38	0.04	100.24
HC-25 L-CPX-1-CORE	51.23	1.11	4.47	0.18	5.32	0.13	16.43	21.73	0.36	0.06	101.01
HC-25 L-CPX-2-CORE	51.01	1.11	4.29	0.21	6.49	0.14	15.92	21.45	0.37	0.04	101.02
HC-25 L-CPX-3-CORE	51.50	1.09	4.84	0.14	5.62	0.14	16.23	21.41	0.34	0.02	101.34
HC-25 L-CPX-4-CORE	51.13	1.02	4.20	0.36	5.73	0.13	16.06	21.30	0.34	0.04	100.31
HC-25 L-CPX-4-RIM	50.90	1.12	4.54	0.33	5.44	0.14	16.23	21.57	0.37	0.05	100.70
HC-26-CPX-1-CORE	50.19	1.17	3.50	0.43	6.46	0.19	15.59	21.87	0.46	0.03	99.89
HC-26-CPX-2-CORE	51.43	1.08	3.34	0.51	6.30	0.17	15.42	22.09	0.49	0.05	100.88
HC-26-CPX-2-RIM	47.55	2.10	3.41	1.34	11.18	0.18	15.54	19.25	0.50	0.06	101.11
HC-26-CPX-3-CORE	49.92	1.13	3.19	0.47	6.27	0.18	15.36	21.95	0.47	0.06	99.01
HC-26-CPX-3-RIM	51.60	0.88	2.35	0.30	7.37	0.21	17.34	19.13	0.39	0.06	99.61
HC-26-CPX-4-CORE	51.29	1.03	2.91	0.47	6.39	0.18	15.55	21.82	0.45	0.05	100.15
HC-26-CPX-5-CORE	51.70	0.77	2.77	0.42	6.85	0.20	15.40	21.93	0.46	0.06	100.58
HC-26-CPX-6-CORE	51.29	1.02	3.00	0.38	6.53	0.18	15.89	21.65	0.43	0.01	100.38
HC-26-CPX-6-CORE DUP	51.23	1.02	2.99	0.38	6.37	0.18	15.51	22.12	0.43	0.03	100.25
HC-26-CPX-6-CORE DUP 2	51.05	1.06	2.98	0.34	6.42	0.20	15.58	22.00	0.44	0.04	100.11
HC-28-CPX-1-1A	52.04	0.53	2.21	0.99	3.36	0.06	16.23	23.98	0.37	0.06	99.84
HC-28-CPX-1-1B	52.01	0.55	2.21	1.00	3.41	0.06	16.34	24.10	0.38	0.07	100.12
HC-47-CPX-1	55.32	0.59	2.16	1.12	3.11	0.05	17.12	22.76	0.44	0.03	102.72
HC-47-CPX-2	51.88	0.57	2.32	1.12	3.24	0.05	16.12	24.08	0.41	0.05	99.85
HC-52-CPX-1	51.03	0.96	3.62	0.71	6.13	0.13	15.73	21.25	0.40	0.06	100.03
HC-52-CPX-2-CORE	50.34	0.86	3.78	0.89	5.81	0.11	15.90	21.61	0.26	0.04	99.59
HC-52-CPX-2-RIM	51.39	0.84	3.99	0.89	5.73	0.10	15.97	21.72	0.27	0.04	100.94
HC-52-CPX-3-CORE	51.72	0.89	4.26	0.92	5.66	0.10	15.74	21.96	0.25	0.03	101.53
HC-52-CPX-3-RIM	50.14	0.83	4.04	0.99	5.70	0.13	15.67	21.83	0.30	0.05	99.68
HC-61-CPX-1-CORE	52.50	0.61	2.50	1.23	3.70	0.09	17.08	22.29	0.59	0.04	100.63
HC-61-CPX-1-RIM	53.89	0.54	2.45	1.16	3.49	0.09	16.79	23.08	0.59	0.08	102.16
HC-61-CPX-2-CORE	52.91	0.55	2.36	1.19	3.41	0.07	16.66	23.18	0.59	0.06	100.97
HC-61-CPX-4-CORE	53.58	0.53	2.54	1.13	3.44	0.05	16.82	23.11	0.56	0.07	101.84
HC-61-CPX-4-RIM	53.13	0.55	2.20	1.12	3.30	0.05	16.47	23.61	0.52	0.05	101.00

HC-76-CPX-1-CORE	48.28	1.75	2.80	0.79	10.62	0.19	16.72	18.48	0.32	0.06	100.02
HC-76-CPX-2-CORE	51.18	1.06	3.44	0.46	6.59	0.16	15.65	22.27	0.39	0.03	101.24
HC-76-CPX-2-RIM	51.40	1.03	3.18	0.45	6.72	0.17	15.82	21.48	0.40	0.05	100.70
HC-76-CPX-3	51.34	1.06	3.23	0.41	6.82	0.17	15.28	21.91	0.44	0.03	100.69
HC-76-CPX-4-CORE	51.68	0.77	2.24	0.23	10.98	0.24	20.49	12.90	0.25	0.05	99.83
HC-77-CPX-1-CORE	53.06	0.55	2.23	0.63	6.25	0.16	16.39	21.73	0.36	0.04	101.41
HC-77-CPX-1-RIM	50.68	1.02	2.99	0.48	6.53	0.14	16.06	21.46	0.38	0.03	99.77
HC-77-CPX-2	51.68	1.09	2.97	0.43	6.13	0.16	15.96	22.06	0.40	0.04	100.92
HC-77-CPX-2A	51.51	0.89	2.62	0.49	6.42	0.19	15.76	21.94	0.36	0.04	100.21
HC-77-CPX-2B	52.79	0.97	2.72	0.42	6.83	0.16	16.42	21.07	0.34	0.01	101.72
HC-77-CPX-3	51.38	1.09	2.79	0.49	6.25	0.16	15.63	22.11	0.38	0.02	100.31
HC-77-CPX-3-RIM	51.86	1.03	3.04	0.45	6.03	0.13	15.94	21.72	0.39	0.02	100.61
HK-1-CPX-1-CORE	50.28	1.06	3.94	0.90	5.75	0.13	15.52	22.17	0.29	0.05	100.09
HK-1-CPX-1-RIM	50.29	1.13	4.50	0.99	5.90	0.13	15.50	21.95	0.34	0.05	100.76
HK-1-CPX-2	50.73	1.07	4.24	0.95	5.94	0.11	15.32	21.96	0.27	0.04	100.62
HK-1-CPX-3-CORE	49.26	1.30	4.51	0.40	5.88	0.13	15.23	22.18	0.29	0.06	99.23
HK-1-CPX-3-RIM	49.59	1.14	4.60	0.55	6.06	0.13	15.20	22.16	0.31	0.06	99.82
HK-1-CPX-4	49.73	1.23	3.91	0.77	5.82	0.11	15.62	21.95	0.32	0.02	99.48
HK-1-CPX-5-CORE	51.45	0.81	3.58	0.88	4.98	0.12	15.87	22.40	0.27	0.06	100.41
HK-1-CPX-5-RIM	50.60	1.00	4.60	0.95	5.72	0.14	15.64	22.09	0.37	0.03	101.14

Table S3

Individual orthopyroxene major-element analyses by sample grain (wt. %)

Analysis	SiO_2	TiO_2	Al_2O_3	Cr_2O_3	FeO	MnO	MgO	CaO	Na_2O	NiO	Total
D-5-OPX-1-CORE	54.59	0.38	1.15	0.10	15.13	0.32	28.51	0.93	0.00	0.10	101.21
D-5-OPX-1-RIM	54.03	0.37	1.47	0.11	15.21	0.32	28.36	0.93	0.00	0.07	100.86
D-5-OPX-2-CORE	54.73	0.36	1.39	0.11	15.13	0.34	28.18	0.94	0.03	0.03	101.23
D-5-OPX-2-CORE	54.73	0.44	1.11	0.11	15.13	0.33	28.29	1.25	0.01	0.05	101.46
D-5-OPX-2-RIM	55.18	0.41	1.34	0.13	15.02	0.29	28.37	1.02	-0.01	0.08	101.82
D-5-OPX-3	55.65	0.37	1.36	0.09	15.39	0.30	28.37	0.94	0.01	0.07	102.53
D-5-OPX-4	54.82	0.35	1.27	0.12	15.18	0.30	28.46	0.91	0.02	0.12	101.55
D-5-OPX-5	54.47	0.38	1.36	0.15	14.80	0.29	27.96	1.78	0.03	0.08	101.32
D-5-OPX-6	54.29	0.45	1.22	0.09	15.13	0.30	28.14	1.20	0.01	0.08	100.91
HA-12-OPX-1-CORE	55.41	0.47	1.45	0.21	14.09	0.31	29.06	1.05	0.01	0.05	102.10
HA-12-OPX-1-RIM	54.74	0.45	1.40	0.21	14.09	0.32	29.22	0.89	0.02	0.07	101.40
HA-12-OPX-2-CORE	56.16	0.41	1.13	0.08	14.14	0.30	28.80	1.22	0.00	0.08	102.32
HA-12-OPX-2-RIM	55.69	0.34	1.17	0.10	14.28	0.30	28.85	0.93	-0.01	0.09	101.73
HA-12-OPX-3-CORE	53.46	0.45	1.40	0.23	13.60	0.28	28.47	2.20	0.03	0.15	100.26
HA-12-OPX-4-CORE	55.93	0.44	1.52	0.19	13.44	0.28	28.93	1.89	0.00	0.04	102.67
HA-12-OPX-4-RIM	55.75	0.40	1.35	0.17	13.86	0.29	29.43	0.78	0.00	0.06	102.08
HA-12-OPX-5-CORE	55.42	0.46	1.52	0.19	13.88	0.29	29.02	1.01	0.05	0.04	101.88
HA-12-OPX-5-RIM	54.47	0.45	1.33	0.19	13.74	0.30	28.44	1.83	0.06	0.04	100.86

HA-12-OPX-6	53.63	0.44	1.54	0.21	13.67	0.30	28.68	1.61	0.04	0.09	100.21
HA-21-OPX-1	55.46	0.51	1.72	0.21	13.26	0.28	28.47	1.95	0.05	0.07	101.96
HA-21-OPX-2-CORE	54.92	0.41	1.25	0.14	13.86	0.29	28.97	0.77	0.02	0.07	100.70
HA-21-OPX-2-RIM	53.76	0.47	1.62	0.21	13.38	0.26	28.27	1.97	0.01	0.05	100.00
HA-21-OPX-3	54.87	0.73	1.28	0.22	13.77	0.28	28.79	1.52	0.01	0.06	101.54
HA-21-OPX-4-CORE	54.56	0.43	1.55	0.20	13.56	0.29	28.33	1.89	0.04	0.06	100.90
HA-21-OPX-4-RIM	54.70	0.48	1.68	0.19	13.64	0.28	28.28	1.78	0.03	0.04	101.08
HA-21-OPX-5	54.94	0.45	1.19	0.18	14.09	0.29	28.62	0.93	0.01	0.06	100.74
HC-12-OPX-1-CORE	55.41	0.49	1.78	0.20	12.38	0.25	29.94	1.07	0.04	0.10	101.66
HC-12-OPX-1-RIM	55.40	0.55	1.74	0.15	12.40	0.25	29.75	1.05	0.01	0.07	101.37
HC-12-OPX-2-CORE	55.12	0.81	1.52	0.10	11.90	0.24	28.97	2.70	0.05	0.06	101.47
HC-12-OPX-2-RIM	55.30	0.54	1.47	0.12	12.54	0.28	29.90	1.08	0.01	0.07	101.30
H-17-OPX-1-CORE	55.35	0.22	1.28	0.06	15.08	0.33	28.80	0.75	0.02	0.08	101.97
H-17-OPX-1-RIM	55.21	0.23	0.79	0.01	15.03	0.38	28.59	0.96	0.03	0.07	101.31
H-17-OPX-2-CORE	54.91	0.25	1.13	0.07	15.11	0.35	27.87	1.29	0.01	0.07	101.06
H-17-OPX-2-RIM	54.16	0.26	1.05	0.06	15.15	0.34	28.20	0.80	0.02	0.05	100.09

Table S4

Individual olivine major-element analyses by sample grain (wt. %)

Analysis	SiO_2	TiO_2	Al_2O3	FeO	NiO	MnO	MgO	CaO	Na_2O	Total
H-17-OLIVINE-1a	39.80	0.00	0.00	14.51	0.30	0.15	45.15	0.08	0.00	99.99
H-17-OLIVINE-1b	38.96	0.00	0.03	14.68	0.29	0.20	44.86	0.09	0.00	99.11
H-17-OLIVINE-2a	39.79	0.00	0.01	14.51	0.32	0.16	45.21	0.09	0.00	100.10
H-17-OLIVINE-3a	39.61	0.00	0.01	14.87	0.28	0.17	45.32	0.09	0.00	100.34
H-17-OLIVINE-3b	40.15	0.00	0.02	14.71	0.29	0.17	45.45	0.09	0.00	100.88
D-5-OLIVINE-1a	38.22	0.00	0.03	23.83	0.32	0.27	38.51	0.04	0.00	101.22
D-5-OLIVINE-2a	36.23	0.00	0.01	21.91	0.31	0.22	36.78	0.04	0.00	95.49
D-5-OLIVINE-2b	38.03	0.00	0.03	22.68	0.32	0.26	38.39	0.04	0.00	99.75
D-5-OLIVINE-3a	38.01	0.00	0.00	23.37	0.28	0.29	38.23	0.05	0.00	100.24
D-5-OLIVINE-5a	37.46	0.00	0.00	23.33	0.31	0.25	37.68	0.04	0.00	99.06
D-4-OLIVINE-5a	38.91	0.00	0.04	17.93	0.20	0.25	42.25	0.08	0.00	99.67
D-4-OLIVINE-5b	38.72	0.00	0.03	18.14	0.23	0.19	42.33	0.07	0.00	99.72
D-4-OLIVINE-1a	38.64	0.00	0.02	18.23	0.24	0.24	42.35	0.05	0.00	99.77
D-4-OLIVINE-2a	38.19	0.00	0.00	18.22	0.25	0.21	42.12	0.05	0.00	99.05
D-4-OLIVINE-4a	38.55	0.00	0.02	18.03	0.25	0.22	42.34	0.03	0.00	99.44
D Cone-OLIVINE-1a	39.09	0.00	0.03	14.66	0.32	0.15	45.18	0.09	0.00	99.52
D Cone-OLIVINE-3a	39.50	0.00	0.01	14.54	0.26	0.16	45.04	0.09	0.00	99.61
D Cone-OLIVINE-3b	39.27	0.00	0.02	14.61	0.30	0.18	45.10	0.09	0.00	99.57
D Cone-OLIVINE-2a	39.53	0.00	0.01	14.49	0.29	0.19	45.30	0.08	0.00	99.89
HA-21-OLIVINE-1a	38.51	0.00	0.00	20.80	0.26	0.26	40.20	0.04	0.00	100.07
HA-21-OLIVINE-1b	38.26	0.00	0.02	21.01	0.24	0.22	40.52	0.04	0.00	100.31
HA-21-OLIVINE-3a	38.63	0.00	0.00	20.85	0.26	0.24	40.45	0.04	0.00	100.48

HA-21-OLIVINE-4a	37.94	0.00	0.00	21.16	0.24	0.23	39.96	0.05	0.00	99.57
HA-21-OLIVINE-4b	38.42	0.00	0.02	21.31	0.29	0.27	40.27	0.05	0.00	100.64
HA-21-OLIVINE-2a	38.56	0.00	0.01	20.76	0.29	0.27	40.44	0.04	0.00	100.36
HA-6-OLIVINE-4a	39.89	0.00	0.02	13.04	0.33	0.15	46.53	0.18	0.00	100.13
HA-6-OLIVINE-3a	39.60	0.00	0.02	13.33	0.37	0.16	46.51	0.19	0.00	100.18
HA-6-OLIVINE-3b	39.53	0.00	0.01	13.18	0.30	0.12	46.27	0.18	0.00	99.61
HA-6-OLIVINE-2a	40.35	0.00	0.01	13.12	0.33	0.15	46.64	0.18	0.00	100.78
HA-6-OLIVINE-1a	39.87	0.00	0.02	13.16	0.35	0.13	46.41	0.19	0.00	100.13
HC-10-OLIVINE-3a	37.76	0.00	0.00	24.03	0.17	0.28	37.51	0.04	0.00	99.80
HC-10-OLIVINE-5a	37.78	0.00	0.00	24.42	0.20	0.28	37.40	0.04	0.00	100.11
HC-10-OLIVINE-2a	37.83	0.00	0.02	24.57	0.18	0.23	37.44	0.05	0.00	100.34
HC-10-OLIVINE-2b	37.60	0.00	0.00	24.43	0.21	0.20	37.24	0.05	0.00	99.73
HC-10-OLIVINE-1a	37.77	0.00	0.01	24.53	0.17	0.22	37.55	0.04	0.00	100.30
HC-10-OLIVINE-4a	38.18	0.00	0.02	23.93	0.21	0.21	37.95	0.05	0.00	100.55
HC-12-OLIVINE-2a	39.18	0.00	0.00	18.46	0.27	0.18	41.96	0.05	0.00	100.10
HC-12-OLIVINE-1a	39.21	0.00	0.03	17.53	0.30	0.19	42.67	0.05	0.00	99.97
HC-12-OLIVINE-1b	39.27	0.00	0.00	17.77	0.28	0.18	42.64	0.05	0.00	100.18
HC-12-OLIVINE-3a	39.10	0.00	0.03	18.78	0.26	0.20	41.94	0.04	0.00	100.36
HC-28-OLIVINE-1a	39.82	0.00	0.01	13.22	0.33	0.17	46.46	0.20	0.00	100.21
HC-28-OLIVINE-2a	40.24	0.00	0.02	13.44	0.31	0.16	47.02	0.19	0.00	101.37
HC-28-OLIVINE-3a	39.35	0.00	0.04	13.09	0.29	0.16	45.94	0.20	0.00	99.06
HC-28-OLIVINE-3b	40.05	0.00	0.02	13.19	0.31	0.13	46.66	0.19	0.00	100.55
HC-28-OLIVINE-4a	39.60	0.00	0.03	13.28	0.32	0.13	46.24	0.20	0.00	99.79
HC-28-OLIVINE-5a	39.66	0.00	0.03	13.28	0.31	0.15	46.39	0.20	0.00	100.02
HC-26-OLIVINE-1a	37.96	0.00	0.00	21.39	0.29	0.24	39.89	0.06	0.00	99.83
HC-26-OLIVINE-2a	38.41	0.00	0.02	21.25	0.27	0.24	40.10	0.05	0.00	100.34
HC-26-OLIVINE-3a	38.44	0.00	0.02	21.00	0.26	0.25	40.13	0.05	0.00	100.15
HC-26-OLIVINE-4a	38.06	0.00	0.03	21.47	0.31	0.27	40.14	0.07	0.00	100.35
HC-26-OLIVINE-4b	38.55	0.00	0.03	21.25	0.28	0.23	40.24	0.06	0.00	100.63
HC-25 L-OLIVINE-1A	39.15	0.00	0.01	14.82	0.28	0.12	45.91	0.09	0.00	100.38
HC-25 L-OLIVINE-2A	38.95	0.00	0.03	14.71	0.28	0.14	45.82	0.10	0.00	100.04
HC-25 L-OLIVINE-3A	39.67	0.00	0.01	14.75	0.24	0.15	45.73	0.08	0.00	100.63
HC-25 L-OLIVINE-4a	39.39	0.00	0.02	14.39	0.26	0.18	45.69	0.09	0.00	100.04
HC-25 L-OLIVINE-5a	39.85	0.00	0.02	14.19	0.31	0.14	45.59	0.08	0.00	100.18
HC-25 D-OLIVINE-1a	38.90	0.00	0.02	16.30	0.23	0.18	43.58	0.09	0.00	99.29
HC-25 D-OLIVINE-1b	38.50	0.00	0.03	16.05	0.24	0.18	42.98	0.08	0.00	98.06
HC-25 D-OLIVINE-2a	39.20	0.00	0.02	17.47	0.24	0.15	43.36	0.09	0.00	100.53
HC-25 D-OLIVINE-3a	38.96	0.00	0.01	17.36	0.20	0.17	43.19	0.09	0.00	99.97
HC-25 D-OLIVINE-4a	38.80	0.00	0.02	17.98	0.21	0.19	43.32	0.10	0.00	100.61
HC-25 D-OLIVINE-5a	38.87	0.00	0.03	17.74	0.19	0.20	43.15	0.08	0.00	100.27
HC-25 D-OLIVINE-5b	38.80	0.00	0.02	17.48	0.21	0.14	43.10	0.07	0.00	99.83
HC-25 D-OLIVINE-6a	39.51	0.00	0.03	17.23	0.24	0.15	43.40	0.08	0.00	100.64
HC-21-OLIVINE-1a	38.27	0.00	0.00	20.82	0.25	0.22	40.59	0.05	0.00	100.20

HC-21-OLIVINE-2a	38.34	0.00	0.03	20.95	0.22	0.24	40.48	0.06	0.00	100.31
HC-21-OLIVINE-3a	38.36	0.00	0.01	21.01	0.25	0.24	40.66	0.05	0.00	100.58
HC-21-OLIVINE-4a	38.55	0.00	0.00	20.97	0.24	0.21	40.57	0.06	0.00	100.60
HC-47-OLIVINE-1a	40.25	0.00	0.01	12.09	0.39	0.12	47.85	0.18	0.00	100.90
HC-47-OLIVINE-2a	40.22	0.00	0.01	11.88	0.35	0.11	47.74	0.19	0.00	100.50
HC-47-OLIVINE-2b	40.16	0.00	0.02	11.76	0.40	0.14	47.75	0.21	0.00	100.42
HC-47-OLIVINE-3a	40.34	0.00	0.03	11.96	0.39	0.13	47.86	0.20	0.00	100.91
HC-47-OLIVINE-4a	39.87	0.00	0.03	11.79	0.36	0.09	47.59	0.18	0.00	99.92
HC-47-OLIVINE-5a	40.42	0.00	0.01	11.93	0.36	0.12	47.88	0.19	0.00	100.91
HC-52-OLIVINE-1a	40.05	0.00	0.00	13.13	0.34	0.13	46.70	0.20	0.00	100.55
HC-52-OLIVINE-1b	39.87	0.00	0.01	13.40	0.30	0.15	46.79	0.20	0.00	100.72
HC-61-1a	40.15	0.00	0.01	12.17	0.38	0.10	47.69	0.19	0.00	100.69
HC-61-2a	40.27	0.00	0.02	11.80	0.39	0.12	47.63	0.18	0.00	100.41
HC-61-3a	40.56	0.00	0.01	12.20	0.38	0.11	47.76	0.18	0.00	101.21
HC-61-4a	40.39	0.00	0.02	11.97	0.40	0.14	47.78	0.19	0.00	100.90
HC-61-4b	40.26	0.00	0.02	11.82	0.41	0.14	47.44	0.19	0.00	100.28
HC-61-5a	40.25	0.00	0.02	11.84	0.41	0.14	47.70	0.19	0.00	100.55
HC-76-1a	38.21	0.00	0.02	21.88	0.23	0.21	39.29	0.06	0.00	99.89
HC-76-2a	38.38	0.00	0.00	21.90	0.23	0.25	39.72	0.05	0.00	100.55
HC-76-3a	38.33	0.00	0.01	21.84	0.24	0.26	39.64	0.07	0.00	100.39
HC-76-4a	38.32	0.00	0.02	21.84	0.27	0.19	39.93	0.06	0.00	100.62
HK-1-OLIVINE-1a	39.59	0.00	0.00	15.87	0.28	0.18	44.98	0.06	0.00	100.97
HK-1-OLIVINE-2a	38.94	0.00	0.00	17.46	0.27	0.19	43.43	0.05	0.00	100.35
HK-1-OLIVINE-3a	38.94	0.00	0.02	17.33	0.22	0.19	43.47	0.06	0.00	100.23
HK-1-OLIVINE-3b	39.37	0.00	0.00	17.48	0.28	0.18	43.52	0.06	0.00	100.89
HK-1-OLIVINE-4a	39.38	0.00	0.00	17.36	0.27	0.21	43.39	0.06	0.00	100.67
HK-1-OLIVINE-5a	39.38	0.00	0.01	17.56	0.27	0.17	43.84	0.06	0.00	101.29

Table S5

Individual plagioclase major-element analyses by sample grain (wt. %)

Analysis	SiO_2	Al_2O_3	FeO	MgO	CaO	Na_2O	K_2O	Total
D-4-PLAG-1a	50.81	30.56	0.60	0.21	13.81	3.56	0.34	99.89
D-4-PLAG-2a	52.06	29.70	0.27	0.03	12.81	4.09	0.24	99.20
D-4-PLAG-3a	47.59	32.59	0.27	0.03	16.11	2.27	0.14	98.99
D-4-PLAG-4a	50.71	31.65	0.27	0.04	14.24	3.51	0.15	100.56
D-4-PLAG-5a	50.18	31.51	0.25	0.01	14.41	3.34	0.05	99.75
D-5-PLAG-1a	53.86	28.47	0.28	0.05	11.17	5.01	0.29	99.12
D-5-PLAG-2a	53.43	29.28	0.27	0.02	12.05	4.71	0.29	100.05
D-5-PLAG-3a	53.73	29.18	0.28	0.04	12.05	4.65	0.30	100.23
D-5-PLAG-4a	51.23	31.25	0.29	0.03	14.22	3.61	0.18	100.80
D-5-PLAG-5a	53.13	29.53	0.30	0.03	12.28	4.39	0.26	99.91

H-17-PLAG-1a	57.40	26.43	0.35	0.02	8.73	6.28	0.65	99.87
H-17-PLAG-2a	56.28	27.06	0.32	0.02	9.51	5.83	0.46	99.49
H-17-PLAG-3a	54.47	29.04	0.32	0.02	11.48	4.97	0.26	100.55
H-17-PLAG-4a	54.37	28.73	0.36	0.03	11.35	5.04	0.31	100.18
HA-12-PLAG-1a	50.69	31.35	0.28	0.03	14.40	3.37	0.12	100.24
HA-12-PLAG-2a	50.83	30.71	0.25	0.04	13.95	3.58	0.13	99.50
HA-12-PLAG-3a	50.75	31.34	0.27	0.03	14.19	3.65	0.13	100.37
HA-12-PLAG-4a	50.59	30.99	0.28	0.04	14.06	3.60	0.12	99.68
HA-12-PLAG-5a	51.60	30.85	0.28	0.02	13.74	3.76	0.14	100.39
HA-21-PLAG-1a	49.81	30.70	0.28	0.04	14.26	3.23	0.14	98.46
HA-21-PLAG-2a	49.89	31.55	0.30	0.05	14.74	3.18	0.12	99.83
HA-21-PLAG-3a	49.31	31.20	0.29	0.05	14.67	3.06	0.12	98.70
HA-21-PLAG-4a	49.06	32.46	0.30	0.03	15.58	2.73	0.09	100.26
HA-21-PLAG-5a	50.42	30.79	0.28	0.04	14.07	3.42	0.14	99.16
HA-21-PLAG-6a	49.21	31.42	0.26	0.02	14.78	2.91	0.11	98.72
HC-10-PLAG-1a	50.28	30.77	0.35	0.02	14.16	3.40	0.11	99.08
HC-10-PLAG-2a	50.70	30.73	0.27	0.02	14.03	3.72	0.07	99.54
HC-10-PLAG-3a	50.81	29.98	0.29	0.03	13.53	3.74	0.10	98.48
HC-10-PLAG-4a	50.31	30.66	0.29	0.02	13.89	3.51	0.11	98.79
HC-10-PLAG-5a	50.83	30.79	0.25	0.03	13.76	3.75	0.10	99.50
HC-12-PLAG-1a	49.29	32.09	0.25	0.04	15.35	2.72	0.10	99.83
HC-12-PLAG-2a	49.16	31.99	0.26	0.03	15.34	2.70	0.11	99.58
HC-12-PLAG-4a	53.35	28.78	0.24	0.04	11.76	4.69	0.23	99.09
HC-12-PLAG-5a	47.73	31.95	0.24	0.03	15.66	2.42	0.10	98.12
HC-18 CG-PLAG-1a	51.47	30.79	0.37	0.03	13.67	3.65	0.17	100.15
HC-18 CG-PLAG-2a	51.33	30.56	0.38	0.04	13.74	3.70	0.15	99.90
HC-18 CG-PLAG-3a	52.79	30.08	0.36	0.03	12.89	4.17	0.21	100.52
HC-18 CG-PLAG-4a	50.83	30.80	0.35	0.04	13.93	3.50	0.16	99.60
HC-18 CG-PLAG-5a	52.10	30.51	0.36	0.03	13.56	3.84	0.15	100.55
HC-18 FG-PLAG-1a	51.63	30.54	0.34	0.03	13.51	3.76	0.14	99.96
HC-18 FG-PLAG-2a	50.92	30.78	0.36	0.03	13.88	3.62	0.12	99.71
HC-18 FG-PLAG-3a	51.28	30.87	0.36	0.03	13.75	3.67	0.13	100.09
HC-18 FG-PLAG-4a	50.15	31.18	0.33	0.04	14.34	3.39	0.11	99.55
HC-21-PLAG-1a	52.43	29.91	0.26	0.04	12.83	4.30	0.18	99.95
HC-21-PLAG-2a	51.74	29.79	0.25	0.06	12.91	4.16	0.23	99.13
HC-21-PLAG-3a	52.07	29.68	0.31	0.03	12.73	4.11	0.20	99.14
HC-21-PLAG-4a	51.41	29.93	0.28	0.05	12.95	4.15	0.21	98.98
HC-21-PLAG-5a	51.02	30.20	0.29	0.04	13.35	3.81	0.20	98.91
HC-26-PLAG-1a	52.74	29.56	0.23	0.04	12.39	4.45	0.14	99.54
HC-26-PLAG-2a	52.44	29.63	0.25	0.06	12.42	4.34	0.16	99.29
HC-26-PLAG-3a	53.22	29.48	0.24	0.03	11.95	4.64	0.16	99.73
HC-26-PLAG-4a	52.87	29.26	0.27	0.03	12.06	4.40	0.18	99.08
HC-26-PLAG-5a	52.42	29.46	0.25	0.03	12.34	4.37	0.12	98.99

HC-52-PLAG-1a	51.39	29.84	0.29	0.05	12.78	3.89	0.38	98.63
HC-52-PLAG-2a	50.30	30.75	0.30	0.05	14.10	3.25	0.31	99.06
HC-52-PLAG-3a	50.22	30.69	0.30	0.06	14.01	3.31	0.19	98.79
HC-52-PLAG-4a	51.53	30.31	0.33	0.05	13.44	3.88	0.21	99.75
HC-52-PLAG-5a	50.81	31.02	0.32	0.06	14.00	3.60	0.21	100.03
HC-76-PLAG-1a	52.41	30.06	0.30	0.03	12.82	4.20	0.19	100.02
HC-76-PLAG-2a	52.22	29.87	0.32	0.02	12.84	4.15	0.19	99.61
HC-76-PLAG-3a	52.37	29.95	0.28	0.04	12.86	4.19	0.17	99.86
HC-76-PLAG-4a	52.55	30.01	0.31	0.02	12.88	4.26	0.19	100.21
HC-77-PLAG-1a	52.51	30.00	0.26	0.06	12.72	4.20	0.21	99.95
HC-77-PLAG-2a	52.25	30.08	0.29	0.03	12.87	4.11	0.20	99.83
HC-77-PLAG-3a	52.33	29.27	0.29	0.06	12.32	4.19	0.23	98.68
HC-77-PLAG-4a	51.71	30.34	0.31	0.04	13.22	3.86	0.17	99.64
HC-77-PLAG-5a	52.73	30.26	0.28	0.04	13.00	4.13	0.21	100.65
HC-77-PLAG-6a	52.48	30.03	0.25	0.04	12.81	4.28	0.23	100.13
HC-77-PLAG-7a	52.22	30.21	0.33	0.05	13.09	4.06	0.23	100.19
HK-1-PLAG-1a	46.74	33.57	0.25	0.01	16.98	1.85	0.07	99.47
HK-1-PLAG-2a	46.88	33.34	0.31	0.02	17.02	1.85	0.09	99.51
HK-1-PLAG-3a	46.59	33.83	0.28	0.04	17.02	1.80	0.06	99.63
HK-1-PLAG-4a	46.77	33.30	0.25	0.02	16.85	1.87	0.07	99.14

Table S6

Individual spinel major-element analyses by sample grain (wt. %)

Analysis	SiO_2	TiO_2	Al_2O_3	Cr_2O_3	FeO	MnO	MgO	CaO	Total
HA-6-SPINEL-1a	0.04	2.20	14.97	37.78	32.77	0.21	10.27	0.00	98.25
HA-6-SPINEL-1b	0.04	2.28	15.31	37.79	33.07	0.17	10.70	0.00	99.34
HA-6-SPINEL-2a	0.00	2.24	14.45	38.89	31.47	0.20	10.48	0.00	97.71
HA-6-SPINEL-2b	0.06	2.76	14.42	39.18	32.22	0.17	10.37	0.01	99.19
HC-25 L-SPINEL-1a	0.04	2.17	18.23	33.63	34.23	0.18	10.07	0.00	98.54
HC-25 L-SPINEL-1b	0.06	2.27	18.41	33.52	33.73	0.17	10.12	0.00	98.28
HC-25 L-SPINEL-1c	0.04	2.08	18.13	33.80	34.25	0.16	10.06	0.00	98.53
HC-25 L-SPINEL-2a	0.01	2.28	17.57	34.53	34.05	0.19	9.95	0.01	98.59
HC-25 L-SPINEL-3a	0.04	2.16	19.02	33.20	33.93	0.19	10.53	0.01	99.09
HC-25 L-SPINEL-4a	0.02	2.25	18.91	33.16	34.14	0.21	10.19	0.01	98.89
HC-28-SPINEL-1a	0.07	2.14	13.07	42.27	30.45	0.21	9.82	0.02	98.04
HC-28-SPINEL-2a	0.00	1.99	13.27	41.53	30.80	0.19	9.93	0.00	97.70
HC-28-SPINEL-3a	0.03	2.14	13.27	41.44	30.88	0.18	9.88	0.00	97.81
HC-28-SPINEL-4a	0.02	2.21	13.08	42.08	30.96	0.17	9.82	0.00	98.35
HC-47-SPINEL-1a	0.01	1.91	14.24	42.28	28.21	0.15	11.05	0.00	97.85
HC-47-SPINEL-2a	0.00	1.92	14.11	42.89	27.90	0.18	10.91	0.00	97.91
HC-47-SPINEL-3a	0.08	2.00	14.36	43.67	28.38	0.18	11.18	0.00	99.86

HC-47-SPINEL-4a	0.01	2.02	15.37	40.61	28.28	0.19	11.15	0.01	97.64
HC-47-SPINEL-5a	0.02	1.92	14.89	41.28	28.69	0.19	11.02	0.00	98.00
HC-47-SPINEL-6a	0.07	1.95	15.16	40.77	28.54	0.19	10.98	0.00	97.66
HC-47-SPINEL-7a	0.00	2.16	13.98	42.76	28.22	0.20	10.68	0.00	98.00
HC-61-SPINEL-2a	0.04	1.71	13.88	43.57	27.40	0.16	10.89	0.00	97.65
HC-61-SPINEL-3a	0.02	2.07	13.96	43.80	27.79	0.15	10.90	0.03	98.72
HC-61-SPINEL-3b	0.04	1.83	13.82	43.91	28.05	0.17	10.91	0.01	98.73
HC-61-SPINEL-3c	0.07	1.94	13.85	43.89	28.65	0.18	10.80	0.00	99.39
HC-61-SPINEL-4a	0.02	2.08	13.93	43.15	28.35	0.18	11.12	0.00	98.82
HC-61-SPINEL-5a	0.05	2.04	13.94	44.58	27.86	0.17	10.78	0.00	99.42
HC-61-SPINEL-6a	0.05	1.50	13.75	43.74	27.60	0.20	10.99	0.00	97.83

Table S7

Average BCR-2G recoveries vs. NIST 612 analyzed on the LA-ICP-MS (n=12)

Na	Ca	Ti	Rb	Sr	Y	Zr	Nb	La	Ce
23368.33 (535.79)	47925.00 (1299.04)	14337.50 (237.45)	47.04 (0.94)	310.74 (5.33)	30.79 (0.55)	170.48 (2.17)	12.76 (0.27)	23.47 (0.37)	50.85 (1.05)

Pr	Nd	Sm	Eu	Gd	Dy	Er	Yb	Lu	Hf
6.08 (0.11)	27.29 (0.56)	6.21 (0.17)	1.82 (0.05)	6.06 (0.16)	6.01 (0.16)	3.36 (0.11)	3.22 (0.09)	0.45 (0.01)	4.28 (0.10)

Th	U
5.6 (0.08)	1.69 (0.06)

Table S8

Individual trace-element analyses by sample grain (ppm)

Sample	Analysis	Na	Ca	Ti	Rb	Sr	Y	Zr
D Cone	D Cone-CPX-1-CORE	2710.00	150500.00	3240.00	-0.02	51.20	6.26	9.86
	D cone-CPX-1-RIM	3210.00	158500.00	4380.00	0.86	60.30	9.49	21.25
	D Cone-CPX-2	2500.00	149400.00	3100.00	-0.02	40.10	5.68	7.99
	D Cone-CPX-3-CORE	3470.00	155800.00	4150.00	0.02	57.00	9.09	17.90
	D Cone-CPX-4-CORE	2609.00	152800.00	3298.00	-0.01	42.30	6.08	9.24
	D Cone-CPX-5	2688.00	153500.00	3630.00	0.02	42.70	6.39	10.14
D-4	D-4-CPX-1-CORE	2687.00	164200.00	6060.00	0.01	55.20	9.86	21.98
	D-4-CPX-2-CORE	2216.00	162000.00	5260.00	0.01	53.20	8.20	18.60
	D-4-CPX-3-CORE	2314.00	170000.00	6240.00	0.01	55.00	9.51	22.30
D-5	D-5-CPX-1-CORE	2980.00	147000.00	5640.00	0.09	25.60	34.10	81.30
	D-5-CPX-3	2400.00	106800.00	5180.00	0.80	18.45	19.80	75.00
	D-5-CPX-4	2903.00	153900.00	5010.00	0.18	24.50	37.90	98.00
H-17	H-17-CPX-1-CORE	3770.00	148100.00	4700.00	0.45	28.50	60.50	120.70
	H-17-CPX-2-CORE	3390.00	151300.00	3680.00	0.29	24.96	80.40	172.10
	H-17-CPX-3-CORE	3620.00	148800.00	3440.00	2.00	26.58	70.30	141.20
	H-17-CPX-4-CORE	3280.00	150100.00	2852.00	0.84	24.15	78.30	146.50
	H-17-CPX-5-CORE	4390.00	156800.00	2950.00	7.90	24.30	64.30	127.50
HA-12	HA-12-CPX-1-CORE	2940.00	139900.00	4750.00	-0.02	25.30	15.50	24.00
	HA-12-CPX-2-CORE	2790.00	153000.00	5590.00	0.01	25.10	15.07	21.90
	HA-12-CPX-3-CORE	2770.00	150800.00	4950.00	0.04	25.50	15.06	23.00
	HA-12-CPX-4-CORE	2810.00	152900.00	5620.00	-0.01	24.89	17.35	30.80
	HA-12-CPX-5-CORE	2263.00	131600.00	4310.00	0.01	21.08	13.29	20.80
	HA-12-CPX-6-CORE	2790.00	147000.00	4840.00	-0.03	22.40	14.02	21.90
HA-21	HA-21-CPX-2-CORE	3029.00	166600.00	7830.00	0.06	32.80	19.84	25.94
	HA-21-CPX-3-CORE	3020.00	143700.00	6500.00	0.03	30.20	28.20	53.00
HA-6	HA-6-CPX-1-CORE	3650.00	169700.00	4590.00	-0.01	46.60	11.56	23.04
	HA-6-CPX-3-CORE	3370.00	171500.00	4610.00	0.57	31.00	11.49	25.35
	HA-6-CPX-3-RIM	2790.00	136100.00	3280.00	-0.02	27.20	8.67	17.55
HC-10	HC-10-CPX-2-CORE	3170.00	154400.00	8730.00	-0.01	41.40	12.06	17.93
	HC-10-CPX-4	3000.00	155700.00	7540.00	0.02	35.40	12.00	23.93
	HC-10-CPX-5	3060.00	146900.00	7400.00	0.01	40.80	11.08	16.00
HC-12	HC-12-CPX-3	2820.00	147600.00	5170.00	0.51	34.30	13.32	33.40
HC-18 CG	HC-18 CG-CPX-1-CORE	2910.00	168500.00	6020.00	-0.01	30.90	15.01	23.40
HC-18 FG	HC-18 FG-CPX-2-CORE	2944.00	134600.00	6250.00	0.07	25.30	16.22	24.40
HC-21	HC-21-CPX-1	2960.00	137600.00	6000.00	-0.01	33.50	13.54	23.95
	HC-21-CPX-2-CORE	2930.00	141700.00	6220.00	0.04	33.11	15.04	24.43
	HC-21-CPX-3-CORE	2970.00	143800.00	6210.00	-0.01	35.20	13.59	24.82

	HC-21-CPX-4-CORE	2855.00	143700.00	6430.00	0.01	36.20	15.17	27.04
HC-25 D	HC-25 D-CPX-1-CORE	2739.00	153200.00	6210.00	0.02	57.20	10.85	22.95
	HC-25 D-CPX-2-CORE	2850.00	150700.00	4520.00	0.01	55.50	8.02	16.45
HC-25 L	HC-25 L-CPX-1-RIM	2857.00	149900.00	5610.00	0.01	57.90	10.13	23.80
	HC-25 L-OPX-5	3082.00	168800.00	6700.00	-0.04	63.00	11.79	25.43
	HC-25 L-CPX-1-CORE	2870.00	159600.00	5850.00	0.02	61.80	10.61	24.10
HC-26	HC-26-CPX-1	3600.00	151500.00	6910.00	0.02	35.13	40.10	55.70
	HC-26-CPX-2-CORE	3590.00	149300.00	6130.00	0.07	36.20	30.20	35.30
	HC-26-CPX-3-CORE	3770.00	149800.00	6060.00	0.00	36.00	54.10	100.80
	HC-26-CPX-4	3400.00	143600.00	6910.00	0.05	35.20	30.70	35.10
	HC-26-CPX-5	3740.00	149100.00	5900.00	0.50	39.95	42.70	113.00
	HC-26-CPX-6	3670.00	160600.00	5770.00	0.00	33.40	47.80	88.60
HC-28	HC-28-CPX-1-B	2745.00	169800.00	3140.00	0.03	26.86	8.49	10.87
HC-47	HC-47-CPX-1	3760.00	168300.00	3130.00	0.06	68.60	9.60	34.20
	HC-47-CPX-2	3520.00	163800.00	4140.00	0.06	79.90	9.45	31.60
HC-52	HC-52-CPX-1	3050.00	157500.00	4660.00	0.01	55.10	9.31	19.80
	HC-52-CPX-2-CORE	2194.00	161100.00	4920.00	-0.02	45.70	8.45	16.72
	HC-52-CPX-3-CORE	2162.00	164400.00	5010.00	0.01	46.80	8.73	17.83
	HC-52-CPX-3-RIM	2228.00	156100.00	4600.00	-0.03	44.70	8.16	15.99
HC-61	HC-61-CPX-2-CORE	4460.00	167300.00	2910.00	0.02	73.70	10.55	18.30
	HC-61-CPX-4	4190.00	165300.00	2840.00	0.02	66.50	10.23	20.20
HC-76	HC-76-CPX-2-CORE	3320.00	148900.00	6040.00	0.02	26.94	20.37	36.80
	HC-76-CPX-2-RIM	3220.00	150900.00	5390.00	-0.01	26.84	21.40	39.90
	HC-76-CPX-3	3410.00	147500.00	6200.00	-0.01	28.90	19.43	32.50
HC-77	HC-77-CPX-1	2495.00	141600.00	2930.00	0.02	30.25	6.51	8.49
	HC-77-CPX-2-A	2730.00	144000.00	4910.00	0.02	32.40	11.98	18.22
	HC-77-CPX-3	2876.00	150800.00	5740.00	0.01	32.90	13.20	21.90
HK-1	HK-1-CPX-1-CORE	2481.00	160600.00	5860.00	-0.01	61.70	9.18	24.50
	HK-1-CPX-2	2434.00	164600.00	6550.00	0.02	53.70	10.75	24.20
	HK-1-CPX-3-CORE	2360.00	160300.00	6900.00	-0.01	57.90	8.46	15.88
	HK-1-CPX-3-RIM	2332.00	162700.00	5980.00	0.03	57.50	8.03	17.38
	HK-1-CPX-4	2307.00	162000.00	6960.00	0.00	54.80	11.25	25.69
	HK-1-CPX-5-CORE	2133.00	158400.00	3920.00	0.01	45.40	6.42	11.70

Sample	Analysis	Nb	La	Ce	Pr	Nd	Sm	Eu
D Cone	D Cone-CPX-1-CORE	0.17	1.20	4.99	0.87	4.51	1.51	0.50
	D cone-CPX-1-RIM	0.35	1.63	6.75	1.19	6.80	2.23	0.75
	D Cone-CPX-2	0.13	0.95	3.82	0.68	3.84	1.24	0.46
	D Cone-CPX-3-CORE	0.23	1.58	6.30	1.13	6.38	2.15	0.68
	D Cone-CPX-4-CORE	0.12	0.96	3.88	0.69	3.94	1.27	0.45
	D Cone-CPX-5	0.13	0.92	3.92	0.74	3.97	1.42	0.51
D-4	D-4-CPX-1-CORE	0.09	1.28	5.60	1.10	6.59	2.29	0.83

	D-4-CPX-2-CORE	0.06	1.06	4.55	0.95	5.68	1.99	0.70
	D-4-CPX-3-CORE	0.08	1.13	5.29	1.07	6.30	2.12	0.75
D-5	D-5-CPX-1-CORE	0.09	4.28	19.65	3.76	20.93	7.05	1.86
	D-5-CPX-3	0.31	3.49	16.27	2.69	13.41	4.25	1.04
	D-5-CPX-4	0.07	4.38	20.97	4.04	23.32	8.06	1.99
H-17	H-17-CPX-1-CORE	0.71	7.02	31.90	6.21	35.50	12.69	3.18
	H-17-CPX-2-CORE	0.88	9.30	48.00	9.00	50.90	17.31	3.85
	H-17-CPX-3-CORE	0.81	8.83	41.50	7.98	43.10	14.42	3.57
	H-17-CPX-4-CORE	0.11	9.45	46.90	9.01	50.90	16.88	3.73
	H-17-CPX-5-CORE	0.79	8.00	36.40	7.01	39.30	13.43	3.16
HA-12	HA-12-CPX-1-CORE	0.12	1.72	6.95	1.26	7.24	2.82	1.00
	HA-12-CPX-2-CORE	0.15	1.03	4.91	1.00	6.22	2.56	0.89
	HA-12-CPX-3-CORE	0.10	1.20	5.24	1.11	6.56	2.53	0.91
	HA-12-CPX-4-CORE	0.14	1.36	6.55	1.29	7.98	2.92	1.07
	HA-12-CPX-5-CORE	0.09	1.13	4.64	1.03	5.87	2.23	0.75
	HA-12-CPX-6-CORE	0.07	1.11	5.38	1.02	6.32	2.47	0.91
HA-21	HA-21-CPX-2-CORE	0.22	2.50	6.29	1.32	8.20	3.35	1.17
	HA-21-CPX-3-CORE	0.38	4.11	17.98	3.31	18.88	6.19	1.89
HA-6	HA-6-CPX-1-CORE	0.14	1.28	4.80	0.83	4.69	1.59	0.66
	HA-6-CPX-3-CORE	0.18	0.92	3.29	0.61	3.49	1.30	0.50
	HA-6-CPX-3-RIM	0.10	0.86	2.62	0.46	2.69	0.99	0.39
HC-10	HC-10-CPX-2-CORE	0.09	0.89	3.86	0.83	5.15	2.13	0.84
	HC-10-CPX-4	0.08	1.03	5.15	1.05	6.09	2.32	0.81
	HC-10-CPX-5	0.09	0.62	3.11	0.70	4.68	2.00	0.76
HC-12	HC-12-CPX-3	0.45	1.33	5.74	1.11	6.64	2.47	0.89
HC-18 CG	HC-18 CG-CPX-1-CORE	0.08	1.27	5.39	1.11	6.74	2.69	0.96
HC-18 FG	HC-18 FG-CPX-2-CORE	0.45	1.88	5.46	1.22	7.30	2.60	0.93
HC-21	HC-21-CPX-1	0.08	1.20	5.95	1.18	7.12	2.71	0.88
	HC-21-CPX-2-CORE	0.12	1.22	5.77	1.18	7.15	2.78	0.95
	HC-21-CPX-3-CORE	0.06	1.21	6.02	1.15	7.11	2.79	0.97
	HC-21-CPX-4-CORE	0.09	1.40	6.39	1.32	7.88	2.76	1.07
HC-25 D	HC-25 D-CPX-1-CORE	0.13	1.23	5.41	1.11	6.44	2.36	0.84
	HC-25 D-CPX-2-CORE	0.08	1.01	4.52	0.87	5.26	1.86	0.62
HC-25 L	HC-25 L-CPX-1-RIM	0.13	1.24	5.54	1.06	6.46	2.25	0.82
	HC-25 L-CPX-5	0.11	1.35	6.01	1.25	7.33	2.74	0.94
	HC-25 L-CPX-1-CORE	0.17	1.33	5.80	1.11	6.75	2.35	0.84
HC-26	HC-26-CPX-1	0.15	4.73	21.55	3.96	22.90	8.41	2.26
	HC-26-CPX-2-CORE	0.16	3.05	13.78	2.66	15.99	5.71	1.89
	HC-26-CPX-3-CORE	0.16	7.81	37.20	7.34	40.00	12.96	3.20
	HC-26-CPX-4	0.13	2.98	14.53	2.75	16.11	5.87	1.78
	HC-26-CPX-5	0.42	8.05	32.64	5.71	29.00	9.13	2.64

	HC-26-CPX-6	0.06	5.44	26.16	5.00	28.80	9.88	2.64
HC-28	HC-28-CPX-1-B	0.11	0.74	3.51	0.44	2.23	0.78	0.32
HC-47	HC-47-CPX-1	0.28	1.74	5.74	0.92	4.69	1.45	0.51
	HC-47-CPX-2	0.33	1.90	6.57	1.01	4.96	1.47	0.52
HC-52	HC-52-CPX-1	0.22	1.57	6.23	1.13	6.15	2.00	0.71
	HC-52-CPX-2-CORE	0.08	0.91	4.05	0.82	5.02	1.84	0.66
	HC-52-CPX-3-CORE	0.06	0.83	3.92	0.86	4.89	1.79	0.67
	HC-52-CPX-3-RIM	0.09	0.84	3.98	0.80	5.10	1.82	0.61
HC-61	HC-61-CPX-2-CORE	0.18	1.89	5.89	0.96	5.27	1.63	0.59
	HC-61-CPX-4	0.15	1.57	5.12	0.82	4.01	1.57	0.54
HC-76	HC-76-CPX-2-CORE	0.05	1.60	8.10	1.60	9.45	3.72	1.16
	HC-76-CPX-2-RIM	0.04	1.70	7.92	1.61	9.97	3.90	1.30
	HC-76-CPX-3	0.10	1.72	7.84	1.50	9.12	3.50	1.23
HC-77	HC-77-CPX-1	0.09	0.74	3.07	0.56	3.13	1.22	0.43
	HC-77-CPX-2-A	0.07	1.02	5.01	0.99	5.85	2.28	0.76
	HC-77-CPX-3	0.09	1.25	5.49	1.13	6.61	2.60	0.89
HK-1	HK-1-CPX-1-CORE	0.18	1.34	5.95	1.15	6.64	2.12	0.78
	HK-1-CPX-2	0.08	1.22	5.58	1.14	6.89	2.52	0.85
	HK-1-CPX-3-CORE	0.09	0.82	3.87	0.80	5.11	1.97	0.76
	HK-1-CPX-3-RIM	0.12	0.88	3.99	0.82	5.08	1.82	0.70
	HK-1-CPX-4	0.09	1.29	5.95	1.23	7.22	2.57	0.88
	HK-1-CPX-5-CORE	0.05	0.78	3.44	0.72	4.11	1.49	0.52

Sample	Analysis	Gd	Er	Yb	Dy	Lu	Hf	Th
D Cone	D Cone-CPX-1-CORE	1.65	0.63	0.43	1.32	0.06	0.42	0.02
	D cone-CPX-1-RIM	2.36	0.93	0.68	2.05	0.10	0.82	0.03
	D Cone-CPX-2	1.36	0.53	0.39	1.30	0.06	0.37	0.01
	D Cone-CPX-3-CORE	2.19	0.90	0.65	2.08	0.08	0.69	0.03
	D Cone-CPX-4-CORE	1.47	0.62	0.41	1.40	0.06	0.40	0.01
	D Cone-CPX-5	1.66	0.70	0.48	1.38	0.06	0.47	0.01
D-4	D-4-CPX-1-CORE	2.51	0.99	0.75	2.25	0.10	1.03	0.01
	D-4-CPX-2-CORE	2.16	0.82	0.57	1.91	0.07	0.91	0.00
	D-4-CPX-3-CORE	2.48	0.96	0.66	2.14	0.09	1.11	0.01
D-5	D-5-CPX-1-CORE	7.99	3.39	2.30	7.42	0.30	2.70	0.11
	D-5-CPX-3	4.77	1.93	1.47	4.09	0.21	2.58	0.13
	D-5-CPX-4	8.83	3.89	2.69	8.15	0.37	3.68	0.09
H-17	H-17-CPX-1-CORE	14.24	5.87	4.36	13.24	0.59	4.57	0.33
	H-17-CPX-2-CORE	19.31	8.04	5.77	17.33	0.78	6.86	0.28
	H-17-CPX-3-CORE	16.32	6.67	4.81	15.30	0.64	5.26	0.55
	H-17-CPX-4-CORE	18.10	7.80	5.74	17.20	0.78	6.76	0.36
	H-17-CPX-5-CORE	14.40	6.44	4.41	13.78	0.63	5.82	2.78
HA-12	HA-12-CPX-1-CORE	3.09	1.71	1.16	3.31	0.16	0.78	0.10

	HA-12-CPX-2-CORE	3.19	1.50	1.09	3.15	0.14	0.97	0.02
	HA-12-CPX-3-CORE	3.22	1.48	1.12	3.15	0.15	0.98	0.03
	HA-12-CPX-4-CORE	3.62	1.65	1.18	3.72	0.16	1.14	0.03
	HA-12-CPX-5-CORE	2.89	1.23	0.95	2.75	0.14	0.85	0.06
	HA-12-CPX-6-CORE	3.11	1.45	1.08	3.16	0.16	0.85	0.05
HA-21	HA-21-CPX-2-CORE	4.27	1.93	1.30	4.27	0.18	1.17	0.06
	HA-21-CPX-3-CORE	6.76	2.77	2.03	6.10	0.26	1.60	0.06
HA-6	HA-6-CPX-1-CORE	2.31	1.06	0.79	2.42	0.10	0.93	0.02
	HA-6-CPX-3-CORE	2.03	1.13	0.79	2.43	0.10	1.08	0.02
	HA-6-CPX-3-RIM	1.36	0.88	0.58	1.78	0.08	0.78	0.01
HC-10	HC-10-CPX-2-CORE	2.76	1.15	0.84	2.66	0.11	0.81	0.03
	HC-10-CPX-4	2.97	1.18	0.91	2.68	0.10	0.91	0.03
	HC-10-CPX-5	2.66	1.09	0.79	2.51	0.09	0.93	0.01
HC-12	HC-12-CPX-3	2.95	1.34	0.96	2.86	0.13	1.52	0.06
HC-18 CG	HC-18 CG-CPX-1-CORE	3.33	1.57	1.10	3.32	0.15	0.91	0.01
HC-18 FG	HC-18 FG-CPX-2-CORE	3.31	1.65	1.25	3.30	0.17	0.92	0.05
HC-21	HC-21-CPX-1	3.19	1.38	1.01	2.96	0.13	1.08	0.01
	HC-21-CPX-2-CORE	3.40	1.54	1.13	3.28	0.15	1.13	0.01
	HC-21-CPX-3-CORE	3.22	1.52	1.07	3.01	0.14	1.09	0.02
	HC-21-CPX-4-CORE	3.55	1.55	1.11	3.35	0.16	1.12	0.01
HC-25 D	HC-25 D-CPX-1-CORE	2.76	1.12	0.77	2.49	0.11	1.15	0.01
	HC-25 D-CPX-2-CORE	1.97	0.81	0.53	1.92	0.08	0.69	0.00
HC-25 L	HC-25 L-CPX-1-RIM	2.51	0.99	0.72	2.22	0.09	1.19	0.01
	HC-25 L-CPX-5	3.07	1.16	0.83	2.74	0.10	1.25	0.01
	HC-25 L-CPX-1-CORE	2.60	1.02	0.72	2.23	0.11	1.11	0.02
HC-26	HC-26-CPX-1	9.20	4.10	2.97	8.78	0.40	1.65	0.11
	HC-26-CPX-2-CORE	6.63	3.08	2.31	6.47	0.31	1.37	0.08
	HC-26-CPX-3-CORE	13.47	5.69	4.00	12.71	0.50	2.82	0.06
	HC-26-CPX-4	6.91	3.26	2.30	6.40	0.33	1.29	0.09
	HC-26-CPX-5	10.17	4.44	3.25	9.41	0.46	4.02	0.20
	HC-26-CPX-6	11.15	4.68	3.51	10.48	0.47	2.38	0.08
HC-28	HC-28-CPX-1-B	1.30	0.85	0.58	1.72	0.07	0.37	0.01
HC-47	HC-47-CPX-1	1.85	0.98	0.62	2.05	0.09	1.15	0.03
	HC-47-CPX-2	1.73	0.91	0.56	2.02	0.07	0.97	0.02
HC-52	HC-52-CPX-1	2.13	0.93	0.67	2.07	0.08	0.78	0.02
	HC-52-CPX-2-CORE	2.07	0.85	0.66	1.94	0.09	0.84	0.01
	HC-52-CPX-3-CORE	2.01	0.89	0.63	1.95	0.09	0.84	0.01
	HC-52-CPX-3-RIM	2.04	0.80	0.57	1.84	0.07	0.80	0.01
HC-61	HC-61-CPX-2-CORE	2.04	0.90	0.74	2.15	0.09	0.51	0.03
	HC-61-CPX-4	2.00	1.07	0.60	2.26	0.09	0.57	0.03
HC-76	HC-76-CPX-2-CORE	4.36	2.01	1.38	4.23	0.23	1.27	0.02

	HC-76-CPX-2-RIM	4.73	2.00	1.52	4.58	0.21	1.53	0.07
	HC-76-CPX-3	4.21	1.96	1.50	4.13	0.19	1.13	0.03
HC-77	HC-77-CPX-1	1.54	0.62	0.55	1.42	0.07	0.32	0.01
	HC-77-CPX-2-A	2.52	1.20	0.87	2.42	0.12	0.63	0.01
	HC-77-CPX-3	3.03	1.36	1.09	2.93	0.15	0.93	0.01
HK-1	HK-1-CPX-1-CORE	2.45	0.90	0.66	2.24	0.08	1.05	0.02
	HK-1-CPX-2	2.75	0.99	0.74	2.39	0.09	1.17	0.01
	HK-1-CPX-3-CORE	2.38	0.91	0.58	2.08	0.08	0.88	0.01
	HK-1-CPX-3-RIM	2.04	0.78	0.55	1.89	0.08	0.91	0.02
	HK-1-CPX-4	3.16	1.09	0.79	2.76	0.10	1.27	0.01
	HK-1-CPX-5-CORE	1.67	0.67	0.48	1.45	0.07	0.55	0.00

Sample	Analysis	U
D Cone	D Cone-CPX-1-CORE	0.00
	D cone-CPX-1-RIM	0.02
	D Cone-CPX-2	0.00
	D Cone-CPX-3-CORE	0.01
	D Cone-CPX-4-CORE	0.01
	D Cone-CPX-5	0.01
D-4	D-4-CPX-1-CORE	0.00
	D-4-CPX-2-CORE	0.00
	D-4-CPX-3-CORE	0.00
D-5	D-5-CPX-1-CORE	0.03
	D-5-CPX-3	0.03
	D-5-CPX-4	0.04
H-17	H-17-CPX-1-CORE	0.11
	H-17-CPX-2-CORE	0.07
	H-17-CPX-3-CORE	0.16
	H-17-CPX-4-CORE	0.07
	H-17-CPX-5-CORE	1.04
HA-12	HA-12-CPX-1-CORE	0.03
	HA-12-CPX-2-CORE	0.01
	HA-12-CPX-3-CORE	0.02
	HA-12-CPX-4-CORE	0.01
	HA-12-CPX-5-CORE	0.02
	HA-12-CPX-6-CORE	0.01
HA-21	HA-21-CPX-2-CORE	0.02
	HA-21-CPX-3-CORE	0.02
HA-6	HA-6-CPX-1-CORE	0.01
	HA-6-CPX-3-CORE	0.01
	HA-6-CPX-3-RIM	0.01
HC-10	HC-10-CPX-2-CORE	0.01

	HC-10-CPX-4	0.01
	HC-10-CPX-5	0.00
HC-12	HC-12-CPX-3	0.02
HC-18 CG	HC-18 CG-CPX-1-CORE	0.01
HC-18 FG	HC-18 FG-CPX-2-CORE	0.02
HC-21	HC-21-CPX-1	0.01
	HC-21-CPX-2-CORE	0.00
	HC-21-CPX-3-CORE	0.00
	HC-21-CPX-4-CORE	0.00
HC-25 D	HC-25 D-CPX-1-CORE	0.00
	HC-25 D-CPX-2-CORE	0.00
HC-25 L	HC-25 L-CPX-1-RIM	0.01
	HC-25 L-CPX-5	0.01
	HC-25 L-CPX-1-CORE	0.01
HC-26	HC-26-CPX-1	0.03
	HC-26-CPX-2-CORE	0.03
	HC-26-CPX-3-CORE	0.02
	HC-26-CPX-4	0.03
	HC-26-CPX-5	0.05
	HC-26-CPX-6	0.03
HC-28	HC-28-CPX-1-B	0.01
HC-47	HC-47-CPX-1	0.01
	HC-47-CPX-2	0.00
HC-52	HC-52-CPX-1	0.00
	HC-52-CPX-2-CORE	0.00
	HC-52-CPX-3-CORE	0.00
	HC-52-CPX-3-RIM	0.00
HC-61	HC-61-CPX-2-CORE	0.00
	HC-61-CPX-4	0.01
HC-76	HC-76-CPX-2-CORE	0.01
	HC-76-CPX-2-RIM	0.02
	HC-76-CPX-3	0.00
HC-77	HC-77-CPX-1	0.00
	HC-77-CPX-2-A	0.00
	HC-77-CPX-3	0.00
HK-1	HK-1-CPX-1-CORE	0.01
	HK-1-CPX-2	0.00
	HK-1-CPX-3-CORE	0.00
	HK-1-CPX-3-RIM	0.01
	HK-1-CPX-4	0.01
	HK-1-CPX-5-CORE	0.00

Table S9

Individual trace-element analyses by sample grain (ppm)

Sample	Analysis	Na	Ca	Ti	Rb	Sr	Y	Zr	Nb
D-5	D-5-OPX-1-CORE	83.80	5420.00	2019.00	0.06	0.04	4.10	6.38	0.02
	D-5-OPX-1-RIM	78.20	5750.00	1942.00	0.00	0.03	4.41	5.61	0.00
	D-5-OPX-2-CORE	121.10	7900.00	2365.00	0.01	0.15	4.59	6.26	0.00
	D-5-OPX-2-RIM	169.00	10200.00	2062.00	0.01	0.57	4.95	7.66	0.00
	D-5-OPX-3	71.20	5420.00	1794.00	0.03	0.04	3.88	4.56	0.00
	D-5-OPX-4	118.90	7380.00	2820.00	0.02	0.29	4.85	8.94	0.19
	D-5-OPX-5	186.10	9250.00	2676.00	0.07	0.35	5.46	9.51	0.02
	D-5-OPX-6	164.70	8370.00	2517.00	0.00	0.12	4.85	7.07	0.01
	D-5-OPX-2	429.00	10400.00	3300.00	3.60	1.96	5.45	11.30	0.18
HA-12	HA-12-OPX-1-CORE	90.10	6830.00	2280.00	-0.01	0.14	1.68	1.55	0.00
	HA-12-OPX-2-CORE	97.10	7600.00	2187.00	0.01	0.07	2.45	2.52	0.01
	HA-12-OPX-2-RIM	66.80	6190.00	1885.00	0.02	0.05	2.17	2.11	0.00
	HA-12-OPX-3	169.90	10050.00	2623.00	0.00	0.49	2.21	2.65	0.01
	HA-12-OPX-4-CORE	134.00	7930.00	2531.00	-0.04	0.24	1.99	2.75	0.02
	HA-12-OPX-5-CORE	178.30	11780.00	2643.00	0.01	0.63	2.48	3.04	0.00
	HA-12-OPX-6	168.70	10290.00	2623.00	-0.01	0.45	2.38	2.46	0.01
HA-21	HA-21-OPX-1	200.80	10180.00	2950.00	-0.01	0.51	2.67	2.29	0.02
	HA-21-OPX-2-CORE	275.00	10400.00	2750.00	0.00	1.21	3.01	2.68	0.04
	HA-21-OPX-3	223.30	12040.00	3280.00	0.01	0.72	2.90	2.95	0.03
	HA-21-OPX-4-CORE	197.40	10990.00	3450.00	0.01	0.55	3.06	2.81	0.05
	HA-21-OPX-4-RIM	188.00	10860.00	3040.00	0.01	0.51	2.77	2.63	0.05
	HA-21-OPX-5	190.00	11040.00	2760.00	-0.01	1.05	4.66	5.52	0.06
HC-12	HC-12-OPX-1-CORE	109.40	8500.00	3118.00	0.03	0.21	2.04	2.26	0.01
	HC-12-OPX-1-RIM	178.50	11800.00	3270.00	1.10	1.60	2.33	3.05	0.02
	HC-12-OPX-2-CORE	175.60	11840.00	3650.00	-0.01	0.67	2.62	3.59	0.03
H-17	H-17-OPX-1-CORE	496.00	11870.00	2611.00	0.14	1.54	12.66	11.31	0.07
	H-17-OPX-2-CORE	400.00	16100.00	2750.00	0.03	1.47	13.79	25.70	0.43

Sample	Analysis	La	Ce	Pr	Nd	Sm	Eu	Gd	Er
D-5	D-5-OPX-1-CORE	0.01	0.05	0.01	0.12	0.09	0.03	0.26	0.49
	D-5-OPX-1-RIM	0.01	0.06	0.01	0.12	0.08	0.03	0.20	0.51
	D-5-OPX-2-CORE	0.03	0.19	0.03	0.28	0.14	0.05	0.30	0.57
	D-5-OPX-2-RIM	0.11	0.61	0.10	0.63	0.23	0.09	0.47	0.65
	D-5-OPX-3	0.02	0.07	0.02	0.13	0.12	0.03	0.20	0.48
	D-5-OPX-4	0.06	0.32	0.06	0.34	0.21	0.06	0.38	0.56

	D-5-OPX-5	0.11	0.50	0.09	0.58	0.27	0.08	0.45	0.65
	D-5-OPX-6	0.03	0.19	0.03	0.27	0.18	0.05	0.39	0.63
	D-5-OPX-2	0.23	0.79	0.14	0.86	0.34	0.10	0.60	0.64
HA-12	HA-12-OPX-1-CORE	0.01	0.04	0.01	0.06	0.03	0.03	0.13	0.21
	HA-12-OPX-2-CORE	0.00	0.03	0.00	0.07	0.05	0.03	0.16	0.30
	HA-12-OPX-2-RIM	0.00	0.02	0.00	0.05	0.02	0.03	0.10	0.26
	HA-12-OPX-3	0.03	0.13	0.03	0.17	0.09	0.04	0.21	0.27
	HA-12-OPX-4-CORE	0.02	0.07	0.01	0.12	0.08	0.02	0.15	0.27
	HA-12-OPX-5-CORE	0.07	0.25	0.04	0.30	0.15	0.05	0.22	0.26
	HA-12-OPX-6	0.03	0.12	0.03	0.15	0.13	0.05	0.23	0.30
HA-21	HA-21-OPX-1	0.03	0.14	0.03	0.16	0.12	0.05	0.21	0.30
	HA-21-OPX-2-CORE	0.13	0.29	0.07	0.34	0.13	0.05	0.26	0.37
	HA-21-OPX-3	0.05	0.23	0.04	0.25	0.17	0.05	0.30	0.35
	HA-21-OPX-4-CORE	0.04	0.20	0.04	0.23	0.10	0.04	0.23	0.37
	HA-21-OPX-4-RIM	0.05	0.18	0.04	0.24	0.11	0.04	0.23	0.28
	HA-21-OPX-5	0.25	0.52	0.11	0.58	0.27	0.08	0.45	0.51
HC-12	HC-12-OPX-1-CORE	0.01	0.04	0.01	0.08	0.07	0.03	0.14	0.31
	HC-12-OPX-1-RIM	0.03	0.13	0.03	0.23	0.09	0.04	0.22	0.30
	HC-12-OPX-2-CORE	0.02	0.12	0.02	0.18	0.14	0.05	0.25	0.31
H-17	H-17-OPX-1-CORE	0.63	3.04	0.55	2.82	0.93	0.26	1.38	1.40
	H-17-OPX-2-CORE	0.68	3.52	0.61	3.50	1.22	0.33	1.64	1.50

Sample	Analysis	Yb	Dy	Lu	Hf	Th	U
D-5	D-5-OPX-1-CORE	0.69	0.53	0.12	0.24	0.01	0.00
	D-5-OPX-1-RIM	0.69	0.49	0.13	0.20	0.01	0.00
	D-5-OPX-2-CORE	0.72	0.60	0.13	0.27	0.01	0.00
	D-5-OPX-2-RIM	0.73	0.80	0.13	0.32	0.03	0.00
	D-5-OPX-3	0.63	0.53	0.12	0.18	0.02	0.00
	D-5-OPX-4	0.66	0.60	0.12	0.29	0.00	0.01
	D-5-OPX-5	0.77	0.76	0.13	0.33	0.03	0.01
	D-5-OPX-6	0.71	0.67	0.13	0.27	0.00	0.00
	D-5-OPX-2	0.67	0.84	0.11	0.40	0.05	0.01
HA-12	HA-12-OPX-1-CORE	0.34	0.23	0.05	0.07	0.00	0.00
	HA-12-OPX-2-CORE	0.39	0.34	0.07	0.11	0.00	0.00
	HA-12-OPX-2-RIM	0.32	0.30	0.06	0.09	0.00	0.00
	HA-12-OPX-3	0.33	0.29	0.06	0.10	0.01	0.00
	HA-12-OPX-4-CORE	0.31	0.26	0.06	0.13	0.00	0.00
	HA-12-OPX-5-CORE	0.37	0.38	0.05	0.12	0.01	0.00
	HA-12-OPX-6	0.37	0.38	0.06	0.09	0.01	0.00
HA-21	HA-21-OPX-1	0.30	0.37	0.07	0.12	0.01	0.01
	HA-21-OPX-2-CORE	0.35	0.43	0.06	0.12	0.02	0.00
	HA-21-OPX-3	0.40	0.45	0.07	0.13	0.02	0.01

	HA-21-OPX-4-CORE	0.41	0.41	0.07	0.12	0.03	0.00
	HA-21-OPX-4-RIM	0.37	0.38	0.06	0.11	0.02	0.01
	HA-21-OPX-5	0.58	0.65	0.10	0.17	0.01	0.00
HC-12	HC-12-OPX-1-CORE	0.34	0.29	0.06	0.11	0.00	0.00
	HC-12-OPX-1-RIM	0.32	0.37	0.05	0.18	0.00	0.00
	HC-12-OPX-2-CORE	0.40	0.39	0.07	0.22	0.00	0.00
H-17	H-17-OPX-1-CORE	1.60	1.98	0.27	0.30	0.13	0.05
	H-17-OPX-2-CORE	1.64	2.30	0.27	0.78	0.26	0.05

Table S11
$\delta^{18}O$ duplicate measurements

	Clinopyroxene		Olivine		Plagioclase
Sample	$\delta^{18}O$-1	$\delta^{18}O$-2	$\delta^{18}O$-1	$\delta^{18}O$-2	$\delta^{18}O$-1
D Cone	4.53	4.54	4.76	4.69	−
D-4	3.90	4.25	4.17	4.38	−
D-5	4.03	4.16	−	−	−
HA-21	4.16	4.15	4.09	4.02	5.10
HA-6	−	−	4.75	−	−
HC-10	3.49	3.44	3.34	3.36	4.40
HC-12	4.00	4.03	3.98	4.02	−
HC-18 CG	−	−	−	−	5.10
HC-21	4.24	4.48	4.20	4.16	−
HC-25 D	4.97	−	4.77	4.32	−
HC-26	−	−	4.72	−	−
HC-28	−	−	4.74	−	−
HC-47	−	−	4.72	−	−
HC-61	−	−	4.66	−	−
HK-1	4.29	4.29	4.28	4.30	−